Faculty of Physics and Astronomy
University of Heidelberg

Diploma thesis
in Physics

submitted by
Jonas Fölling
born in Oldenburg (Oldb)
2005

Bose-Einstein Josephson Tunnelling and Generation of Arbitrary Optical Potentials

This diploma thesis has been carried out by Jonas Fölling at the
Kirchhoff-Institut für Physik
under the supervision of
Prof. Dr. M. K. Oberthaler

Bose-Einstein Josephson Tunneln und Erzeugung von Beliebigen Optischen Potenzialen

Diese Arbeit beschreibt die erste experimentelle Realisierung eines Josephsonkontaktes für Bose-Einstein Kondensate (BEC). Dieser wird durch ein optisches Doppelmuldenpotenzial erzeugt, in das ein BEC aus ^{87}Rb-Atomen hineingeladen wird. Die Wellenfunktionen der Kondensatteile in der linken bzw. der rechten Potenzialmulde überlappen in der zentralen Tunnelbarriere des Potenzials, was eine schwache Kopplung beider Wellenfunktionen bewirkt. In Übereinstimmung mit theoretischen Vorhersagen lassen sich zwei dynamische Regimes dieses Systems nachweisen: Ein anfänglicher kleiner Populationsunterschied von Atomen in den Mulden führt zu Oszillationen des relativen Populationsunterschiedes, wobei die Atome durch die zentrale Barriere tunneln, sowie des Phasenunterschieds zwischen linkem und rechtem Kondensat. Überschreitet der anfängliche Populationsunterschied einen bestimmten kritischen Wert, so wird diese Tunnelbewegung unterbunden und die Populationsinvarianz bleibt erhalten, während der Phasenunterschied linear ansteigt. Dieser Effekt ist bedingt durch die Wechselwirkung zwischen den Atomen und wird 'macroscopic quantum self-trapping' genannt.
Des Weiteren beschreibt diese Arbeit eine Erweiterung des experimentellen Aufbaus, die das Erzeugen beliebiger optischer Potenziale für die Atome ermöglicht. Diese Potenziale können entweder als Atomfalle benutzt werden, oder zum Aufprägen beliebiger Phasenmuster auf ein BEC. Die Tests von Prototypen und detaillierte Vorlagen für den Aufbau werden vorgestellt. Besonderes Augenmerk gilt dabei dem speziellen Objektiv, das für diese Apparatur benötigt wird.

Bose-Einstein Josephson Tunnelling and Generation of Arbitrary Optical Potentials

This thesis describes the first experimental realisation of a Josephson junction for Bose-Einstein condensates (BEC), implemented by a ^{87}Rb-BEC in an optical double well potential. The wave functions of the condensate parts in the left and right well, respectively, are overlapping in the central barrier of the potential, resulting in a weak link between both parts. Two dynamical regimes are demonstrated in agreement with theoretical predictions: An initial small imbalance of the atomic population in the wells leads to oscillations of the relative population, with atoms tunnelling through the central barrier, as well as to oscillations of the phase difference between both parts. Exceeding a critical value, the initial population imbalance remains locked and the phase difference increases linearly. This effect originates in the atomic interaction and is called 'macroscopic quantum self-trapping'.
Furthermore this thesis describes an extension to the experimental setup which allows for the creation of arbitrary optical potentials for atoms. These potentials can be used either as atom traps or for imprinting arbitrary phase patterns onto a BEC. Tests of prototypes and detailed blueprints for the construction of this apparatus are presented. Special focus is put on the customised objective needed for this device.

Contents

1 Introduction **1**

2 Theory of the Superconducting Josephson Junction **5**
2.1 The DC Josephson Effect 5
2.2 The AC Josephson Effect 7
2.3 The Resistively and Capacitively Shunted Josephson Junction Model . . 7

3 Theory of the Bose-Einstein Josephson Junction **11**
3.1 The Bose-Einstein Condensate 11
3.1.1 Condensation of Bosonic Atoms 11
3.1.2 Description of BEC Dynamics: The Gross-Pitaevskii Equation . . 13
3.2 Two Mode Model of the Bose-Einstein Josephson Junction 13
3.2.1 Josephson Oscillation Regime 17
3.2.2 Self-Trapping Regime 19
3.2.3 π-Phase Modes 20
3.3 Numerical Simulations of the Bose-Einstein Josephson Dynamics 20

4 Experimental Setup **21**
4.1 Gathering and Condensing ^{87}Rb Atoms 21
4.1.1 Collecting Atoms in the MOT 21
4.1.2 Evaporative Cooling in the Magnetic Trap 23
4.1.3 Optical Potentials and Traps 25
4.2 Creating a Double Well Potential 27
4.2.1 Experimental Method 27
4.2.2 Analysis and Improvement of Stability 29
4.3 Imaging System 35
4.3.1 Imaging Setup 35
4.3.2 Diffraction Effects 37
4.3.3 Estimation of the Optical Resolution 42

5 Experimental Results **49**
5.1 Considerations on Trap Parameters 49
5.2 Initiating the Tunnelling Dynamics 49
5.2.1 Phase Induced Josephson Oscillations 49
5.2.2 Population-Imbalance Induced Josephson Oscillations 52
5.3 Measuring the Population Imbalance $z(t)$ 53
5.4 Measuring the Phase Difference $\phi(t)$ 55

5.5 Calibrating the Trap Parameters 55
5.6 Results of the Josephson Tunnelling Measurements 56

6 A New Objective: Towards High-Resolution Phase Imprinting and Imaging 59
6.1 The Need for an Extension of the Setup 59
6.2 Creating Arbitrary Optical Potentials 59
6.2.1 Holographic Imaging Technique 59
6.2.2 Time Averaged Optical Potentials 60
6.3 Experimental Setup of the Phase Imprinting Device 61
6.3.1 An Overview 61
6.3.2 The Beam Steering Device and Projection Optics 62
6.3.3 Detailed Objective Mounting 64
6.3.4 Working Principle of Acousto Optic Devices 64
6.4 Feasibility Study 66
6.4.1 Estimating the Spot Size 66
6.4.2 Test Setup For a Moving Light Sheet 68
6.4.3 Creating Simple Patterns 70
6.4.4 Important Aspects of Acousto Optic Devices 71
6.5 High-Resolution Imaging 72
6.6 The Objective 73

7 Conclusion and Outlook 81

Bibliography I

Chapter 1

Introduction

Quantum mechanics is, aside from the theory of relativity, probably the most intriguing fundamental field of physics not only to physicists but also to the interested public. Concepts such as quantised energy or the wave character of massive particles and the resulting effects like matter wave interference or, most prominently, the tunnelling through a classically forbidden region are raising curiosity since they seem to contradict our experience in the familiar macroscopic environment.
The experimental realisation of Bose-Einstein condensates in 1995 [1, 2, 3], gave us a new tool to study this fascinating field with an unprecedented clarity. This novel state of matter, first predicted by Albert Einstein in 1925 [4] based on quantum statistical considerations by Satyendra Nath Bose [5] from the year 1924, enables us to virtually look at quantum mechanical dynamics with a simple microscope.
A Bose-Einstein condensate is a dilute gas of weakly interacting bosonic atoms (up to 10^6) which are all in the ground state of their confining potential. They form a coherent macroscopic quantum mechanical matter wave whose extent can be larger than $100\,\mu$m. It can thus be directly observed by standard imaging techniques.
During the last ten years, Bose-Einstein condensates have therefore been extensively used as tools to study quantum mechanical effects known from different fields of physics: A classic was the observation of interference of two Bose-Einstein condensates at MIT in 1997 [6]. Due to the atomic interaction, Bose-Einstein condensates represent nonlinear matter waves, opening the way to perform experiments in analogy to nonlinear optics such as the creation of bright [7, 8, 9] and dark [10] solitons. Furthermore the observation of vortices [11] demonstrates the linkage to the field of condensed matter physics. Especially in the borderland to solid state physics many interesting experiments were performed using Bose-Einstein condensates in optical lattice potentials in analogy to the electrons in periodic potentials. Effects known from this field were 'simulated' while also fascinating new phenomena, connected to the interaction between the atoms could be studied. Performing these experiments the quantum mechanical system can be visually observed which is not possible in solid matter. Among the mentioned effects were Bloch-oscillations [12], Bragg-scattering [13, 14] and Landau-Zener tunnelling [15] for Bose-Einstein condensates. Probably the most impressive of these experiments connected to solid state physics was the observation of the quantum phase transition from the superfluid to the Mott insulator phase of atoms in a periodic lattice potential [16].

The Bose-Einstein Josephson Junction

A further fundamental effect in solid states physics is the Josephson tunnelling phenomenon encountered in Josephson junctions. These devices are composed of two superconductors which are separated by a thin tunnelling barrier. The macroscopic wave functions in each superconductor, composed of the Cooper paired electrons, are therefore overlapping, creating a weak link between them. The resulting dynamics of the current of tunnelling Cooper pairs and of the phases of the quantum mechanical wave functions have been predicted by Brian D. Josephson in 1962 [17]. He has been awarded the Nobel Prize for physics for this scientific merit in 1973. The first experimental evidence of the predicted phenomena has already been obtained in 1963 [18]. Today, Josephson junctions can be found in numerous applications for example in superconducting quantum interference devices (SQUIDs) [19], which are devices for measuring ultra small variations in magnetic fields with a resolution of up to 10^{-14} T.
The physical model describing the superconducting Josephson junction can also be applied to other systems of weakly linked macroscopic wave functions, including neutral superfluids [20] and Bose-Einstein condensates. The latter system, called 'Bose-Einstein Josephson junction' consists of two Bose-Einstein condensates in a double well potential which are coupled by a spatial overlap of the two wave functions in the central tunnelling barrier of the double well. Following the tradition of utilising Bose-Einstein condensates in order to mimic effects known from solid states physics, a manifold of theoretical works describe the expected dynamics of such a system, e.g. [21, 22, 23, 24, 25, 26, 27].
It has been predicted that due to the atomic interactions new dynamical regimes appear, unknown to superconducting Josephson junctions. The most striking of them is called 'macroscopic quantum self-trapping', leading to an inhibition of tunnelling.
The experimental implementation of a single Bose-Einstein Josephson junction, however, took about ten years since the first realisation of a Bose-Einstein condensate. Earlier implementations of double well potentials using magnetic traps [28], optical potentials created by two focussed, red detuned laser beams [29] or atom chips [30] were not appropriate for Josephson tunnelling dynamics on an observable timescale on the order of some tens of milliseconds [29] so far. The difficulty lies in the adequate tradeoff between atom number and barrier height and width. Generally spoken, thin tunnelling barriers of a size of just a few microns and small condensates of only ≈ 1000 atoms in total are necessary, which requires a setup being able to reliably produce condensates of that size. Furthermore a very good imaging system is needed in order to be still able to optically resolve the shape of the atomic cloud in the tiny double well potential.
Up to now only the analogue of a one-dimensional array of Josephson junctions, formed by a periodic optical lattice, has been experimentally implemented successfully [31]. In this case, however, the lattice spacing was only $\approx 400\,\mathrm{nm}$, therefore the dynamics of a single junction could not be resolved. The observation was restricted to the centre of mass movement of the Bose-Einstein condensate. Shortly before the beginning of my final year project in July 2004, my work group observed the above mentioned effect of macroscopic quantum self-trapping in a Josephson junction array [32] with a similar experimental setup. However, the single lattice sites could also not be resolved.
Finally the first realisation of a single Bose-Einstein Josephson junction has been achieved by our group in October 2004. The resolution of our imaging system is good enough to resolve the atomic cloud in its confinement, enabling us to look at the ongoing tun-

nelling dynamics in situ. Even the phase difference between the two condensates, which plays a crucial role in the Josephson tunnelling effect, could be measured by interference experiments.
Therefore, making use of the unmatched accessibility of a macroscopic quantum system composed of Bose-Einstein condensates, we can observe the Josephson tunnelling effect in an unprecedented clarity, while also being able to study the novel phenomenon of macroscopic quantum self-trapping arising from the atomic interaction.
This experiment will be presented in the first part of the thesis at hand.

A New Objective: Towards the Creation of Arbitrary Optical Potentials

Inspired by the Bose-Einstein Josephson junction experiments, where the phase difference between the wave functions is of great importance, it has been decided to extend the existing experimental setup with a phase manipulation tool.
The phase of the quantum mechanical wave function of a Bose-Einstein condensate can be locally altered using the phase imprinting technique [33]. This method is based on optical dipole potentials which, when turned on for a short time, produce a corresponding phase pattern on the condensate. Phase imprinting has for example been applied in order to create dark solitons in a Bose-Einstein condensate [10], which are characterised by a sudden step of up to π in the phase of the wave function.
Such an optical potential can be created by a focussed, off-resonant laser beam which is quickly scanned over the condensate, creating a time averaged light pattern of arbitrary shape whose spatial resolution is only limited by the size of the focus spot. The shape of these optical potentials is therefore extremely flexible, allowing for the creation of complex phase patterns. Applications are the creation of phase induced Josephson oscillations in order to complement the Bose-Einstein Josephson tunnelling experiments (see section 5.2.1) or the investigation of single and multiple ring dark solitons which require circular phase imprinting patterns [34].
The possibility of creating arbitrary optical potentials is not only interesting for phase imprinting which merely requires a short burst of light but also for fabricating complex static or time varying trapping potentials. This opens the way to the creation of dark soliton fans [35, 36], which requires a thin, quickly removable barrier in a harmonic confinement [37] or the implementation of a Fabry-Perot interferometer for Bose-Einstein condensates [38]. This interferometer consists of a condensate in a narrow waveguide potential with two thin tunnelling barriers, which can be easily implemented with such a system.
One of the strengths of our experimental setup is the reliable production of Bose-Einstein condensates with few atoms combined with an excellent imaging system. Therefore our apparatus is predestined to study effects requiring small Bose-Einstein condensates in tiny structures which we can still observe. Hence, a necessity of the new phase imprinting system is that the spot size of the focussed laser beam is as small as possible. This requires a well corrected high numerical aperture objective that is customised for our setup. If not used for phase imprinting or the creation of complex trapping potentials, this new objective can also be utilised as an additional imaging objective, enabling us to image the Bose-Einstein condensate from two different directions. The objective therefore represents the heart of this extension.
The development of the device for the creation of arbitrary optical potentials, often sim-

ply referred to as 'phase imprinting setup' was the second project of the thesis at hand. This versatile tool has been planned in detail and prototypes have been tested. Furthermore the special objective has been designed in cooperation with *Carl Zeiss Laser Systems* in Oberkochen, opening the way towards high resolution phase imprinting and imaging.

Contents of this Thesis

Apart from this introduction and the conclusion, the thesis contains two parts. The major part, containing chapters 2 to 5, describes the work which was done during the first six and a half months of this final year project, namely the experimental realisation of the Bose-Einstein Josephson junction, including some further improvements of the experimental setup. The second part, chapter 6, deals with the design and prototype testing of the new phase imprinting and imaging setup which has been done in the remaining time before this thesis was put down in writing.
In the first part, chapter 2 summarises the most important aspects of the 'original' Josephson junction in superconductors. After shortly illuminating the theory of Bose-Einstein condensation, chapter 3 then deals with the theoretical description of the Bose-Einstein Josephson junction, using a two mode model in close analogy to the description of the Josephson junction in superconductors in the previous chapter. Here, the differences in behaviour due to the atom-atom interaction for the Bose-Einstein system are especially pointed out. Following these theoretical considerations, the actual experimental setup is explained in chapter 4. Special focus is here put on the analysis of the stability of the so called 'crossed dipole trap' and on an improved setup for the one-dimensional lattice potential which has been implemented after having concluded the measurements on the Josephson tunnelling dynamics. The largest section of this chapter, however, deals with a thorough description of our imaging system. Chapter 5 presents the results of the measurements on the Bose-Einstein Josephson junction.
The second part, chapter 6, is to be understood as a combination of feasibility study and construction manual for the new setup. It includes the results of prototype testing and the description of the beam steering technique as well as engineering drawings for the actual setup and especially detailed drawings for the objective.
Chapter 7 concludes this thesis and shows up some prospects of the large variety of experiments which are waiting for this experimental setup and the team of physicists operating it.

Chapter 2

Theory of the Superconducting Josephson Junction

The fundamentals of the Josephson effect become manifest in two basic phenomena, the 'DC Josephson effect' and the 'AC Josephson effect'. Both effects are presented in this chapter, using a simplified model developed by Feynman [39] which nevertheless unveils the underlying physics and which can be found in numerous superconductor textbooks such as [19, 40, 41].

2.1 The DC Josephson Effect

The Josephson effect occurs in two superconductors S_L and S_R separated by a thin non-superconducting tunnelling barrier, as depicted in figure 2.1. The barrier between

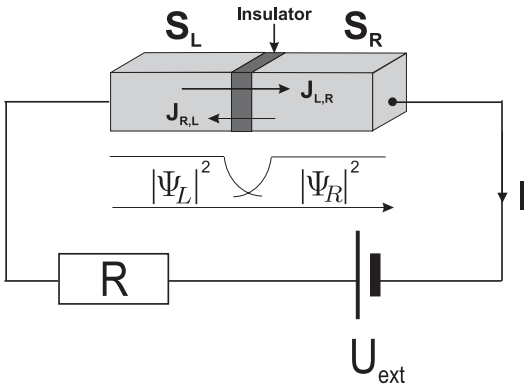

Figure 2.1: A Josephson junction. S_L and S_R represent the left and right superconductor which are separated by an insulating barrier. Depicted below are the density distributions $|\Psi_L|^2$ and $|\Psi_R|^2$ of the macroscopic quantum wave functions Ψ_L and Ψ_R formed by the Cooper pairs of the left and the right superconductor, respectively. The electric circuit is closed by a non-superconducting wire with resistance R and an external current source replacing the tunnelling Cooper paired electrons. I represents the current and $J_{L,R}$ ($J_{R,L}$) the current density in the Josephson junction going from S_L to S_R (S_R to S_L).

the two superconductors S_L and S_R is thin enough (typically 10 to 20 Å[41]) such that the macroscopic wave functions Ψ_L and Ψ_R describing the electron Cooper pairs of the left and right superconductor, respectively, are overlapping in the central region. This

case of two coupled quantum mechanical wave functions is called a 'weak link'. The Schrödinger equation for this coupled system is:

$$\begin{aligned} i\hbar\frac{\partial}{\partial t}\Psi_L &= E_L\Psi_L + K\Psi_R \\ i\hbar\frac{\partial}{\partial t}\Psi_R &= E_R\Psi_R + K\Psi_L \end{aligned} \tag{2.1}$$

Here, E_L and E_R denote the energy of the left and the right state, respectively. K is a constant coupling term which represents the overlap of the two wave functions. We will use the following ansatz for the wave functions:

$$\begin{aligned} \Psi_L &= \sqrt{\rho_L}e^{i\phi_L} \\ \Psi_R &= \sqrt{\rho_R}e^{i\phi_R} \end{aligned} \tag{2.2}$$

ρ_L and ρ_R are the densities of the Cooper pairs in the left and the right superconductor. ϕ_L and ϕ_R denote the phases of the two wave functions. Inserting (2.2) into (2.1) yields

$$\begin{aligned} i\hbar\left(\frac{1}{2\sqrt{\rho_L}}\dot{\rho}_L e^{i\phi_L} + i\sqrt{\rho_L}\dot{\phi}_L e^{i\phi_L}\right) &= E_L\sqrt{\rho_L}e^{i\phi_L} + K\sqrt{\rho_R}e^{i\phi_R}, \\ i\hbar\left(\frac{1}{2\sqrt{\rho_R}}\dot{\rho}_R e^{i\phi_R} + i\sqrt{\rho_R}\dot{\phi}_R e^{i\phi_R}\right) &= E_R\sqrt{\rho_R}e^{i\phi_R} + K\sqrt{\rho_L}e^{i\phi_L}. \end{aligned} \tag{2.3}$$

Multiplying the first of equations (2.3) with $\sqrt{\rho_L}e^{-i\phi_L}$ and the second one with $\sqrt{\rho_R}e^{-i\phi_R}$ and separating real and imaginary part, we get

$$\begin{aligned} \frac{1}{2}\hbar\dot{\rho}_L &= K\sqrt{\rho_L\rho_R}\sin(\phi), \qquad -\hbar\rho_L\dot{\phi}_L = E_L\rho_L + K\sqrt{\rho_L\rho_R}\cos(\phi), \\ \frac{1}{2}\hbar\dot{\rho}_R &= K\sqrt{\rho_R\rho_L}\sin(\phi), \qquad -\hbar\rho_R\dot{\phi}_R = E_R\rho_R + K\sqrt{\rho_R\rho_L}\cos(\phi), \end{aligned} \tag{2.4}$$

where we have introduced the relative phase between the two condensates: $\phi := \phi_R - \phi_L$ We will now assume two equal superconductors, i.e. $\rho_L = \rho_R =: \rho = const.$ From the left hand side equations in (2.4) we get an expression for the time dependence of the Cooper pair density:

$$\dot{\rho}_L = -\dot{\rho}_R = \frac{2K\rho}{\hbar}\sin(\phi) \tag{2.5}$$

Note, that although the Cooper pair density is assumed to be constant and equal in both superconductors its time derivative is not! This is no contradiction if large superconductors are assumed or if the particles moving from the left superconductor to the right

or vice versa are being replaced by an external current source, as depicted in figure 2.1. From the right hand side equations in (2.4) we get an expression for the time dependance of the relative phase:

$$\dot{\phi} = \frac{1}{\hbar}(E_R - E_L) \tag{2.6}$$

We will assume $E_R = E_L$ for a while, which means in our model that the current source replacing the electrons in the Josephson junction does not apply any voltage to it.
Considering the results derived so far, equation (2.5) reveals that we obtain a current of Cooper pairs tunnelling through the insulating barrier even if no voltage across the Josephson junction is applied, i.e. for $\phi = const$ and different than 0 or multiples of π. The tunnelling current is driven only by a phase difference between the quantum mechanical wave functions of left and right superconductor. If we consider that each Cooper pair has the charge of $2e$, the current density resulting from these tunnelling Cooper pairs can be expressed as:

$$J = J_0 \sin(\phi) \tag{2.7}$$

Here, $J_0 = \frac{4eK\rho}{\hbar}$ represents the maximum possible tunnelling current density of Cooper pairs. This effect is known as the 'DC Josephson effect'.

2.2 The AC Josephson Effect

We will now consider the case of an energy difference between left and right side, i.e. $E_R \neq E_L$. This corresponds to a constant voltage $U = \frac{E_R - E_L}{2e}$ applied to the Josephson junction. Equation (2.6) shows that the relative phase ϕ now increases linearly over time, resulting in an oscillating Cooper pair tunnelling current density $J(t)$ as can be seen from (2.7). This effect is called the 'AC Josephson effect'.

2.3 The Resistively and Capacitively Shunted Josephson Junction Model

The description of the DC- and the AC-Josephson effect only considered the current of Cooper pairs in the superconductor which are tunnelling through the insulating barrier. In a more realistic model of a Josephson junction the 'normal' single electron current has to be considered as well. This is taken into account in the resistively and capacitively shunted Josephson junction (RCSJ) model developed by Stewart [42] and McCumber [43] in 1968. Figure 2.2 depicts a model circuit for this case. For electrons which are not Cooper paired the barrier between the two superconductors is approximated as a resistor with constant resistivity R and the capacitance of the junction is assumed to be C. Therefore the 'ideal' Josephson junction is shunted with a resistor and a capacitance. The total current I flowing through the shunted junction is composed of the Cooper

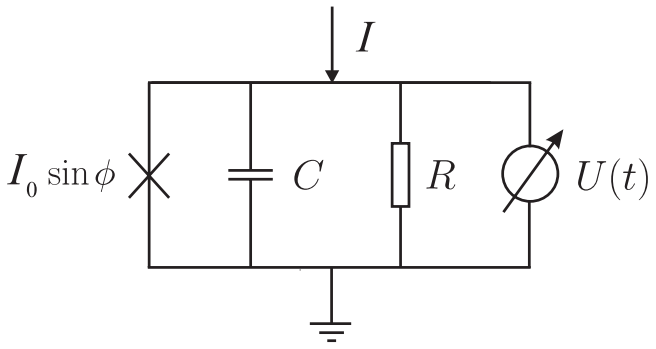

Figure 2.2: Circuit model of the RCSJ theory. R represents the resistance for the single electron current and C is the finite capacitance of the junction. $I_0 \sin(\phi)$ is the tunnelling current through the 'ideal' Josephson junction and I is the total current driven through the RCSJ.

pair tunnelling current $I_{cp} = I_0 \sin\phi$, a single electron tunnelling current $I_{se} = \frac{U}{R}$ and a displacement current $I_C = C\frac{\partial}{\partial t}U$:

$$I = C\frac{\partial}{\partial t}U + \frac{U}{R} + I_0 \sin\phi$$

Here $I_0 = AJ_0$ with A representing the cross section of the superconductor. Using (2.6) and $U = \frac{E_R - E_L}{2e}$, we obtain a differential equation describing the time dependance of the phase difference across the junction:

$$I = \frac{\hbar C}{2e}\frac{\partial^2}{\partial t^2}\phi + \frac{\hbar}{2eR}\frac{\partial}{\partial t}\phi + I_0 \sin\phi \tag{2.8}$$

In the case of small currents driven through the RCSJ, i.e. $I \to 0$ and only small relative phases $|\phi| \ll \pi/2$, equation (2.8) can be linearised showing that the phase difference across the Josephson junction oscillates with the plasma frequency $\omega_p = \frac{2eI_0}{\hbar C}$.
The behaviour for larger currents cannot be as easily derived from (2.8), since the equation is not solvable analytically. However, it is of the same form as the equation of motion of a rigid pendulum which is driven by an external torque. By comparing the RCSJ model with the pendulum, we can thus gain intuitive insight into the way how a real Josephson junction reacts to a current driven through it by means of an external voltage. A picture of the pendulum is shown in figure 2.3. Equation (2.9) represents the

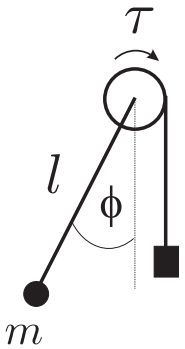

Figure 2.3: Rigid pendulum of length l and mass m, driven by an external torque τ. ϕ is the angular deviation.

equation of motion of the pendulum of length l and mass m:

$$\tau = M\frac{\partial^2}{\partial t^2}\phi + D\frac{\partial}{\partial t}\phi + mgl\sin\phi \tag{2.9}$$

Here, τ is the external constant torque, $M = ml^2$ represents the moment of inertia, D is a damping coefficient and g the acceleration of gravity. Table 2.1 opposes the corresponding parameters of both models.

RCSJ-Model				**Rigid Pendulum Model**
applied current	I	$\leftrightarrow$	τ	external torque
average (dc) voltage term	$\frac{2e}{\hbar}U_{dc}$	$\leftrightarrow$	$\omega = \frac{\partial}{\partial t}\phi$	average angular velocity
phase difference	ϕ	$\leftrightarrow$	ϕ	angular displacement
capacitance term	$\frac{\hbar}{2e}C$	$\leftrightarrow$	M	moment of inertia
critical current	I_0	$\leftrightarrow$	mgl	critical torque

Table 2.1: List of equivalent parameters in the RCSJ-model and the rigid pendulum model, repsectively.

We can now distill three different dynamical regimes:

- $\tau = 0$: This is the case of $I = 0$ discussed above.
- $0 < |\tau| < mgl$: In this case the pendulum has its resting position at $|\phi| \neq 0$, as depicted in figure 2.3. In the case of the Josephson junction this corresponds to the situation where $0 < I < I_0$: The current driven through the RCSJ is smaller than the maximum Cooper pair tunnelling current I_0, therefore the whole charge transport can be performed by unresistant Cooper pair tunnelling without voltage drop across the junction.
  Although the pendulum may oscillate around its deviated resting position, the average angular momentum is zero, corresponding to a zero time averaged voltage drop $U_{dc} = \frac{\hbar}{2e}\langle\frac{\partial}{\partial t}\phi\rangle_t$ across the junction. Due to the damping term (i.e. the finite resistance), these oscillations will damp out anyway.
- $|\tau| > mgl$: Now the torque is large enough so that the pendulum overcomes the top position and starts to rotate with a non vanishing angular velocity $\frac{\partial}{\partial t}\phi$. This corresponds to the case of $I > I_0$, meaning that the driving current is too large for Cooper pair tunnelling alone and a single electron tunnelling current I_{se} will appear, leading to a finite voltage drop across the junction. The current I_{cp} will therefore be oscillating, due to the AC-Josephson effect. For large currents I, the AC-Josephson current can be neglected and the current-voltage characteristic for the RCSJ is linear according to Ohm's law: $I = \frac{U}{R}$

The current-voltage characteristics of a Josephson junction as predicted by the RCSJ model is depicted in figure 2.3 by the red curve (solid and dashed).
Note that the RCSJ model has a major flaw: It assumes a constant single electron tunnelling resistance R. This, however, is not the case in real Josephson junctions. In fact, R depends strongly nonlinearly on the external voltage; single electrons can only

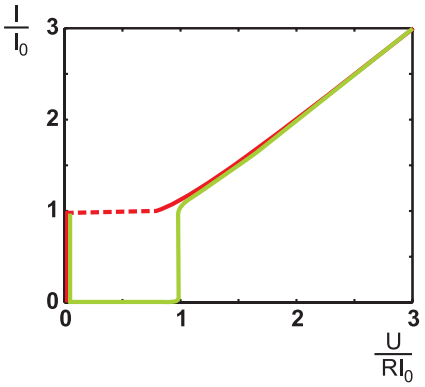

Figure 2.4: The current-voltage characteristics of the RCSJ model is depicted by the red line (solid and dashed). Note that the dashed part is actually never measured due to the non-linearity of R with respect to U (see text). This part of the curve is modelled falsely. Experimentally measured current-voltage curves therefore resemble the green line.

tunnel through the barrier if a voltage $U \geq (\Delta_L + \Delta_R)/e$ is applied, where Δ_L and Δ_R represent the band energy gaps of the left and right superconductor, respectively [41]. This has the effect that a voltage drop of $U < (\Delta_L + \Delta_R)/e$ across the Josephson junction is never measured. Instead, for currents $I > I_0$ the voltage suddenly jumps to $U = (\Delta_L + \Delta_R)/e$. The dashed red line in figure 2.3 is therefore not seen in experiments, this region is falsely explained by the RCSJ model. A typical experimental current-voltage curve of a Josephson junction instead follows the green line. It can be seen, however, that the other regions of the current-voltage characteristics are captured quite well by the RCSJ model.

Chapter 3

Theory of the Bose-Einstein Josephson Junction

In this chapter the theoretical description of a Bose-Einstein Josephson junction (BJJ) is discussed. A Bose-Einstein Josephson junction is defined as two Bose-Einstein condensates separated by a thin tunnelling barrier in analogy to the superconducting Josephson junctions (SJJ). The macroscopic wave function which describes the Cooper pairs in the superconducting case is now describing the bosonic atoms (^{87}Rb in our case) which are Bose-Einstein condensed. Therefore, the basic features of the dynamics of such a coupled system can be described by using the same methods as for the SJJ case (section 2). Before doing this in section 3.2, however, we will shortly revise the most important aspects of Bose-Einstein condensation and introduce a mean field model, the so called Gross-Pitaevskii equation, which describes the dynamical behaviour of a Bose-Einstein condensate (BEC). A numerical method in order to actually compute the dynamics of a BEC will then be introduced in section 3.3.

3.1 The Bose-Einstein Condensate

3.1.1 Condensation of Bosonic Atoms

The theory of Bose-Einstein condensation, first developed by Einstein [4] in 1925 based on quantum statistical considerations by Bose [5] can nowadays be found in most textbooks on statistical mechanics such as [44] and in numerous review articles, e.g. in [45, 46, 47]. This effect is best described in the grand canonical ensemble. Neglecting the interaction of the particles for a while, we consider an ideal gas of N bosonic atoms in an external potential $U(\mathbf{r})$. The atoms will occupy the single particle states with eigenenergies ϵ_i according to the Bose distribution

$$\langle n_i \rangle = \frac{1}{\exp\left[\frac{\epsilon_i - \mu}{k_B T}\right] - 1}, \tag{3.1}$$

where $\langle n_i \rangle$ is the number of atoms in the state i, μ is the chemical potential, k_B the Boltzmann factor and T the temperature of the gas. N is therefore given by

$$N = \sum_i \langle n_i \rangle. \tag{3.2}$$

It can be seen from equation 3.1 that $\epsilon_i > \mu$ since otherwise the number of atoms would be negative or the denominator would become 0. We will now consider the number of atoms which can be found in the excited states, if we lower the temperature $T \to 0$. In this case $\mu \to \epsilon_0$ until it reaches ϵ_0 at a critical temperature T_c. We can therefore set the energy of the lowest state $\epsilon_0 = \mu$ but exclude this state from the summation in order to prevent the problem mentioned above:

$$N - N_0 = \int_{\epsilon \neq \epsilon_0}^{\infty} \frac{g(\epsilon)}{\exp\left[\frac{\epsilon_i - \mu}{k_B T}\right] - 1} d\epsilon \tag{3.3}$$

N_0 is defined as the number of atoms in the ground state and $g(\epsilon)$ is the density of states. We exchanged the sum in (3.2) by an integral following the usual semiclassical approximation. This integral is finite for $g(\epsilon)$ of typical three-dimensional traps, showing that only a finite number of atoms can occupy the excited states on average. If the total number of atoms N exceeds this value, the atoms can only evade into the ground state which was excluded in our integral. The ground state therefore becomes macroscopically occupied: Bose-Einstein condensation takes place. For a homogeneous three-dimensional system, the condensation sets in if the following criterion for the phase space density $n\lambda_{dB}^3$ is fulfilled:

$$n\lambda_{dB}^3 = \zeta(3/2) \approx 2.61 \tag{3.4}$$

Here, n is the density of the bosons and $\lambda_{dB} = \frac{h}{\sqrt{2\pi m k_B T}}$ is the thermal de Broglie wavelength of the atoms. ζ is Riemann's zeta function. This criterion can be interpreted figuratively: the condensation sets in when the quantum mechanical wave functions start to overlap spatially.
In order to find a typical critical temperature for this phase transition, we will now consider the case of a three-dimensional harmonic trap which can be found in most experimental realisations. The trapping frequencies in x-, y- and z-direction are ω_x, ω_y and ω_z. For the density of states we get

$$g(\epsilon) = \frac{1}{2}(\hbar\bar{\omega})^{-3}\epsilon^2, \tag{3.5}$$

with $\bar{\omega} = (\omega_x \omega_y \omega_z)^{\frac{1}{3}}$ representing the mean trapping frequency. As mentioned, Bose-Einstein condensation takes place if the number of atoms in the ground state becomes larger than zero. If we insert (3.5) into (3.3) we get for this case:

$$k_B T_C = \hbar\bar{\omega}\left(\frac{N}{\zeta(3)}\right)^{\frac{1}{3}} \approx 0.94\,\hbar\bar{\omega}N^{\frac{1}{3}}. \tag{3.6}$$

Considering typical trap frequencies of $2\pi \times 80\,\mathrm{Hz}$ and $N = 1000$ such as in the case of our experiments we get a critical temperature $T_C = 40\,\mathrm{nK}$. In this case a fraction of

$$\frac{N_0}{N} = 1 - \left(\frac{T}{T_c}\right)^3 \tag{3.7}$$

atoms is in the condensed phase.
These considerations assumed the thermodynamic limit $N \to \infty$ and neglected the atomic interaction. They are, however, still valid with small corrections for dilute gases, i.e. $na^3 \ll 1$, where n is the atomic density and a is the s-wave scattering cross section of the atoms ($a = +5.32\,\mathrm{nm}$ for ^{87}Rb).

3.1.2 Description of BEC Dynamics: The Gross-Pitaevskii Equation

Once having obtained a Bose-Einstein condensate it is of course desirable to describe the dynamical behaviour of this macroscopic quantum wave function. For large N, however, the system of coupled differential equations describing the interacting atoms is difficult to solve even numerically. The established standard method for describing Bose-Einstein condensates therefore is a mean field model, the so called 'Gross-Pitaevskii-Equation' or 'GPE', derived by Gross [48, 49] and Pitaevskii [50] in 1961. It assumes a dilute gas and low temperature, where the interaction between the atoms is mainly given by elastic s-wave scattering. In that case, the interaction potential of the atoms can be reduced to a delta potential $U(\mathbf{r} - \mathbf{r}') = g_{3d}\delta(\mathbf{r} - \mathbf{r}')$ with

$$g_{3d} = \frac{4\pi\hbar^2 a}{m} \tag{3.8}$$

being the so called threedimensional coupling constant. m is the mass of the atoms. a is positive in the case of repulsive interaction such as for ^{87}Rb and negative for attractive interaction. Despite these approximations the GPE is a very good tool to describe the dynamics of Bose-Einstein condensates. It reads

$$i\hbar\frac{\partial}{\partial t}\Psi(\mathbf{r},t) = \left[-\frac{\hbar^2}{2m}\Delta + V_{ext}(\mathbf{r}) + g_{3d}N\left|\Psi(\mathbf{r},t)\right|^2\right]\Psi(\mathbf{r},t). \tag{3.9}$$

$\Psi(\mathbf{r},t)$ represents the effective one body wave function of the Bose-Einstein condensate and is normalised to the number of atoms N. $V_{ext}(\mathbf{r})$ is the external potential.
The equation would be of the same form as the linear Schrödinger equation, if it were not for the last term in the brackets on the right side. This nonlinear term in $\Psi(\mathbf{r},t)$ is due to the interaction between the atoms and gives rise to numerous interesting phenomena in the dynamics of Bose-Einstein condensates.

3.2 Two Mode Model of the Bose-Einstein Josephson Junction

The Bose-Einstein Josephson junction consists of two BECs that are coupled by a tunnelling barrier, similar to the case of superconducting Josephson junctions. Such a

situation can be realised by a harmonic external potential which has a 'bump' in the centre, such as depicted in figure 3.1 with the solid black line.. In analogy to section 2.1

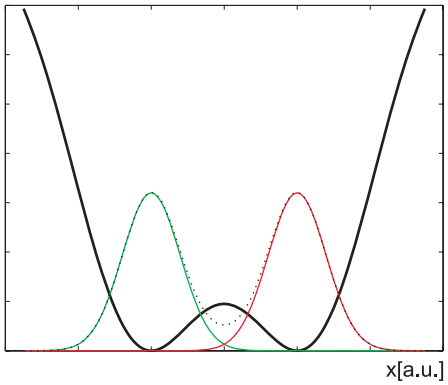

Figure 3.1: Sample picture of a BEC in a one-dimensional double well confinement. The solid black curve represents V_{ext}, the green curve shows $|\Psi_L|^2$, the red curve $|\Psi_R|^2$. The dotted black line depicts $|\Psi|^2 = |\Psi_L + \Psi_R|^2$

we can express the overall BEC wave function $\Psi(\mathbf{r}, t)$ by the sum of the wave functions of the BEC in the left well, $\Psi_L(\mathbf{r}, t)$ (green curve), and in the right well, $\Psi_R(\mathbf{r}, t)$ (red curve), respectively.

$$\Psi(\mathbf{r}, t) = \Psi_L(\mathbf{r}, t) + \Psi_R(\mathbf{r}, t) \tag{3.10}$$

Note, that (3.10) represents an approximation since the superposition principle of two wave functions is not correct in this case due to the nonlinear term in the Gross-Pitaevskii equation (3.9). This ansatz is, however, valid for small spatial overlaps of the two wave functions. It has first been used by Javanainen in 1986 [21] but this work did not consider the effects arising from the on-site interaction between the atoms. We will see later that this interaction gives rise to a variety of dynamical regimes [24, 22, 23] which cannot be found in the superconducting Josephson case.
In order to gain insight into the dynamics of two weakly linked BECs, we will therefore follow the derivation of [23]. Although this simple two mode model is not capable of describing the dynamics of the coupled BECs quantitatively for the parameter range that was used in the experiments described in section 5, it can show all accessible dynamical regimes in a qualitative and intuitive way. Its elegancy originates from the fact that the complete dynamics can be characterised by only two variables, the difference of atom numbers in the two wells z and the phase difference of both condensates, called ϕ. This is all in close analogy the the familiar SJJ case. In order to calculate the dynamics quantitatively, however, numerical methods for solving the GPE have to be applied, such as described in section 3.3 or the two mode model has to be extended as shown in [51]. The limits of the two mode model are discussed in more detail in [52].
In the two mode model the wave functions $\Psi_{L,R}(\mathbf{r}, t)$ are defined as:

$$\begin{aligned} \Psi_{L,R}(\mathbf{r}, t) &= \psi_{L,R}(t)\Phi_{L,R}(\mathbf{r}) \\ \Rightarrow \Psi(\mathbf{r}, t) &= \psi_L(t)\Phi_L(\mathbf{r}) + \psi_R(t)\Phi_R(\mathbf{r}) \end{aligned} \tag{3.11}$$

The time dependent part is given by

$$\psi_{L,R}(t) = \sqrt{N_{L,R}(t)}e^{i\phi_{L,R}(t)}, \tag{3.12}$$

where $N_{L,R}$ are the numbers of atoms in the left and right well, respectively and $\phi_{L,R}(t)$ represents the phase of each wave function. Note that the phase is assumed to be spatially constant for each condensate but may vary in time.
The spatially dependent part of $\Psi_{L,R}(\mathbf{r},t)$ is defined as a linear combination of the lowest symmetric $\Phi_s(\mathbf{r})$ and antisymmetric $\Phi_{as}(\mathbf{r})$ stationary eigenstates of the coupled system:

$$\begin{aligned}\Phi_L(\mathbf{r}) &= \frac{\Phi_s(\mathbf{r}) + \Phi_{as}(\mathbf{r})}{\sqrt{2}} \\ \Phi_R(\mathbf{r}) &= \frac{\Phi_s(\mathbf{r}) - \Phi_{as}(\mathbf{r})}{\sqrt{2}}\end{aligned} \tag{3.13}$$

The shape of the two wave functions is therefore assumed to remain constant over time, which is not necessarily the case in the real situation. This will lead to false predictions concerning the time dependence of the dynamics.
Again following the analogy of the superconducting Josephson junction, we insert (3.11) into the GPE (3.9) and get after multiplying with $\Phi_L^*(\mathbf{r})$ and integrating over the spatial dimensions:

$$\begin{aligned}&i\hbar\frac{\partial}{\partial_t}\psi_L(t) = \\ &\left(\int\left[-\frac{\hbar^2}{2m}\Phi_L\nabla^2\Phi_L + \Phi_L^2 V_{ext} + N_L\Phi_L^4 g + \Phi_L^3\Phi_R\psi_R^*\psi_L g + 2N_R\Phi_L^2\Phi_R^2 g\right]dV\right)\psi_L \\ &+\left(\int\left[-\frac{\hbar^2}{2m}\Phi_L\nabla^2\Phi_R + \Phi_L V_{ext}\Phi_R\right]dV\right)\psi_R \\ &+\left(\int\left[N_R\Phi_L\Phi_R^3 g + \Phi_L^2\Phi_R^2\psi_L^*\psi_R g + 2N_L|\Phi_L|^3\Phi_R\ g\right]dV\right)\psi_R\end{aligned} \tag{3.14}$$

The corresponding equation is obtained for $\psi_R(t)$. We will neglect all mixed terms except for those in the second integral, since we are only considering the interaction of atoms in the same well (on-site interaction). This approximation is valid for a small spatial overlap of the wave functions. By defining the constant parameters

$$E_{L,R}^0 = \int\left[\frac{\hbar^2}{2m}|\nabla\Phi_{L,R}|^2 + |\Phi_{L,R}|^2 V_{ext}\right]dV, \tag{3.15}$$

$$K = -\int\left[\frac{\hbar^2}{2m}\nabla\Phi_L\nabla\Phi_R + \Phi_L V_{ext}\Phi_R\right]dV, \tag{3.16}$$

$$U_{L,R} = g\int|\Phi_{L,R}|^4 dV, \tag{3.17}$$

we get two coupled equations for the time dependent part of the wave functions in the two wells

$$\begin{aligned} i\hbar\frac{\partial}{\partial t}\psi_L &= (E_L^0 + U_L N_L)\psi_L - K\psi_R, \\ i\hbar\frac{\partial}{\partial t}\psi_R &= (E_R^0 + U_R N_R)\psi_R - K\psi_L. \end{aligned} \tag{3.18}$$

These equations resemble (2.1) of the SJJ case in section 2.1 except for the on-site interaction energy terms $U_L N_L$ and $U_R N_R$. Note, that the minus sign in (3.18) is due to the definition of the coupling constant K in (3.16).
We proceed as in section 2.1 by defining the relative phase of the two wave functions

$$\phi(t) = \phi_R(t) - \phi_L(t) \tag{3.19}$$

and additionally the relative population imbalance

$$z(t) = \frac{N_L(t) - N_R(t)}{N_T}, \tag{3.20}$$

where $N_T = N_L + N_R$ is the total number of atoms. In the case of the SJJ, the population imbalance could be ignored due to the current source replacing the tunnelling Cooper paired electrons. In the BJJ, atoms tunnelling from one well to the other cannot be replaced by an external circuit substitute of whatever kind, therefore we have to take a population difference into account.
Solving the equations in (3.18) by inserting $\psi_{L,R}(t)$ and proceeding similarly as in section 2.1, we get the following differential equations describing the tunnelling dynamics:

$$\dot{\phi}(t) = \Delta E + \Lambda z(t) + \frac{z(t)}{\sqrt{1 - z^2(t)}}\cos(\phi(t)) \tag{3.21}$$

$$\dot{z}(t) = -\sqrt{1 - z^2(t)}\sin(\phi(t)) \tag{3.22}$$

Time in this case is expressed in units of $\frac{\hbar}{2K}$ and the introduced dimensionless parameters are defined as

$$\Delta E = \frac{(E_L^0 - E_R^0)}{2K} + \frac{U_L - U_R}{4K}N_T, \tag{3.23}$$

$$\Lambda = \frac{(U_L + U_R)N_T}{4K}. \tag{3.24}$$

Comparing (2.6) of the SJJ case and (3.21) we notice additional energy terms arising from the on-site interaction. Therefore, for $z(t) \neq 0$ the relative phase between the two wave functions can change over time due to the nonzero Λ even if no external potential difference is present between the two wells, i.e. $E_L^0 = E_R^0$ and even if $U_L = U_R$. This is in

contrast to the DC Josephson effect, where $\phi(t)$ remained constant in time for $\Delta E = 0$. For an initial population difference we will therefore get an increasing phase difference due to the unequal on-site interaction energies of the two wells. The asymmetric BEC in the double well potential generates its own potential difference without the need of an external voltage as in the SJJ case. One can thus speak of a 'self generated AC Josephson effect' due to the interaction of the atoms. There are therefore in principle two different possibilities to initiate tunnelling dynamics in a Bose-Einstein Josephson junction with no external potential:
Firstly, starting with an initial nonzero phase difference will initiate a tunnelling current as in the DC SJJ case. We will call this method 'phase induced Josephson oscillations'. Secondly, we can also begin with zero initial phase difference but initial population imbalance; due to the self generated energy difference of the wave functions, a phase difference will evolve according to (3.21) and initiate the tunnelling dynamics. This method shall be called 'population-imbalance induced Josephson oscillations'.
If we compare the expression for the tunnelling current in the case of the SJJ (2.7) and of the Bose-Einstein Josephson junction (3.22), we also note that the maximum tunnelling current density J_0 which was constant in the SJJ case is now depending on the population imbalance. The minus sign in (3.22) originates from the definition of $\phi(t)$ in (3.19).
In order to gain insight into the actual dynamics of the system, which is described by the coupled differential equations (3.21) and (3.22), we will now again consider a mechanical pendulum analogue.
Equations (3.21) and (3.22) describe a non-rigid pendulum of deviation angle $\phi(t)$ and angular momentum $z(t)$. 'Non-rigid' in this case means that the length l of the pendulum is not constant but obeys the particular equation $l = \sqrt{1 - z^2}$ and is thus coupled to the angular momentum. Other than in section 2.3 this pendulum model does not experience external torque. We will now look at different regimes of these pendulum motions for the case of a symmetric double well confinement, i.e. $E_L = E_R$.

3.2.1 Josephson Oscillation Regime

This regime covers oscillations of the pendulum around its resting position $\phi = 0$.

Non-Interacting Limit

For no atomic interaction, i.e. $U_L = U_R = 0$, the coupled differential equations (3.21) and (3.22) reduce to

$$\ddot{z}(t) = -z(t). \tag{3.25}$$

We therefore get sinusoidal oscillations of the population imbalance. These oscillations with frequency 1, corresponding to $\omega_R = \frac{2K}{\hbar}$ in unscaled time, can be interpreted as Rabi-oscillations [22]. The oscillations of the pendulum or the phase and population difference, respectively, are shown in figure 3.2(a) with dotted red lines. Note, that this limit is not easily accessible for ^{87}Rb. Although in principle the interaction can be tuned and also turned to zero by means of Feshbach resonances, they are difficult to implement in the case of ^{87}Rb. This limit could therefore not be studied experimentally. It would, however, be possible to look at for Cs BECs, which are well tunable by Feshbach resonances [53].

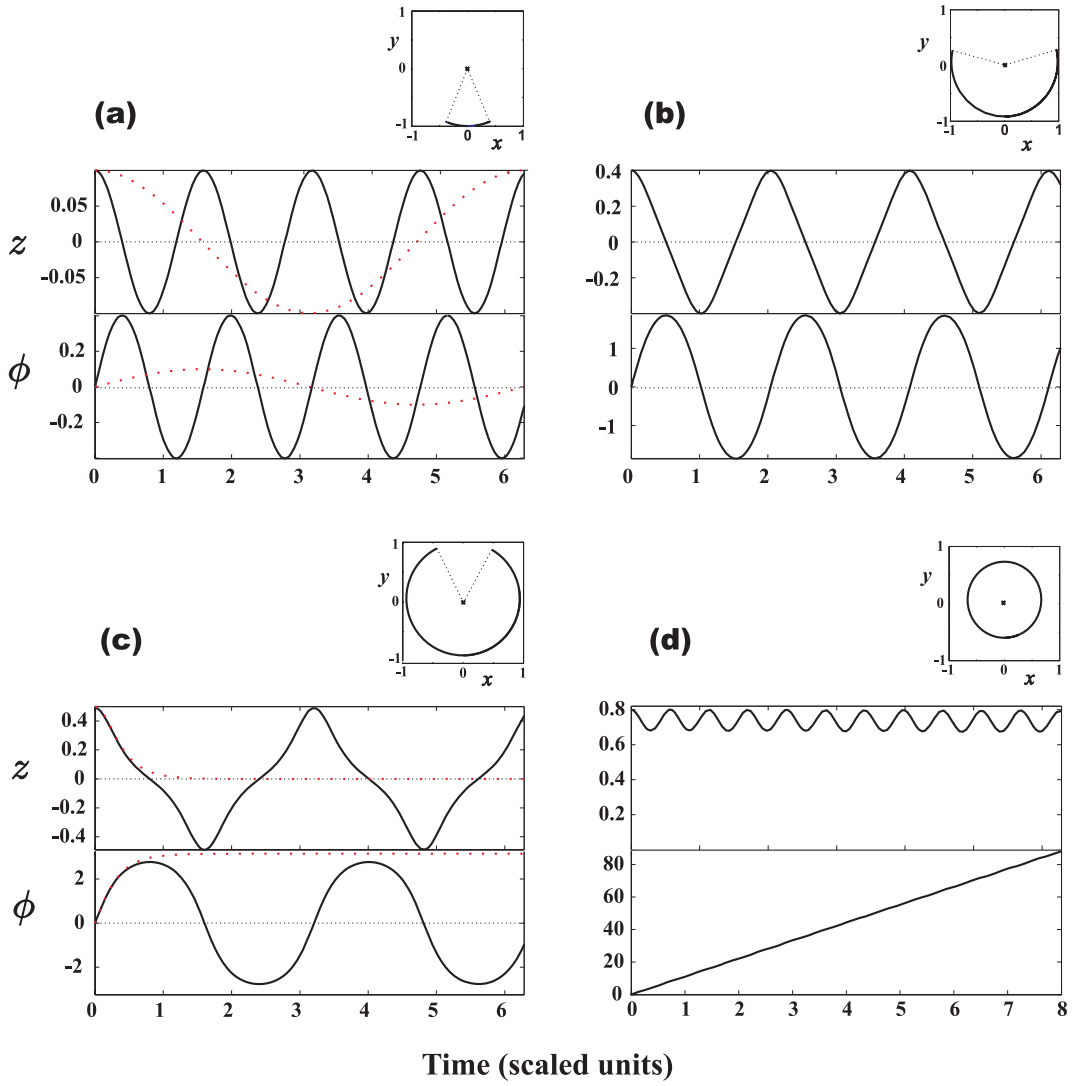

Figure 3.2: This figure depicts the different dynamical regimes of the BJJ for $\Lambda = 15$ (solid black lines). The small squared figures in (a),(b),(c),(d) represent the deviation range of the model pendulum for the corresponding dynamics. (a) shows the non-interacting limit ($\Lambda = 0$, red dotted line) and the small amplitude limit (black solid line) with $z(0) = 0.1$. Sinusoidal oscillations in $\phi(t)$ and $z(t)$ can be observed. (b) shows the case of $z(0) = 0.4$: for larger amplitudes the oscillations become anharmonic. (c) depicts the case of very large amplitudes with $z(0) = 4.9$ (solid line) and the critical case where the initial 'kick' of the pendulum is sufficient so that it comes to rest at its top position (red dotted line), corresponding to $z(0) = z_c = 0.499$. (d) shows the self-trapping regime for $z(0) = 0.8$. In the mechanical model this corresponds to a rotating pendulum. For $z(t)$ small amplitude oscillations of high frequency can be observed in this case, since $z(t)$ varies during one rotation. The phase difference winds up quasi linearly with overlaying small amplitude oscillations.

Small Amplitude Limit

The equations (3.21) and (3.22) can also be reduced to a more simple form by linearising them in the case of small amplitude oscillations, i.e. $|z(t)| \ll 1$ and $|\phi(t)| \ll 1$:

$$\dot{\phi}(t) = (\Lambda + 1)z(t) \tag{3.26}$$
$$\dot{z}(t) = -\phi \tag{3.27}$$

Inserting (3.26) into (3.27) we get:

$$\ddot{z}(t) = -(\Lambda + 1)z(t) \tag{3.28}$$

These are oscillations with a frequency of $\omega_{pl} = \sqrt{\Lambda + 1}\frac{2K}{\hbar}$ and are often called 'plasma oscillations' in analogy to superconducting Josephson junctions. In the latter case, however, the plasma frequencies are on the order of several GHz as compared to $\omega_{pl} \approx 2\pi \times 30\,\mathrm{Hz}$ for a typical Bose-Einstein Josephson junction. These sinusoidal oscillations are shown in figure 3.2(a) (black solid line) for $\Lambda = 15$ and $z(0) = 0.1$.
This limit is also not easily accessed experimentally, due to the fact that such small population imbalances are both difficult to implement and to measure.

Large Amplitude Oscillations

For larger initial population or phase imbalances the anharmonic character of equations (3.21) and (3.22) becomes more and more important and the oscillations become non-sinusoidal. Figure 3.2(b) shows the case of $z(0) = 0.4$ and figure 3.2(c) depicts the oscillations for $z(0) = 0.49$. Note, that all these figures show the case of population-imbalance induced Josephson oscillations, corresponding to the case of zero angular deviation but initial angular momentum in the pendulum analogue.
The borderline case is reached, if we give the pendulum a kick $z(0) = z_c$ that is large enough such that it reaches its top position. Due to the dependence of the length l on the angular momentum, this position is a stable one. The pendulum therefore stops at $\phi = \pi$ which means that $z = 0$, i.e. the population becomes balanced with a phase difference of π between both sides. This case is depicted by the red dots in figure 3.2(c) for $z_c = 0.499$.

3.2.2 Self-Trapping Regime

We will now consider the case where the pendulum has enough initial angular momentum to overcome its top position and starts rotating with non vanishing angular momentum $z(t)$. This means that for a very large initial population imbalance the oscillations described above will not be seen any more but instead the initial population imbalance remains locked apart from small amplitude oscillations. They are due to the fact that the pendulum angular momentum slightly varies during one rotation. In other words: No full amplitude tunnelling oscillations occur, there will always remain more atoms in the well that had a larger initial population as shown in 3.2(d) for the case $z(0) = 0.8$. This surprising result is called 'macroscopic quantum self-trapping'. It results from the interaction of the atoms and cannot be seen in superconducting Josephson junctions.
Note that the case of the rotating pendulum in the analogue used for explaining the RCSJ is different: The rotation was due to an external torque, i.e. a driving current in the Josephson junction picture and was independent of the initial condition of the population or the phase.
The transition from oscillatory to self-trapping behaviour is a sudden one as can be nicely seen in the pendulum analogue. For initial $\phi(0) = 0$, it happens at the critical initial population imbalance $z(0) = z_c$ which can be deduced by considering the total energy H of the system, which is constant and given by

$$H = \frac{\Lambda z^2(t)}{2} + \Delta E z(t) - \sqrt{1 - z^2(t)} \cos \phi(t). \tag{3.29}$$

The initial angular momentum has to be large enough such that $\phi_{final} = \pi$ and $z_{final} = 0$ which corresponds to $H = 1$. Therefore:

$$\frac{\Lambda z_c^2}{2} + \Delta E z_c - \sqrt{1 - z_t^2} \cos \phi(0) \stackrel{!}{=} 1 \tag{3.30}$$

For $\phi(0) = 0$ this equation is only solvable for $\Lambda > 2$ in which case we get

$$z_c = \frac{2\sqrt{\Lambda - 1}}{\Lambda}. \tag{3.31}$$

3.2.3 π-Phase Modes

Other fascinating dynamical regimes are the so called 'π phase modes'. They are defined as oscillations with $\langle \phi(t) \rangle_t = \pi$. Looking at it in the pendulum model this means that the pendulum is oscillating around its top position, while never reaching $\phi(t) = 0$. This is possible due to the fact that the length of the pendulum is dependent on the angular momentum, resulting in a stable top position. These oscillations, however, are almost not accessible experimentally and will therefore not be further discussed here. For a detailed investigation, please see [23] and [52].

3.3 Numerical Simulations of the Bose-Einstein Josephson Dynamics

The numerical method used for all simulations in this thesis is the non-polynomial nonlinear Schrödinger equation method (NPSE) developed by Luca Salasnich [54]. The NPSE is a quasi three-dimensional equation specially designed for cigar shaped BECs in elongated traps. In this case the dynamics is restricted to the longitudinal direction. The NPSE does on the other hand assume a Gaussian shape for the lateral dimensions of the condensate and therefore takes the three-dimensional shape of a real BEC into account. Lateral excitations, however, are not captured by this model.
The model has been tested in [54, 55] and also in the context of the Josephson oscillations in [52] and is described there in more detail. It shows excellent agreement with the full three-dimensional solution of the GPE and the experimentally obtained data while reducing computation time to a fraction of what is needed when solving the full three-dimensional GPE. The simulations have been performed with MatLab.

Chapter 4

Experimental Setup

In order to obtain a Bose-Einstein condensate in a double well potential, the atoms need to be trapped and condensed. The apparatus creating the BECs will now shortly be described, as well as how the atoms are trapped and cooled and how the double well potential is implemented in the experiment. The basic setup of the apparatus has already been described in many publications, such as [52, 55, 56, 57, 58]. The focus will therefore be put on modifications and analyses of the setup that have been performed in the framework of this thesis. This concerns e.g. the stabilisation analysis of the X-DT beam and the modification of the standing wave setup (4.2.2) and especially the thorough analysis of the imaging system (section 4.3.1).
In anticipation of the following sections, a sketch showing the optical and vacuum setup is depicted in figure 4.1 as a reference.

4.1 Gathering and Condensing ^{87}Rb Atoms

4.1.1 Collecting Atoms in the MOT

In order to be able to cool atoms to the nanokelvin range, any contact to other matter at laboratory temperature has to be prevented. Therefore an ultra high vacuum of below 10^{-11} mbar is used. Figure 4.2 shows a drawing of the vacuum chamber. The ^{87}Rb is provided by electrically heated dispensers in the left part of the chamber. Due to the dispensers in the chamber, however, a pressure of below $\approx 10^{-9}$ mbar is not feasible. The vacuum chamber is therefore separated into two segments by a differential pumping stage, consisting of a small tube. The left side of the chamber (yellow in figure 4.2) contains the dispenser and the right part (blue in figure 4.2) contains the glass cell where the actual condensation takes place. The pressure in the right part is below 10^{-11} mbar.
The atoms are gathered on the left side (funnel chamber) by a two dimensional magneto optical trap (MOT) whose laser beams are indicated by the red arrows. For the detailed description of the working principles of a MOT refer to e.g. [59]. The atoms are then 'pushed' by another laser beam (shown on the left edge of figure 4.2) through the tube of the differential pumping stage, producing a continuous beam of cold atoms. They are collected in a three-dimensional MOT in the right part of the chamber.
The loading rate of the MOT on the right hand side is $\approx 2 \times 10^7$ atoms/s and the temperature of the atoms in the MOT is $\approx 160\,\mu$K. The laser providing the MOT beams is a titanium sapphire (Ti:Sa I) laser (*Coherent MBR 110*) pumped by a frequency

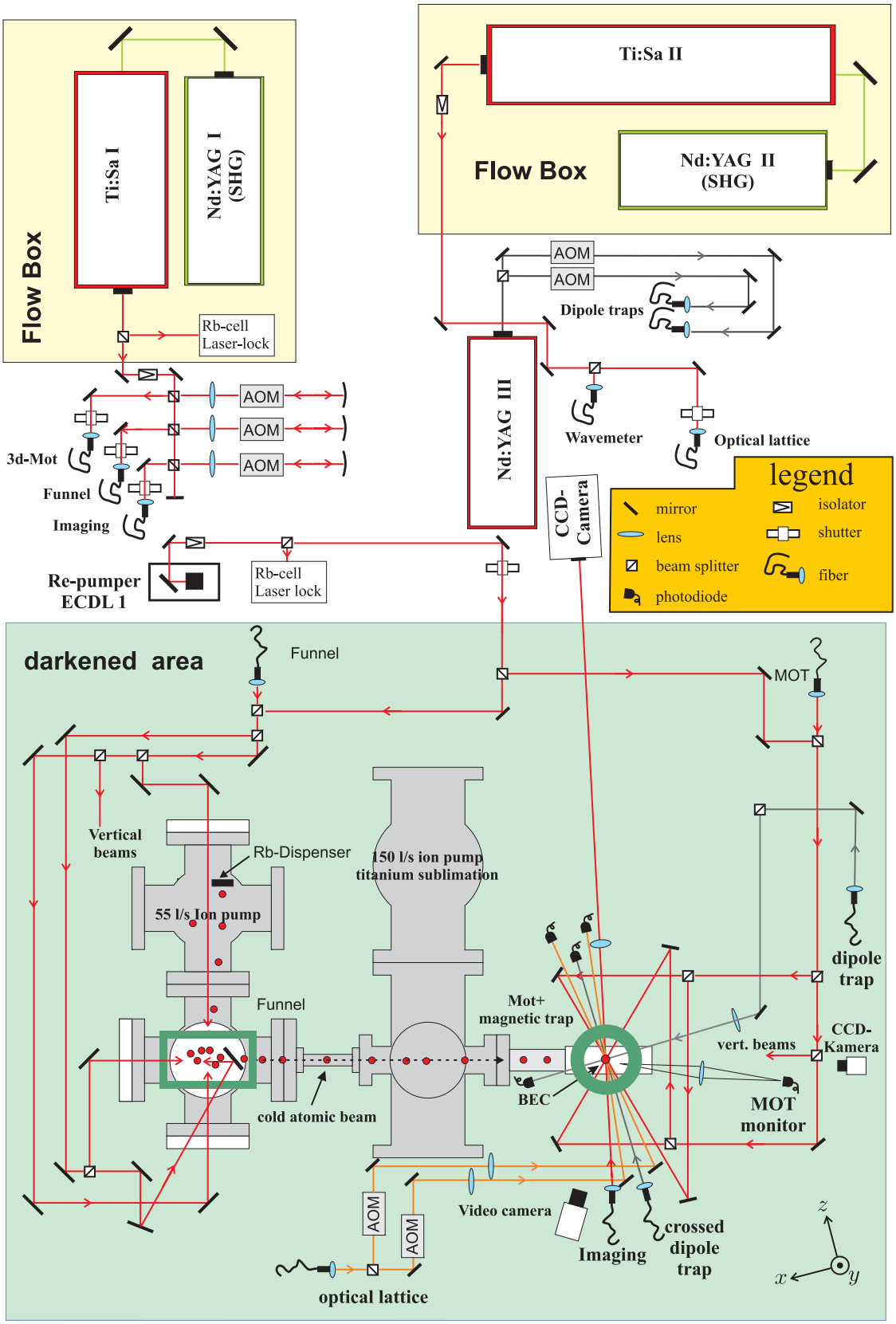

Figure 4.1: Sketch showing the setup on the optical table. The upper part depicts the preparation of the laser light which is then transferred by optical fibres to the darkened experimental region (green shaded area). Here, the vacuum chamber is placed where the atoms are cooled, trapped and finally Bose-Einstein condensed.

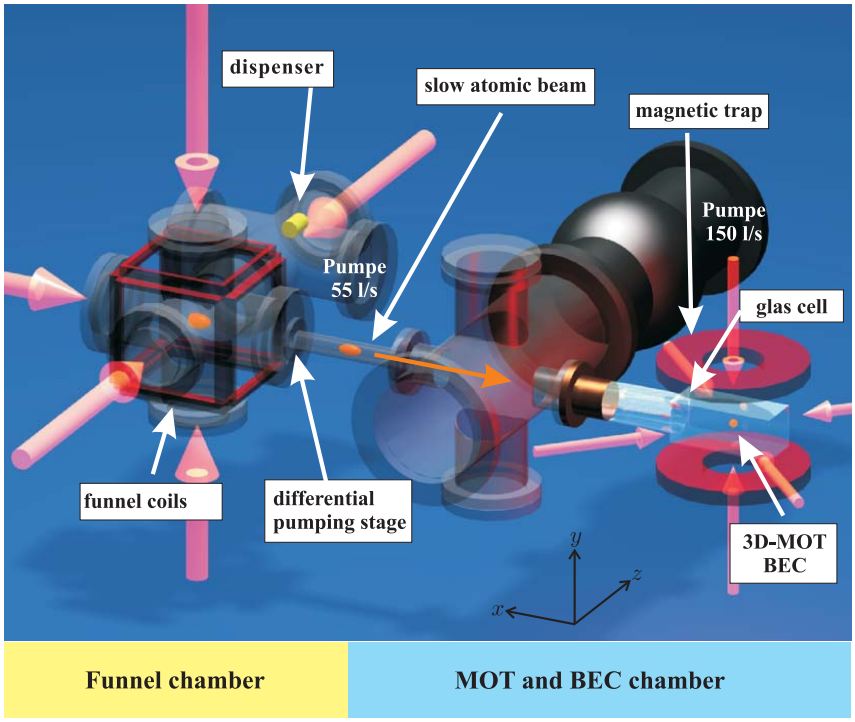

Figure 4.2: Drawing of the vacuum chamber. The left part (yellow region) has a pressure of $\approx 10^{-9}$mbar and is separated from the right part which has a pressure of below 10^{-11}mbar (blue region) by a differential pumping stage. The funnel on the left side provides a beam of cold atoms which is collected by the MOT in the glass cell on the right side.

doubled Nd:YAG laser (*Coherent Verdi V10*) and is locked to the ($F = 2 \rightarrow F' = 3$) crossover of ^{87}Rb by means of Doppler-free absorption spectroscopy. The hyperfine structure of ^{87}Rb is depicted in figure 4.3.
Please note that a part of the atoms drops out of the ($F = 2 \rightarrow F' = 3$) cycle and decays to the $5S_{1/2}$ state. Therefore a repumping laser is needed in order to bring these atoms back into the cycle. The repumper is provided by an external cavity diode laser (ECDL 1, 100 mW output power) which is locked to the ($F = 1 \rightarrow F' = 2$) transition as shown in figure 4.3.
The laser light is transferred to the vacuum chamber by means of optical fibres. The atom number in the MOT can be monitored by a photodiode which collects a part of the fluorescent light of the atoms. As soon as enough atoms are in the MOT, typically around 2×10^8, the cloud is further cooled by optical molasses cooling. It then has a temperature of $40 - 50\,\mu$K and a phase space density of $\Omega \approx 3 \times 10^{-7}$.

4.1.2 Evaporative Cooling in the Magnetic Trap

The next step of cooling is performed by forced evaporative cooling in a magnetic time orbiting potential (TOP) trap [60]. In magnetic traps the magnetic dipole moment of the neutral atoms is used in order to create a confining potential by proper magnetic field gradients. The energy of a particle with magnetic dipole moment μ in a magnetic field $\mathbf{B}(\mathbf{r})$ is given as

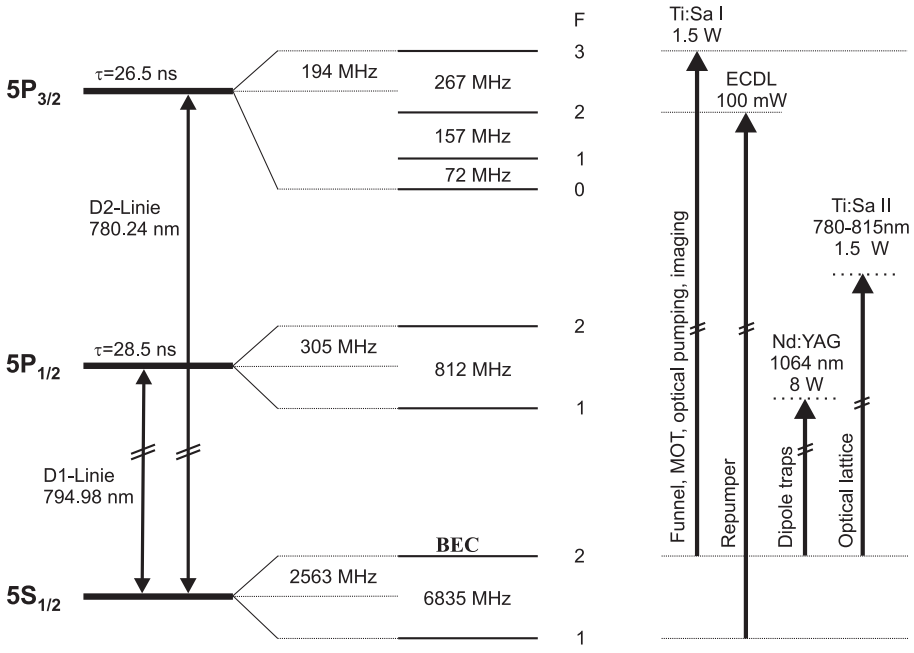

Figure 4.3: Hyperfine structure of ^{87}Rb. The right side shows the lasers used for the corresponding transitions.

$$E(\mathbf{r}) = -\mu \cdot \mathbf{B}(\mathbf{r}). \tag{4.1}$$

For an atom in the magnetic hyperfine substate m_F this becomes, introducing also the gyromagnetic factor g_F and the Bohr magneton μ_B:

$$E(\mathbf{r}) = m_F g_F \mu_B |\mathbf{B}(\mathbf{r})| \tag{4.2}$$

Atoms with $m_F g_F > 0$ are called 'low-field seeker', since they tend to move to the point of the lowest magnetic field in order to minimise their energy. They can therefore be trapped in a minimum of a magnetic field. In the case of $m_F g_F < 0$ the atoms are called 'high-field seekers'. Those, however, cannot be trapped by a magnetic field, since the Maxwell equations do not allow magnetic field maxima at places without current, e.g. in free space. This restricts the magnetically trapable hyperfine substates for ^{87}Rb in its ground state to $(F = 1, m_F = -1)$, $(F = 2, m_F = 1)$ and $(F = 2, m_F = 2)$. Since it has the largest magnetic moment, the atoms are transferred into the last of these states by means of optical pumping. The atoms therefore can be trapped more densely, as the potential experienced by the atoms is largest. This leads to a more efficient re-thermalisation of the atoms and thus to a faster cooling process as will be explained below.

The magnetic field gradient is provided by a quadrupole field produced by two coils in anti-Helmholtz configuration. This quadrupole field, however, has a zero field minimum in its centre. Experiencing no magnetic field the atoms can undergo Majorana spin flips [61], thus become high-field seekers and disappear from the trap. In order to prevent this, in TOP traps the minimum of the magnetic field is moved on a circular path by

means of a rotating bias field, producing a time averaged magnetic field with a nonzero minimum [55] and trapping frequencies on the order of $2\pi \times 100\,\mathrm{Hz}$ in our case. The speed of the moving minimum has to be fast enough so that the atoms cannot follow it (much faster than the centre of mass motion of the atoms) but slow enough such that the magnetic moment may readjust to the time varying magnetic field (i.e. with a rotation frequency much smaller than the Larmor frequency). In our experiment the rotation frequency of the moving field minimum is $\omega_{TOP} = 2\pi \times 9.8\,\mathrm{kHz}$.
The circular path of the minimum is called 'circle of death' since atoms on this circle can leave the trap via the Majorana process. This can be used for forced evaporative cooling: By narrowing the circle diameter slowly enough so that the 'hottest' atoms, i.e. those having the highest kinetic energy, are allowed to leave the trap while the remaining atoms can still re-thermalise, energy is carried out of the atomic cloud by the departing atoms and the temperature of the cloud drops. In this experiment the circle of death is reduced from originally 1.6 mm to 75 μm until finally $\approx 3 \times 10^6$ atoms with a phase space density of $\Omega \approx 5 \times 10^{-3}$ are left. The atoms are now transferred to an optical dipole trap for further cooling and condensing.

4.1.3 Optical Potentials and Traps

Traps based on optical dipole potentials have several advantages over 'standard', i.e. non-atom-chip based magnetic traps. They can be made smaller, more stable and reproducible, they are easier to control and more flexible in their spatial form. Therefore the presented experiments are performed in optical potentials. The reason why the atoms are not directly loaded into an optical trap from the MOT is that the available optical traps cannot be made large and strong enough to trap enough atoms from the MOT in order to perform the evaporative cooling procedure. There are, however, experiments where this has been realised [62, 63].
The optical potential results from the interaction between the dipolar moment $\mathbf{d}$ of the atom which is induced by the electric field of the laser $\mathbf{E}(\mathbf{r})$ and the electric field $\mathbf{E}(\mathbf{r})$ itself. This effect is known as 'ac Stark shift'. Considering an atomic two state system with Γ representing the natural transition line width and with the Rabi frequency $\Omega = \mathbf{d} \cdot \mathbf{E}(\mathbf{r})/\hbar$, the dipole potential experienced by the atom is [64, 65]

$$V(\mathbf{r}) = \frac{\hbar |\Omega(\mathbf{r})|^2}{4\delta}, \tag{4.3}$$

where we introduced $\delta = \omega_L - \omega_0$ which is the detuning of the laser frequency ω_L to the centre of the transition frequency ω_0. For the square of the Rabi frequency we find [64, 65]

$$|\Omega(\mathbf{r})|^2 = \frac{\Gamma^2 I(\mathbf{r})}{2 I_S}, \tag{4.4}$$

where we introduced the intensity of the laser beam $I(\mathbf{r})$ and the saturation intensity $I_S = \frac{\pi h c \Gamma}{3\lambda^3}$. Due to its fine structure, ^{87}Rb has two transitions, D1 at 795 nm and D2 at 780 nm with the D2 transition being twice as strong as the D1 line. Considering this and introducing the Clebsch-Gordan coefficient of 2/3 for atoms in the $m_F = 2$ substate at

linearly polarised light we get for the optical dipole potential experienced by the ^{87}Rb atoms:

$$V(\mathbf{r}) = I(\mathbf{r})\frac{\hbar\Gamma^2}{8I_S}\frac{2}{3}\left(\frac{1}{\delta_{D2}} + \frac{1}{2\delta_{D1}}\right) \tag{4.5}$$

Note that the sign of the potential depends on the sign of δ. For $\delta < 0$, i.e. a red detuning of the laser beam to the transition line the atoms are high-field seekers. For $\delta > 0$ they are low-field seekers.
A confinement for atoms can thus be created by a red-detuned focussed laser beam in the Gaussian TEM_{00} mode. Such a beam, propagating in x-direction and focussed to a minimum beam waist[1] of w_f has the following intensity distribution

$$I(x, y, z) = \frac{I_0}{1 + (x/x_R)^2}\exp\left[-2\frac{y^2 + z^x}{w_f^2(1 + (x/x_R)^2)}\right], \tag{4.6}$$

with $x_R = \frac{\pi w_f^2}{\lambda}$ being the Rayleigh length which determines the divergence of the beam waist along the propagation direction. $I_0 = \frac{2P}{\pi w_f^2}$ is determined by the laser power P which is $\approx 500\,\mathrm{mW}$ in our case. This beam is provided by a Nd:YAG laser from *Spectra Physics* (*T 40-X30-106QW*, Nd:YAG III) and transferred to the experiment by means of an optical fibre. It has a wavelength of 1064 nm and is focussed to a beam waist of $60\,\mu$m, which results in a Rayleigh length of $\approx 1.1\,\mathrm{cm}$. The waist of the beam $w(x) = w_f(1 + (x/x_R))$ can therefore be assumed to be w_f in the region of the atoms in our case since the atomic cloud is of the size of a few microns only and thus much smaller than this length.
The dipole potential given by a single, not tightly focussed laser beam therefore creates only a lateral confinement for the atoms which can be found by inserting equation (4.6) into (4.5):

$$V_{dipole}(y, z) = V_0\exp\left[-2\frac{y^2 + z^2}{w_f^2}\right], \quad V_0 = \frac{\hbar\Gamma^2 I_0}{8I_S}\frac{2}{3}\left(\frac{1}{\delta_{D2}} + \frac{1}{2\delta_{D1}}\right) \tag{4.7}$$

In our case $\Gamma = 2\pi \times 5.76\,\mathrm{MHz}$ and $I_S = 1.58\,\mathrm{mW/cm^2}$. Due to the shape of this 'tube-like' potential, it is often referred to as a 'waveguide'. Since we will only be working with small atomic clouds in the centre of the waveguide we can expand (4.7) and keep only the second order term which results in a harmonic confinement approximation of $V_{dipole}(y, z)$ with the lateral trap frequencies

$$\omega_y = \omega_z = \sqrt{\frac{4|V_{WG}|}{mw_{WG}^2}}, \tag{4.8}$$

[1] Beam 'waist' is here defined as the $1/e^2$ radius of the Gaussian cross section of the beam given as $\exp\left[-2\frac{y^2+z^2}{w_f^2}\right]$.

where we have renamed $w_f =: w_{WG}$ and $V_0 =: V_{WG}$.
In order to prevent the atoms from escaping in the x-direction, a second beam is needed which is perpendicular to the waveguide. This beam is called 'crossed dipole trap' or 'X-DT'. It also has a wavelength of 1064 nm and a power of $\approx 800\,\mathrm{mW}$ provided by the same laser as the waveguide and is also guided to the setup in an optical fibre. This beam is propagating in z-direction and has a beam waist of $w_{XDT_y} \approx 140\,\mu\mathrm{m}$ in y-direction and of $w_{XDT_x} \approx 70\,\mu\mathrm{m}$ in x-direction. The asymmetry is obtained by spreading the beam in y-direction by means of a cylindrical lens. This is done in order to be able to adjust the confinement x-direction by varying the power of the X-DT without changing the confinement in y-direction too much, which is then mainly given by the waveguide beam. However, we also have to take gravity into account, which, pointing in $-y$-direction, pulls the atoms away from the location of maximum laser intensity. This effectively reduces all trapping frequencies.
With the two superimposed beams a three-dimensional quasi harmonic confinement with the following maximum trap frequencies can be realised:

$$\omega_{x_{max}} = 2\pi \times 150\,Hz, \quad \omega_{y_{max}} = 2\pi \times 210\,Hz, \quad \omega_{z_{max}} = 2\pi \times 220\,Hz. \tag{4.9}$$

We also have to think about the loss of atoms in the dipole trap due to absorbtion of photons of the laser beams. If an atom absorbs a photon, its recoil obtained on re-emission is so large that it will instantly leave the trap. The spontaneous scattering rate

$$\Gamma_s = \frac{\Gamma^3 I_{max}}{8 I_S} \frac{2}{3} \left(\frac{1}{\delta_{D2}} + \frac{1}{2\delta_{D1}} \right) \tag{4.10}$$

depends on the laser intensity and on the detuning to the transition line. In our case $\Gamma_s \approx 0.01\,\mathrm{Hz}$. The loss of atoms during the cooling sequence, which is on the order of a few seconds is therefore small. In the time scale of the actual tunnelling experiments, which is in the millisecond range, the loss is negligible.
The atoms that have been pre-cooled evaporatively in the magnetic trap are now loaded into the optical dipole trap whose laser beam intensity is slowly being reduced in order to make the trap shallower and to let the most energetic atoms escape. At the critical temperature $T_c \approx 40\,\mathrm{nK}$ the atoms start condensing into a Bose-Einstein condensate. The evaporation cooling continues until $T \approx 15\,\mathrm{nK}$ in order to get a clean condensate with only a small fraction of atoms in the excited states. The typical density of the BEC is $10^{13}\,\mathrm{atoms/cm^3}$. The whole process of creating a Bose-Einstein condensate takes about one minute.

4.2 Creating a Double Well Potential

4.2.1 Experimental Method

In order to perform Bose-Einstein Josephson junction experiments, a double well potential is needed. Several methods exist to create such a potential. The first double well potential, which was used for interference measurements with BECs [6] was implemented using the harmonic confinement of a magnetic trap and focussing a blue detuned laser

beam into the centre of the trap which created a barrier. This realisation had a well spacing of 50 μm and was therefore too large to observe Josephson tunnelling on a realistic time scale.
A recent realisation of a purely optical double well potential by Shin *et.al.* [29] had a double well distance of 15 μm which would still lead to Josephson oscillation frequencies of only 1 Hz.
Atom chips are in principle the perfect tool for creating double well potentials with a well spacing of the required few microns. This has recently been realised by Estève *et.al.* [30]. The elongated BECs created in these atom chip traps, however, suffer from fragmentation due to spatial inhomogeneities of the magnetic field. Therefore the overlap of the two wave functions is inhomogeneous along the trap axis leading to spatially dependent tunnelling time scales. The authors of [30] do state, however, that these problems can be fixed and that Josephson oscillations will be observable with this system.
Due to the fact that optical traps can be created more flexibly and are more reproducible than magnetic traps the alternative of a purely optical double well trap was chosen in this experiment. Except for the method in [29], further possibilities of creating a purely optical double well potential are imaginable, e.g.:
Creating a thin light sheet, i.e. a laser beam focussed narrowly only in one direction and shining it into the centre of the optical harmonic dipole trap would yield the desired result. Another method consists of superposing a standing light wave with the Gaussian optical dipole potential of the X-DT beam.
Since standing light waves have already been used in former experiments of the group (see [55, 56, 57] and the PhD thesis of Thomas Anker), the second method was chosen. The resulting potential is shown in figure 4.4(a). The standing wave is created by two linearly polarised laser beams of $\lambda \approx 810\,\mathrm{nm}$ provided by Ti:Sa II (*Coherent*, 899) which are intersecting at an angle of 9° at the place of the BEC, thus creating an effective standing light wave with a periodicity of $d = 5.2(2)\,\mu$m in x-direction.
In the central region of this combined trap the Gaussian can be approximated by a parabola, yielding a potential of the form

$$V_{DW}(x) = \frac{m\omega_x^2}{2}(x - \Delta x)^2 + V_0 \cos^2\left(\frac{\pi x}{d}\right) \tag{4.11}$$

in x-direction, which represents a double well in its central region. Δx represents the shift between the two potentials. For $\Delta x = 0$ the potential is symmetric. This case is shown in figure 4.4(b), depicting the central part of 4.4(a). For $0 < |\Delta x| < d$ it becomes asymmetric. The effective double well distance becomes 4.4 μ.
Δx can be varied by two different methods. On the one hand the x-position of the X-DT beam can be moved. This can simply be done by tilting the fibre collimator providing the laser beam with the help of piezo elements. On the other hand, by shifting the relative phase $\Delta\varphi$ of the two beams creating the standing wave, the interference pattern can be moved along the x-axis. The possibility of creating an asymmetry by shifting the harmonic confinement and the standing wave with respect to each other, is used for creating an initial population asymmetry in the double well as described in section 5.2.2.
The actual setup of the optical components can be seen in figure 4.5 and will be further described in the following.

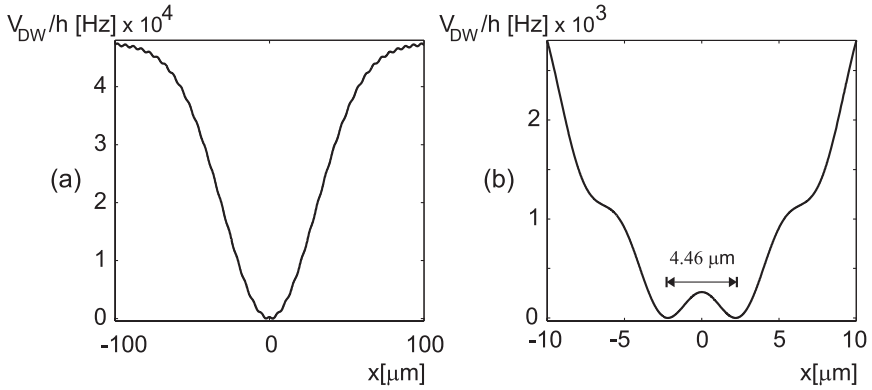

Figure 4.4: (a) Dipole potential resulting from the superposition of the X-DT beam and the standing light wave. (b) Magnification of the central region of (a).

4.2.2 Analysis and Improvement of Stability

The fact that the double well symmetry depends on the relative position of the X-DT beam and the standing wave causes severe stability problems. As it was mentioned above, the initial distribution $z(0)$ of the atoms is created by means of an asymmetric double well. Due to the small dimensions of the trap, already a shift of $\Delta x \approx 350\,\mathrm{nm}$ leads to an initial population difference large enough to switch from $z(0) = 0$ to the self-trapping regime. This is especially critical since the optical path length of the laser beams creating the trap are on the order of tens of centimetres. The optical elements in the path of the laser beams, e.g. the fibre outcouplers, mirrors, etc., have to be mounted extremely stable. Additionally, $\Delta\varphi$ has to be controlled actively as described further below.

Stability of Waveguide and X-DT

In the early stages of the experiment standard posts and post holders were found to be too instable for mounting the optical elements. Long posts leading to poor mechanical stability were used because the glass cell, where the BEC is created is located 21.7 cm above the optical table. Therefore, the fibre collimator of the waveguide was set up on a single, massive aluminium block. Furthermore a secondary optical table of a height of 19 cm was built up and was fixed to the main table using six massive aluminium table-legs. The optical elements of the X-DT are now mounted robustly on this new table and the optical fibre outcoupler could be placed close to the vacuum chamber (20 cm). This setup is shown in figure 4.5 in top view.
The only optical elements left in the path of the X-DT beam consist of a focussing lens directly glued to the holder of the fibre collimator, the cylindrical lens needed to expand the X-DT beam in y-direction and an anti-reflection coated glass plate used to guide a part of the X-DT beam onto a quadrant photodiode in order to monitor the beam movements.
The x-position stability of the X-DT beam at the place of the atoms was analysed before and after the modification. Since the location of the atoms along the x-axis is given by the X-DT position, this could be done by taking approximately 30 pictures of a BEC in

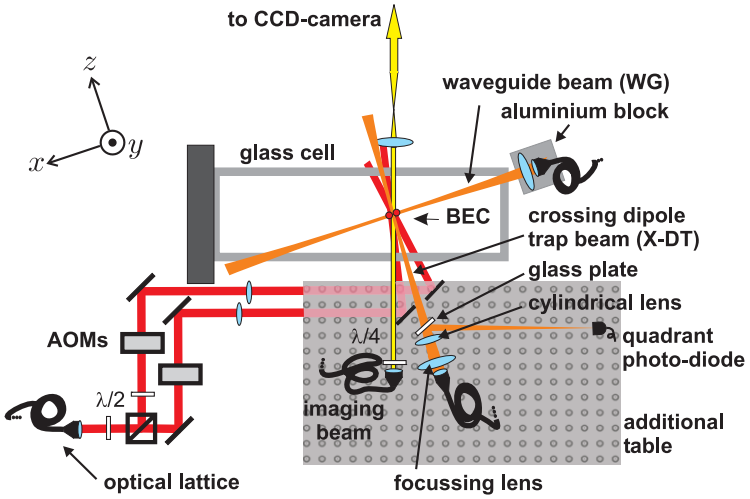

Figure 4.5: Top view of the beam configuration of the optical traps. The BEC plane is located 21.7 cm above the optical table, the additional optical table has a height of 19 cm. Therefore all optical parts of the X-DT beam could be mounted with high stability and close to the glass cell. The components of the standing wave beams are mounted on the main optical table and the beams are directed upwards by the last mirror. Note that the glass plate and the slit aperture used for monitoring the phase of the standing wave beams are not shown.

the harmonic confinement and estimating the x-positions of the atomic clouds by fitting them with a Gaussian. It is found that the position stability of the X-DT could be improved from a standard deviation of 800 nm to below 100 nm from picture to picture. The position fit error is also on the order of 100 nm, therefore the stability can assumed to be even better.
As mentioned, the position is also measured by a quadrant photodiode (QPD), which consists of a circular light sensitive area that is divided into four equal quadrants A, B, C, D as shown in figure 4.6. The deviation δx and δy from the centre position of a homoge-

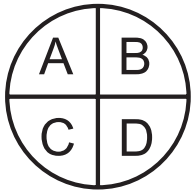

Figure 4.6: A quadrant photo diode is a circular photo diode divided into four equal quadrants A, B, C, D.

neous beam shining onto the four quadrants of the diode can be measured by comparing the fractions of beam power falling on the left half of the QPD with that falling on the right half of the QPD and that on the upper half with that on the lower half, respectively:

$$\delta x \propto \frac{P_A + P_C}{P_{tot}} - \frac{P_B + P_D}{P_{tot}}$$
$$\delta y \propto \frac{P_A + P_B}{P_{tot}} - \frac{P_C + P_D}{P_{tot}}$$

Here, $P_{A,B,C,D}$ represents the power measured on quadrant A, B, C, D and $P_{tot} = P_A + P_B + P_C + P_D$. The photodiode is very accurate and can resolve beam shifts below 70 nm. Due to the longer optical path from fibre outcoupler to QPD than to the BEC in the vacuum chamber, a tilt of the outcoupler that corresponds to a beam shift of $\delta_x = 70\,\text{nm}$ on the photodiode corresponds to a deviation of $\approx 30\,\text{nm}$ in the region of the BEC. X-DT beam displacements resulting from an instable outcoupler can therefore in principle be measured extremely well.
Comparing the beam position measured by the QPD and the position estimated by fitting the position of the atomic cloud, however, does not reveal any obvious correlation in the fluctuations of the beam position as shown in figure 4.7. The abscissa denotes the x-position of the X-DT determined by the position fit of the atomic cloud while the ordinate shows the position of the beam as simultaneously estimated by the quadrant

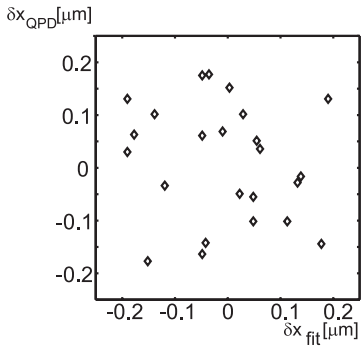

Figure 4.7: The abscissa shows the position of the X-DT beam as estimated by the position fit of the atomic cloud (δx_{fit}). The ordinate shows the position of the beam as determined by the quadrant photo diode (δx_{QPD}). Each diamond corresponds to one experiment where δx_{fit} and δx_{QPD} have been measured independently and simultaneously. No obvious correlation of the data can be seen. The distance is given relatively to the middle of the total position range.

photo diode. It can be seen that the signal on the QPD shows a signal fluctuation from picture to picture, i.e. on the minute scale, which is on the same order of magnitude as the standard deviation of the position fit.
The fact that both signals are uncorrelated gives rise to the assumption that the fluctuation of the fitted position is not so much due to an instability of the X-DT outcoupler which was assumed to be the most sensitive part in the beginning. It is rather determined by fit errors and maybe a spatial instability of the vacuum glass cell. The vacuum chamber is fixed roughly 70 cm away from the glass cell, therefore vibrations of the glass cell are thinkable and since the X-DT crosses the glass cell under an angle those would lead to a beam deviation of the described magnitude. The deviation of the signal of the QPD might be due to variations in the intensity distribution of the beam, which lead to changes of the effective position measured by the QPD. Disturbances in the air along the beam path can result in such an effect. Also instabilities of the glass plate reflecting a part of the beam to the QPD or of the QPD mount are possible reasons. Although the fluctuations could be reduced by shielding the optical path with small tubes (red tubes in figure 4.8) the total beam path could not be shielded due to spatial constraints.
Due to this uncorrelation and due to the additional effect that the position measured by the photodiode shows long-term drifts on the order of hours which are also not correlated to the fit position, the X-DT beam can not be further actively stabilised using the QPD

as reference signal as originally intended. The analysis of the beam position with the QPD revealed, however, that the stability of the X-DT position suffers significantly if the beam is not coupled into the fibre with the correct polarisation direction which could thus be revised. Furthermore the QPD is still used as a reference indicating sudden jumps of the X-DT beam and for estimating the time scale of X-DT shifting (see section 5.2.2).

Stabilisation of $\Delta\varphi$

In order to keep variations of the shift Δx between harmonic confinement and lattice potential small it is also crucial to keep the relative phase $\Delta\varphi$ of the two interfering beams creating the standing wave constant. In order to ensure this, it was absolutely necessary to actively stabilise $\Delta\varphi$ with the setup used at the time. This setup is depicted in figure 4.5. The optical path lengths are on the order of one metre, including several optical devices as shown in the figure.
In order to stabilise $\Delta\varphi$, a fraction of each of the two beams is led onto a slit aperture of $5\,\mu$m width as shown in figure 4.8, using two anti-reflection coated glass plates. The two

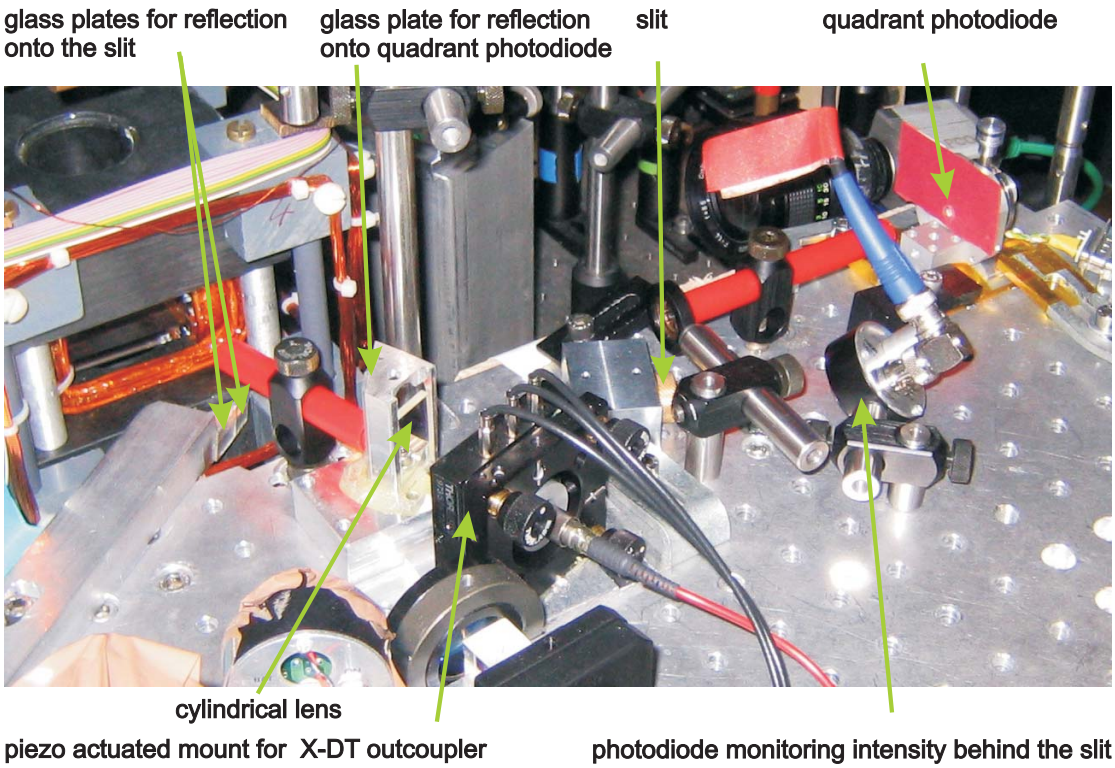

Figure 4.8: Picture of the actual setup on the additional optical table. The two glass plates, reflecting parts of the standing wave beams onto the slit aperture can be seen. The slit aperture is mounted in the labelled brass holder. The lens focussing the light behind the slit onto the monitoring photodiode cannot be seen. Note the red tubes installed to minimise beam aberrations due to air flow.

glass plates are mounted at an angle so that the two beams interfere on the slit aperture at an angle of 4°. The slit of the aperture is aligned to be parallel to the interference fringes. A lens projects the light going through the slit into a photodiode. When $\Delta\varphi$ is shifted, the fringes move over the slit, producing a bright-dark-pattern on the photodiode

over time. This signal can be used as a reference signal for $\Delta\varphi$ which can be adjusted by means of an acousto optic modulator (AOM) in each beam path of the standing wave (please refer to section 6.3.4 for the working principles of an AOM). Shifting the phase of the RF signal driving the AOM yields in a phase shift of the beams of the standing wave. Using four RF phase shifters connected in series (*Minicircuits JSPHS120*) the phase can be shifted within a range of $\pm 2\pi$. Using a proportional-integrator (PI) loop for controlling the phase, the optical lattice can be stabilised better than 100 nm with this method. It is, however, only possible for constant lattice beam intensities. During the experimental sequence the lattice beams have to be ramped up within 1 s. Therefore $\Delta\varphi$ is actively stabilised at low lattice beam intensities before the ramping and then held constant during the ramping time and the following evolution time of the BEC in the double well trap by means of a sample and hold circuit.

Even more Stability of $\Delta\varphi$

The setup described above was used for phase stabilisation in the Josephson oscillation experiments. However, a new and improved standing wave setup has been constructed afterwards and shall be described at this point for consistency. Although the former setup could provide sufficient short term stability the depth of the periodic potential changed significantly on the time scale of a few days. The reason for this were uncontrollable long term drifts of the position of the two laser beams, resulting in a varying overlap. Due to this the optical lattice had to be calibrated and readjusted after a few days' time which restricted the time available for long experimental runs.
Therefore a much more compact and less delicate setup has been designed and constructed. A sketch of the new setup is shown in figure 4.9(a), figure 4.9(b) shows a photo. The standing wave setup is now reduced to very few optical devices mounted on

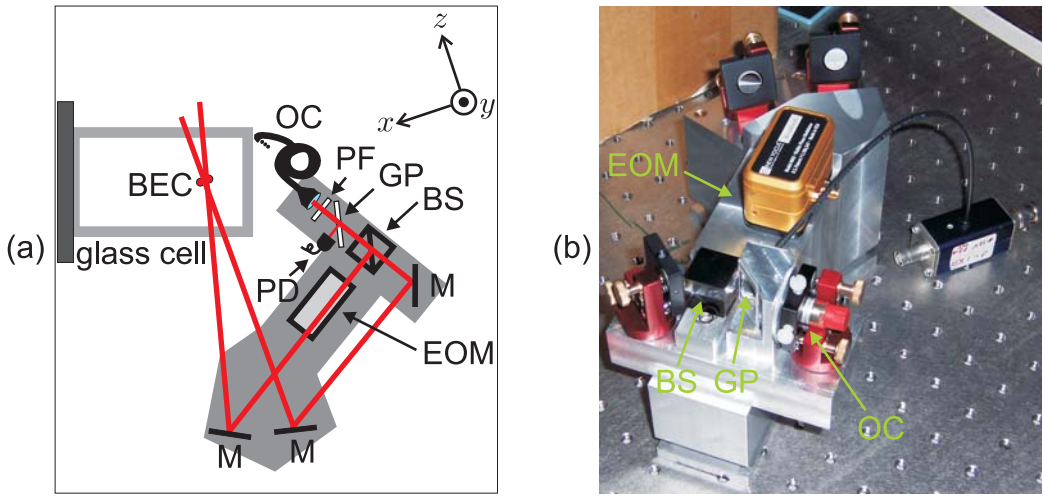

Figure 4.9: (a) shows a sketch of the new setup for the standing wave beams. All optical components are compactly mounted on a large aluminium block. Note that the lengths of the beam paths are not drawn to scale. (b) shows a photo of the setup. Note that the photo is turned for about 180° around the y-axis with respect to the sketch in (a).

a massive aluminium block and has a short optical path of 30 cm. The laser beam enters from the outcoupler of the optical fibre (OC). It then passes a rotatable polarising filter

(PF) and an anti-reflection coated glass plate (GP) which deflects a small fraction of the beam to a photodiode (PD) as a reference signal for the intensity stabilisation (see below). These three components are fixed in a compact and stable way on a specially manufactured mount. Afterwards the beam is equally divided by a non-polarising beam splitter (BS) which supersedes the use of an additional wave plate. One of the resulting beams now passes an electro optic modulator (EOM) which can shift the phase of the beam by up to 2π. The beams are then guided into the chamber by mirrors (M). The lattice distance of the resulting standing wave is $4.46\,\mu$m with this setup.
A further improvement is the use of a lock-in amplifier in order to control $\Delta\varphi$. The phase difference can now be held stable also when ramping the intensities of the beams. Additionally, a more compact, lens-free setup for the reference slit and photodiode has been designed. For well aligned standing wave beams, the depth of the lattice potential now remains stable within 10% for up to two weeks.

Stabilisation of Intensity

All laser beams also have to be stabilised in intensity. This is being performed by collecting a part of the light coming out of the fibres which carry the light to the experiment and guiding it to a reference photodiode. In the case of the X-DT, the waveguide and the lattice beams, the reflection of the beams on the glass cell are taken as reference. The intensity can be varied by an AOM which is placed in front of the fibre. The intensity can then be stabilised using a proportional-integrator loop [66].

4.3 Imaging System

In order to observe the tunnelling dynamics, pictures of the BEC have to be taken. Thus the features of the imaging system will now be discussed. Note that within this section, we perform a change of the coordinate set. Due to the fact that we are primarily interested in the image, we will denote the axes of the image plane with the 'usual' variables x, y and the imaging direction with z. The denotations of the axes of the object coordinate system, including laser propagation directions, which have hitherto had these labels are now changed to Greek letters $x \to \xi$, $y \to \eta$, $z \to \zeta$. For clarification, please refer to figure 4.12.

4.3.1 Imaging Setup

The density distribution of the atomic cloud is measured by standard absorption imaging. This technique will only be shortly explained. It is discussed in detail in many other works e.g. in [55, 57].
The atomic cloud is illuminated by a collimated laser beam provided by Ti:Sa I with a diameter of 1.8 mm, propagating in z-direction. The laser beam is σ^+ polarised and resonant to the D2 transition ($F = 2 \to F' = 3, \lambda = 780.2\,\mathrm{nm}$). The atoms are hence fluorescing and scattering the light. Therefore only a small (in our case negligible) fraction of the exciting photons is being re-emitted into the z-direction and thus one obtains a net absorption depending on the atom density $n(\xi, \eta, \zeta)$. This 'shadow image' is then projected onto the chip of a CCD-Camera (*Theta-System SiS s285M*) by means of a microscope objective (*Zeiss Planapochromat S*, focal length $f = 10\,\mathrm{cm}$) with a tenfold magnification.
Using resonant light, the atomic cloud is heated up due to the recoil energy of the fluorescing atoms. The BEC is thus instantly destroyed. In order to measure BEC dynamics it is therefore necessary to take many pictures at different evolution times of the system.
The intensity distribution $I(x, y)$ of the 'shadow image' contains the information of the spatial atomic density distribution $n(\xi, \eta, \zeta)$ integrated along the z-axis. We define this projection as

$$n_A(x, y) := \int n(x, y, z)\, dz = N_A(x, y)/A. \tag{4.12}$$

Here, N_A is the number of atoms in each column parallel to z with base area A, which in our system is reasonably chosen as A_{pixel}/M^2, with $A_{pixel} = 6.45 \times 6.45\,\mu\mathrm{m}^2$ the area of a pixel of the CCD and $M \approx 10$ the magnification of the imaging system. In order to establish the connection between $n_A(x, y)$ and $I(x, y)$, we consider the variation of the imaging light propagating through the atomic cloud of density $n(x, y, z)$:

$$\begin{aligned} dI(x, y, z) &= -I(x, y, z)\, n(x, y, z)\, \sigma(I(x, y, z))\, dz \\ \Leftrightarrow \frac{dI(x, y, z)}{I(x, y, z)} &= -n(x, y, z)\, \sigma(I(x, y, z))\, dz \end{aligned} \tag{4.13}$$

Here,

$$\sigma(I(x,y,z)) = \frac{\Gamma h\nu}{2I_S} \frac{1}{1 + \frac{I(x,y,z)}{I_S} + \left(\frac{2\Delta}{\Gamma}\right)^2} \tag{4.14}$$

is the scattering cross section of the atoms, Γ is the width of the D2 transition line, Δ is the detuning to the resonance frequency of the D2 transition and I_S is the saturation intensity for the atoms. In our case $\Delta = 0$ since resonant light is used for imaging. Furthermore, we can apply an approximation for the high intensity limit [55]:

$$s(x,y,z) := \frac{I(x,y,z)}{I_S} \gg 1, \tag{4.15}$$

which simplifies equation (4.14) to

$$\sigma(I(x,y,z)) = \frac{\Gamma h\nu}{2I(x,y,z)}. \tag{4.16}$$

Inserting (4.16) into (4.13), the equation can now easily be integrated, yielding the desired relation:

$$I(x,y) = I_0 \left(1 - \frac{\Gamma h\nu}{2I_S s_0} n_A\right), \tag{4.17}$$

where $s_0 = s(x,y,0)$.
The actual imaging process is composed of three images taken successively. The primary image with intensity distribution $I(x,y)$ is the 'shadow image', the secondary image is a reference image without the atomic cloud and has therefore the intensity distribution $I_0(x,y)$ of the unaltered incoming beam and the third image with intensity distribution $I_b(x,y)$ is a background image without imaging light. We can therefore define

$$T(x,y) := \frac{I(x,y) - I_b(x,y)}{I_0(x,y) - I_b(x,y)} = 1 - \frac{\Gamma h\nu}{2I_S s_0} n_A. \tag{4.18}$$

Therefore we get $n_A(x,y)$ and $N_A(x,y)$ as

$$n_A = \frac{1}{\sigma}(1 - T(x,y)), \tag{4.19}$$

$$N_A(x,y) = \frac{A}{\sigma M^2}(1 - T(x,y)). \tag{4.20}$$

Here, $\sigma = \frac{\Gamma h\nu}{2s_0 I_S}$. Neglecting effects such as aberration and diffraction, we therefore get a tenfold magnification of the atomic distribution, integrated along z.
Note that the high intensity approximation leads to an overestimation of the atom number of about 10% [55].

4.3.2 Diffraction Effects

The discussion of image acquisition in the previous section is based on perfect geometric imaging and neglects resolution limiting factors such as lens errors and diffraction effects. Even if we assume a perfect lens, blurring and broadening of the image due to diffraction at the lens aperture is of great relevance in our case, since our objects' sizes are on the order of just a few wavelengths of the imaging light.
Several analysis methods such as estimation of the atom number N and of the relative atom distribution z in the Josephson-oscillation measurements depend on fitting the shape of the condensates. It is therefore of interest to study the effect of the diffraction induced change of the shape of the image.

Theory of Imaging

We will now derive the object-image relation of our imaging system and compare the results with the experimentally obtained images. This follows the derivation in [67] but is adapted to our case.
The electric field $\mathbf{E}(\mathbf{r}, t)$ of an electromagnetic wave propagating through a medium obeys the wave equation

$$\nabla^2 \mathbf{E}(\mathbf{r}, t) - \frac{n^2}{c^2} \frac{\partial^2 \mathbf{E}(\mathbf{r}, t)}{\partial t^2} = 0, \tag{4.21}$$

where n is the refractive index of the medium and c denotes the speed of light. The magnetic field $\mathbf{H}(\mathbf{r}, t)$ obeys the same differential equation. This equation is also valid for every component of $\mathbf{E}(\mathbf{r}, t)$, for example the x-component:

$$\nabla^2 E_x(\mathbf{r}, t) - \frac{n^2}{c^2} \frac{\partial^2 E_x(\mathbf{r}, t)}{\partial t^2} = 0, \tag{4.22}$$

Therefore one can summarise the behaviour of the vectorial electromagnetic wave by just considering a representative component and thus by a single scalar wave equation. However, this is only possible if the medium is optically homogeneous, i.e. $n = const.$ otherwise there will be terms occurring in (4.21) which are coupling the different components of $\mathbf{E}(\mathbf{r}, t)$ [67]. With this approximation, and taking into account the linearity of the wave propagation phenomenon, we can now express the projected image by a scalar function which is a sum over all object points, where each point is broadened by some imaging system specific function, the so called 'point spread function' or 'PSF':

$$U(x, y) = \iint_{-\infty}^{\infty} h(x, y; \xi, \eta) U_0(\xi, \eta)\, d\xi\, d\eta \tag{4.23}$$

Here, $U_0(\xi, \eta)$ is the complex field directly behind the object, i.e. it represents the object distribution. $U(x, y)$ is the field recorded in the image plane and $h(x, y; \xi, \eta)$ is the PSF and will in general be dependent on both the origin of the wave and the point where it is detected.
Figure 4.12 shows an overview of the imaging setup and the coordinate systems referred to in this section. Note that we will neglect the angle of 12.3° between ζ and z for a while and assume object plane Ω to be coplanar to the other planes. We will further

assume a thin lens, i.e. planes Λ and Λ' both to be located at distance z_1 from object plane Ω.
In order to determine the exact form of $h(x, y; \xi, \eta)$, we will first consider the normalised field $U_\delta(u, v; \xi, \eta)$ which a point source in object plane Ω generates at the lens, i.e. at the plane Λ:

$$U_\delta(u, v; \xi, \eta) = \frac{\exp\left(ik\sqrt{(u-\xi)^2 + (v-\eta)^2 + z_1^2}\right)}{\sqrt{(u-\xi)^2 + (v-\eta)^2 + z_1^2)}} \tag{4.24}$$

Assuming $z_1 \gg (u-\xi), (v-\eta)$ we can now transform the square root into

$$\sqrt{(u-\xi)^2 + (v-\eta)^2 + z_1^2} = z_1\sqrt{((u-\xi)/z_1)^2 + ((v-\eta)/z_1)^2 + 1} \tag{4.25}$$

and expand it to its series, which is given by $\sqrt{1+b} = 1 + \frac{1}{2}b - \frac{1}{8}b^2 + ...$ in the general case. Here, $b = ((u-\xi)/z_1)^2 + ((v-\eta)/z_1)^2$. If we only keep the first term of the series in the case of the square root in the denominator of (4.24) and the first two terms of the series in the exponential function in the numerator, we get

$$U_\delta(u, v) = \frac{1}{z_1}\exp\left[\frac{ik}{z_1}\left(z_1^2 + \frac{(u-\xi)^2}{2} + \frac{(v-\eta)^2}{2}.\right)\right] \tag{4.26}$$

This approximation is called 'Fresnel approximation'. The reason for keeping the first two terms of the series in the exponential function instead of just the first term as in the case of the denominator is simply the much greater influence of an approximation error in the exponent.
During propagation through the lens of focal length f, the field gets an additional phase factor $\exp\left[-i\frac{k}{2f}(u^2+v^2)\right]$ [67]. If $P(u, v)$ describes the aperture function of the lens, that is $P(u, v) = 1$ inside the lens area of radius 2.4 cm and $P(u, v) = 0$ otherwise, we find the field from our point source $\delta(\xi, \eta)$ to be

$$U'_\delta(u, v) = U_\delta(u, v)P(u, v)\exp\left[-i\frac{k}{2f}(u^2+v^2)\right] \tag{4.27}$$

directly behind the lens, i.e. in plane Λ'. In order to finally get $h(x, y; \xi, \eta)$, the field of a single point source, at the image plane Π, we again use the Fresnel diffraction approximation for the propagation over the distance z_2. Since all points in the plane Λ' contribute to the image in Π, we integrate over Λ' and thus get

$$h(x, y; \xi, \eta) = \iint_{-\infty}^{\infty} U'_\delta(u, v)\frac{1}{z_2}\exp\left[\frac{ik}{z_2}\left(z_2^2 + \frac{(x-u)^2}{2} + \frac{(y-v)^2}{2}\right)\right]du\,dv. \tag{4.28}$$

Using (4.27) and (4.26), we get a lengthy result pleading for some simplifications:

$$
\begin{aligned}
h(x,y;\xi,\eta) &= \frac{1}{z_1 z_2}\exp[ik(z_1+z_2)]\exp\left[\frac{ik}{2z_1}(\xi^2+\eta^2)\right]\exp\left[\frac{ik}{2z_2}(x^2+y^2)\right] \\
&\times \iint_{-\infty}^{\infty} P(u,v)\exp\left[\frac{ik}{2}(u^2+v^2)\left(\frac{1}{z_1}+\frac{1}{z_2}-\frac{1}{f}\right)\right] \\
&\times \exp\left[-ik\left(u\left(\frac{\xi}{z_1}+\frac{x}{z_2}\right)+v\left(\frac{\eta}{z_1}+\frac{y}{z_2}\right)\right)\right] du\,dv \qquad (4.29)
\end{aligned}
$$

The first exponential function under the integral vanishes if we choose the position of object and image plane to be consistent with the lens equation $\frac{1}{f}=\frac{1}{z_1}+\frac{1}{z_2}$ known from geometrical optics. Two other terms that can be dropped in our case are $\exp[ik(z_1+z_2)]$ and $\exp\left[\frac{ik}{2z_2}(x^2+y^2)\right]$. The first one is a constant phase factor and the second one is a phase factor depending on the coordinates of the image. Since the imaging camera can only measure an intensity distribution, both terms vanish. Furthermore one can approximate $\exp\left[\frac{ik}{2z_1}(\xi^2+\eta^2)\right]\approx 1$ since our object size is only on the order of a few microns, whereas z_1 is on the order of 10 cm. Therefore, (4.29) becomes

$$
h(x,y;\xi,\eta)=\frac{1}{z_1 z_2}\iint_{-\infty}^{\infty} P(u,v)\exp\left[-ik\left(u\left(\frac{\xi}{z_1}+\frac{x}{z_2}\right)+v\left(\frac{\eta}{z_1}+\frac{y}{z_2}\right)\right)\right] du\,dv \qquad (4.30)
$$

If we now consider the magnification $M=-z_2/z_1$, where the minus sign is introduced to compensate the effect of image inversion, we can introduce the normalised object-plane variables

$$
\tilde{\xi}=M\xi \qquad \tilde{\eta}=M\eta
$$

and plug this into (4.30):

$$
h(x-\tilde{\xi},y-\tilde{\eta})=\frac{1}{z_1 z_2}\iint_{-\infty}^{\infty} P(u,v)\exp\left[-i\frac{2\pi}{\lambda z_2}\Big(u(x-\tilde{\xi})+v(y-\tilde{\eta})\Big)\right] du\,dv \qquad (4.31)
$$

Here, we also used $k=2\pi/\lambda$. We can see from (4.31) that $h(x,y;\xi,\eta)=h(x-\tilde{\xi},y-\tilde{\eta})$. Therefore the object-image relation (4.23) of our imaging system is nothing else but a convolution of the object distribution $U_0(\frac{\tilde{\xi}}{M},\frac{\tilde{\eta}}{M})$ with the imaging function $h(x-\tilde{\xi},y-\tilde{\eta})$:

$$
U(x,y)=h(x,y)\otimes U_0(x,y)=\frac{1}{M^2}\iint_{-\infty}^{\infty} h(x-\tilde{\xi},y-\tilde{\eta})U_0(\frac{\tilde{\xi}}{M},\frac{\tilde{\eta}}{M})\,d\tilde{\xi}\,d\tilde{\eta} \qquad (4.32)
$$

Here, the factor $1/M^2$ comes from the coordinate normalisation. For the measured intensity distribution we get

$$I(x,y) = |h(x,y) \otimes U_0(x,y)|^2 \approx h^2(x,y) \otimes U_0^2(x,y) = h^2(x,y) \otimes I_0(x,y). \qquad (4.33)$$

$I_0(x,y)$ represents the intensity distribution directly at the object. The approximation in (4.33) is often used, although only valid for incoherent illumination or Gaussian-like functions $h(x,y)$ and $I_0(x,y)$ which in our case is a good approximation.
In order to get an image that resembles the object distribution as closely as possible, $h(x-\tilde{\xi}, y-\tilde{\eta})$ should therefore resemble the delta function $\delta(x-\tilde{\xi}, y-\tilde{\eta})$ as closely as possible. With a further coordinate normalisation, now in the Λ-plane

$$\tilde{u} = \frac{u}{\lambda z_2} \qquad \tilde{v} = \frac{v}{\lambda z_2} \qquad (4.34)$$

we get for $h(x-\tilde{\xi}, y-\tilde{\eta})$ in the case of a point source in or close to the origin of Ω:

$$h(x,y) \propto \iint_{-\infty}^{\infty} P(\lambda z_2 \tilde{u}, \lambda z_2 \tilde{v}) \exp\left[-i2\pi\left(\tilde{u}x + \tilde{v}y\right)\right] d\tilde{u}\, d\tilde{v} \qquad (4.35)$$

This is the Fraunhofer diffraction pattern of a circular aperture of the size of the lens. The integral of (4.35) gives the Airy function [67], which is radially symmetric and of the form

$$h(r) \propto \left[\frac{2J_1(kaMr/z_2)}{kaMr/z_2}\right], \qquad (4.36)$$

with $a = 2.4\,\text{cm}$ being the radius of the lens aperture and $r = \sqrt{x^2+y^2}$ the distance from the point where the geometric image of a given object point would be centred. The square of this function

$$h_I(r) \propto \left[\frac{2J_1(kaMr/z_2)}{kaMr/z_2}\right]^2 \qquad (4.37)$$

represents the intensity distribution of a single point source in the image plane and is depicted in figure 4.10 for our case. One finds that this picture of a point source is a disc of approximately $2\,\mu$m radius and additional dark and bright fringes around it. This represents the broadening of our image due to the imaging system.

Defining the Resolution of an Imaging System

The resolution of the imaging system is most practically defined as the minimum distance of two point sources in the object plane such that they can still be identified as two different points in the image plane. The most common criterion for this case is the Rayleigh criterion, which states that two point sources can 'barely be resolved' by a diffraction limited imaging system with a circular pupil if the maximum of the Airy pattern from the first point source falls on the first minimum of the pattern from the

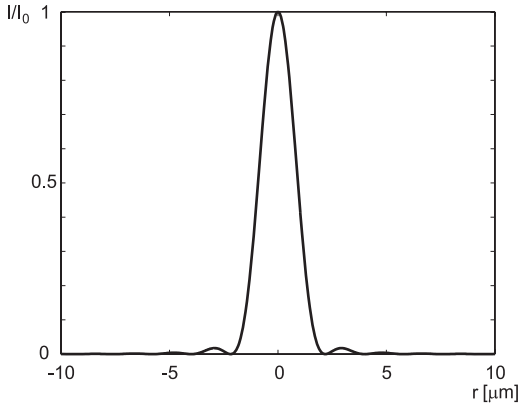

Figure 4.10: Shape of the theoretical PSF $h_I(r)$ of our imaging system, normalised to 1.

second one [67]. This situation is depicted in figure 4.11(a). The Airy function (4.36) has its first minimum at $ka|M|r/z_2 = 1.22\pi$. Therefore, the resolution as defined above is

$$r_{Rayleigh} := \frac{1.22\pi z_2}{ak|M|} = \frac{0.61\lambda z_1}{a} \tag{4.38}$$

which in our case gives $r_{Rayleigh} = 2.2\,\mu$m.
The Rayleigh criterion, however, is a pessimistic one, since at $r_{Rayleigh}$ the sum of both Airy-functions still shows a clear minimum and therefore both points can still be distinguished as can be seen in figure 4.11(a). If the two point sources are moved closer

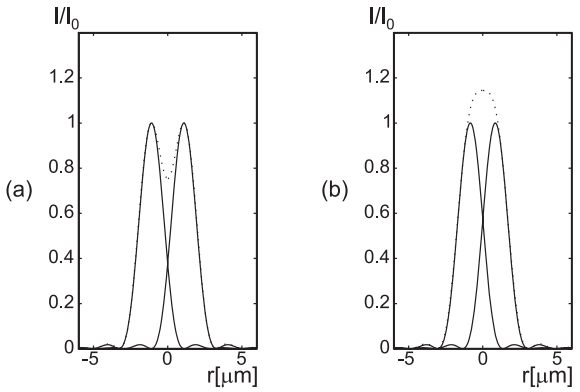

Figure 4.11: (a) The PSF of two point sources at distance $r_{Rayleigh}$, the dotted line represents the added intensity. (b) The PSF of two point sources at distance $r_{Sparrow}$. No modulation is visible in the centre. The points cannot be resolved any more.

together, this minimum will vanish at a certain distance $r_{Sparrow}$, which is depicted in figure 4.11(b). This is the distance where two points can not be resolved any more. The resolution criterion based on this definition is called the Sparrow criterion. Although perhaps less known, it represents the far more appropriate criterion for modern detection devices [68]. We get for the minimum resolution distance:

$$r_{Sparrow} := \frac{0.94\pi z_2}{ak|M|} = \frac{0.47\lambda z_1}{a}, \tag{4.39}$$

which in our case gives $r_{Sparrow} = 1.7\,\mu$m.

4.3.3 Estimation of the Optical Resolution

The theoretical resolution limit does take into account neither aberration from lens errors nor from the glass plate of the vacuum chamber. The actual resolution of the imaging is therefore expected to be worse, i.e. the broadening of the perfect geometric image will be larger with our imaging system. Due to the imperfection of the imaging system, the PSF will also not exactly be an Airy function and furthermore will not be constant. A standard method to determine the exact PSF is imaging a point-like object, for example a nano-bead or a very small point aperture and record its image. This, however, is not feasible in our case since one cannot easily insert this kind of object into the vacuum chamber. In order to get an idea of the actual PSF and hence the broadening of the image, we will therefore assume the PSF to be of the shape of the Airy function and perform a best-fit analysis in order to get its size. The procedure is as follows.

Deriving the PSF from a Best-Fit Analysis

Firstly, images of a Bose-Einstein condensate in a one-dimensional lattice potential are taken experimentally. The potential is created in the same way as described in section 4.2.1 only with much lower X-DT beam intensity, such that the confinement along the ξ-axis is much weaker and therefore more wells of the lattice are being populated. The condensate is split into several thin disks which are strung along the ξ-axis, as depicted in figure 4.12. This kind of object is well suited to study the broadening due to the imaging system: When imaged in a direction perpendicular to the ξ-axis, we observe very narrow objects for which the broadening will be significant and result in a much less modulated intensity distribution between the wells.
A typical experimentally taken picture is shown in figure 4.13(d). The pixels in figure 4.13 correspond to the pixels of the CCD. Each pixel represents $6.45/M \times 6.45/M\,\mu$m^2 of the object, where $M = 10.3$ is the magnification of the imaging system. We will call the intensity distribution of the experimentally taken picture $I_{exp}(x, y)$ and will from now on consider x,y to be discrete, denoting the xth and yth pixel of the CCD-section in the horizontal and vertical direction, respectively.
Secondly, the actual spatial density $n_{calc}(\xi, \eta, \zeta)$ of the Bose-Einstein condensate is calculated using the trap parameters of the experiment. This numerical calculation is performed using the non-polynomial Schrödinger equation method dicussed in [54].
Thirdly, the density distribution $n_{calc}(\xi, \eta, \zeta)$ is integrated along the direction of imaging z. Note that the z-axis is not parallel to the ζ-axis which leads to a broadening of the discs in the projection. This effect can be seen in figures 4.13(a) and 4.13(b), where the projections of the atomic distribution along ζ and z are shown, respectively. Figure 4.13(b) shows the perfect geometric image expected for our imaging system, which we will call $I_{geo}(x, y)$. Comparing figures 4.13(b) and 4.13(d) the broadening of the image due to diffraction becomes obvious.

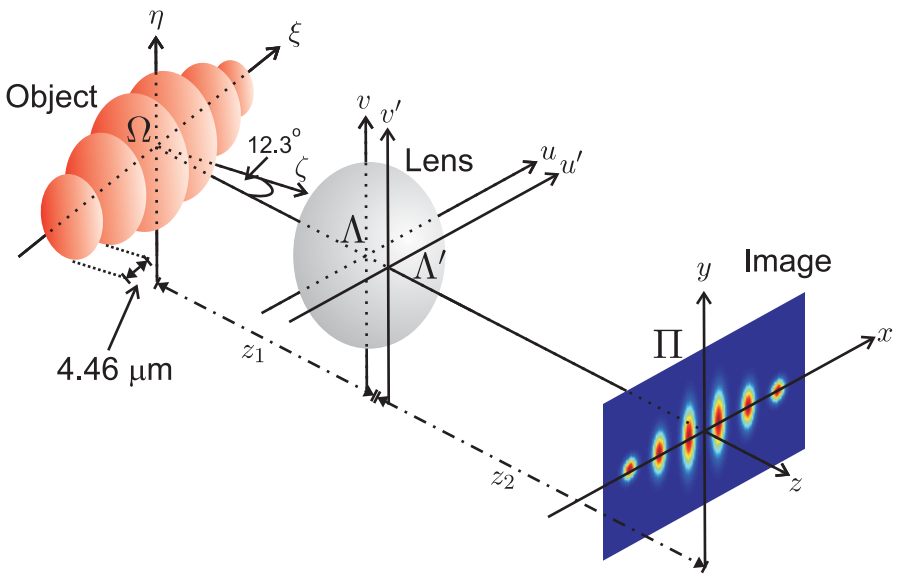

Figure 4.12: Sketch of the imaging setup. Planes Λ and Λ' are considered to be at the same place (thin lens approximation). Note that object plane Ω is not coplanar to planes Λ, Λ' and Π but tilted at an angle of 12.3° around the η-axis.

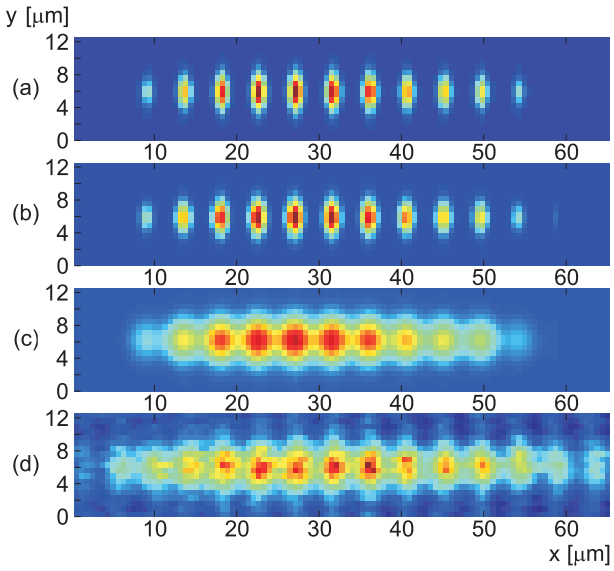

Figure 4.13: (a) shows the numerically calculated atomic density distribution $n_{calc}(\xi, \eta\, zeta)$ integrated along ζ. (b) shows $n_{calc}(\xi, \eta\, zeta)$ integrated along z. This intensity distribution corresponds to the perfect geometric image $I_{geo}(x, y)$. Note a slight broadening of the 'discs' due to the angle between ζ and z. (c) depicts $I_{geo}(x, y)$ convolved with the best-fit Airy function. (d) shows the image taken in the experiment. The pixels in the pictures correspond to a pixel on the CCD. Considering magnification, each pixel length represents to 626 nm in the object coordinate system. The pictures are colour coded. Red corresponds to a high atomic density, blue to no atoms.

If we finally convolve $h_I(x, y; a)$ and $I_{geo}(x, y)$ with varying values for the aperture a and perform a best-fit analysis of $I_{exp}(x, y)$ and $I_{theo}(x, y; a) := h_I(x, y; a) \otimes I_{geo}(x, y)$, we can estimate an a_{min} where the standard deviation of $I_{diff}(x, y; a) = I_{exp}(x, y) - I_{theo}(x, y; a)$

is smallest:

$$\begin{aligned} a &= a_{min} \Leftrightarrow \\ S(a) &:= \left(\frac{1}{x_{max} y_{max} - 1} \sum_{x=1}^{x_{max}} \sum_{y=1}^{y_{max}} \left(I_{diff}(x,y;a) - \bar{I}_{diff}(a) \right)^2 \right)^{\frac{1}{2}} \text{ is smallest} \end{aligned} \quad (4.40)$$

This best-fit analysis starts with an initial $a_{init} = 2.5\,\text{cm}$ which is larger than the actual aperture of the lens and thus leads to a broadening smaller than the theoretical one. The value of a is decreased by $da = 0.02\,\text{cm}$ in every step of iteration and $S(a)$ is calculated anew. The exact procedure for the nth iteration is as follows.

- $I_{theo}(x,y;a_n)$ is computed and $I_{theo}(x,y;a_n)$ as well as $I_{exp}(x,y)$ are normalised such that

$$\sum_{x,y} I_{theo}(x,y;a_n) = \sum_{x,y} I_{exp}(x,y) = 1$$

- Both pictures are aligned by means of a cross correlation.
- The standard deviation $S(a_n)$ of $I_{diff}(x,y;a_n)$ is computed and saved.

The iteration consists of 150 steps. Afterwards, a_{min} is determined as the minimum of $S(a)$. This procedure has been performed with four Bose-Einstein condensates in the above mentioned trap configuration. The radial (waveguide) confinement was $w_{WG} = 2\pi \times 116(5)\,\text{Hz}$, the atom numbers for each specific picture were known and considered since they have an influence on the width of the computed shape of the atomic cloud and were in the range of 14,500 to 19,500 atoms. The lattice potential was $0.46 E_{rec}$ and the lattice spacing was $4.46\,\mu\text{m}$. The value for the axial confinement was $w_{XDT} = 2\pi \times 13.3(5)\,\text{Hz}$. However, this confinement was slightly asymmetric due to a the fact that the waveguide was not parallel to the optical table but was pointing downwards at an angle of approximately 0.63°. Therefore, an additional potential $V_g = -mgx\sin(0.63°)$ has been added to the axial confinement. The effect of the asymmetry can be seen in figure 4.13(d).
For the pictures considered we yield as mean values $r_{Rayleigh} = 4.1(2)\,\mu\text{m}$ and $r_{Sparrow} = 3.2(2)\,\mu\text{m}$ which corresponds to an effective aperture radius of $a = 1.28(4)\,\text{cm}$. The errors are the standard deviation. For all pictures $S(a)$ was typically in the range of the standard deviation of the background noise of the experimentally taken pictures.
Figure 4.14 shows the effect of the broadening on the intensity modulation along the x-axis. The plots represent the intensity distribution of the mean of the central three pixel rows along the x-axis. The black dotted curve depicts the modulation expected for the perfect geometric image, i.e. of figure 4.13(b). In this case 100% modulation is obtained. The black curve and the solid red curve show the modulation for the best-fit and the experimentally taken image, respectively. Due to the broadening, the modulation is much less. All pictures were normalised to their overall intensity before the cuts were taken.
These results are to be seen as 'worst case' limit for the resolution. The method described above overestimates the actual broadening of the imaging system. This can be

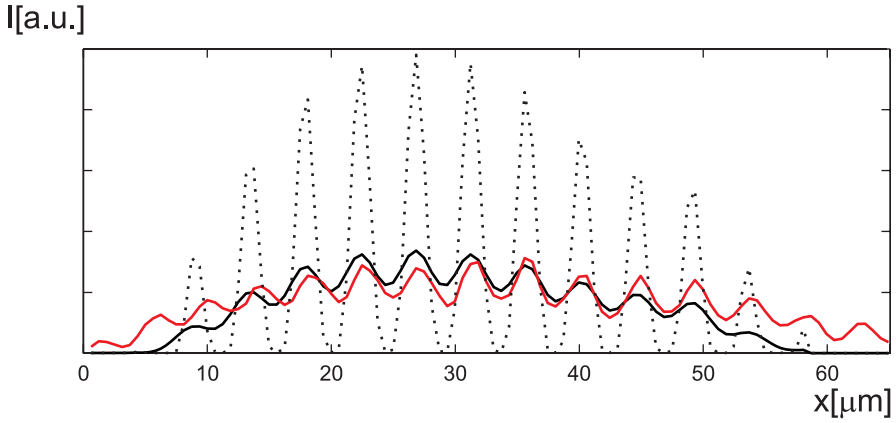

Figure 4.14: Central cut of the intensity profile along the x-axis. The solid red line shows the intensity profile of the measured image, i.e. figure 4.13(d). The black dotted curve represents the intensity modulation expected for the perfect geometric image, i.e. represents a cut through figure 4.13(b). The black solid line depicts the profile of the best fit, i.e. of figure 4.13(c).

understood taking a closer look on figures 4.13(c) and 4.13(d). It can be seen that the experimental image still shows oblate shapes for the atomic clouds as expected for projected disks, whereas the theoretical image shows 'oversmoothed', almost circular clouds. This overestimation has two reasons.
Firstly, we assume a flat object in our derivation of the PSF. The atomic clouds, however, have an extension of $\approx 5\,\mu$m in direction of imaging. The depth of field of our imaging system is roughly given by Rayleigh's depth of sharpness criterion

$$\Delta z_R = \frac{\lambda}{2\sin(\frac{a}{z_1})^2} \approx 8\,\mu\text{m}$$

and is therefore of the same magnitude as the size of our object. Those parts of the object that are not in the central focal plane therefore suffer from additional out of focus blurring.
Secondly, the resonant imaging light heats up the atomic clouds leading to an expansion particularly in imaging direction [55]. This expansion is given by

$$\Delta z_h = \frac{1}{4}\Gamma v_r \Delta t^2 \approx 800\,\text{nm},$$

where $v_r = 5.7\,\text{mm/s}$ is the recoil velocity of a ^{87}Rb atom emitting a photon on the D2-transition and $\Delta t = 4\,\mu$s is the imaging time. The atoms are thus moving out of the focal field, making our first point even more critical. The broadening in the ξ-η-plane is given by [55] as

$$\Delta\rho_h = \sqrt{\frac{\Gamma}{3}} v_r \Delta t^{3/2} \approx 160\,\text{nm}$$

and can therefore be neglected. Both reasons lead to a broadening of the object which is not considered here. Therefore, in our fitting process, the alleged broadening due to

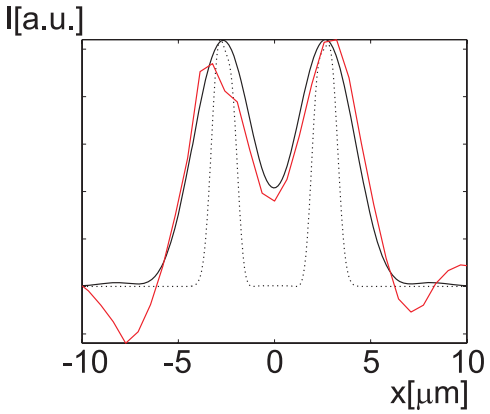

Figure 4.15: Cut in x-direction through the centre of a typical picture of a BEC in a double well potential after separation of the two BECs (see section 5.3). The black dotted curve shows the theoretical shape of the condensates. The black solid line represents the broadened theoretical shape considering our PSF. The red curve depicts the cut of the experimentally taken picture.

diffraction is overestimated. However, the first of these two effects is not easily implemented since the exact field of focus of our objective is not known.
A closer look at a picture of a BEC in a double well such as taken in the Josephson oscillation measurements does reveal, however, that the resolution estimated here is still in a realistic range. The red line in figure 4.15 shows a cut through a typical experimentally taken picture of a BEC in a double well trap, similar to those taken in order to fit the relative atomic distribution as described in section 5.3. The black dotted curve shows the shape of the atomic cloud after the Bose-Einstein condensates in the two wells were separated by ramping up the standing wave which will also be described in section 5.3. The black solid line depicts the convolution of the calculated shape with the PSF. All curves are normalised to the maximum of the experimental picture (red line). As can be seen, the modulations of the red and the black line are identical and the shapes of both curves do agree considerably well.
However, in experiments with cigar shaped BECs of 1000 atoms often lateral widths of $\sigma_{lat} = 2.9(2)\,\mu$m were estimated. σ_{lat} here represents the $1/e^2$-width of the Gaussian best fit of the lateral shape of the atomic cloud. This would not be possible with a PSF that fulfills $r_{Sparrow} = 3.2(2)\,\mu$m.

Circumventing Out-of-Focus Blurring

A second method to get an estimate of the resolution is therefore to numerically calculate the lateral shape of the cigar shaped, radially symmetric condensate and convolve it with Airy functions of different widths. Fitting the resulting function swith a Gaussian, using the same fit routine as in the experiment, and comparing them to the experimentally estimated width of $\sigma_{lat} = 2.9\,\mu$m, a best-fit Airy function can be estimated. This is done with a BEC in a lateral confinement of $2\pi \times 116\,$Hz and a shallow axial confinement of $2\pi \times 20\,$Hz. Using the NPSE method [54] we get a Gaussian shape of the lateral density distribution of the object BEC:

$$I_{obj}(r) \propto \exp\left[-2\frac{r^2}{\sigma_{obj}^2}\right] \tag{4.41}$$

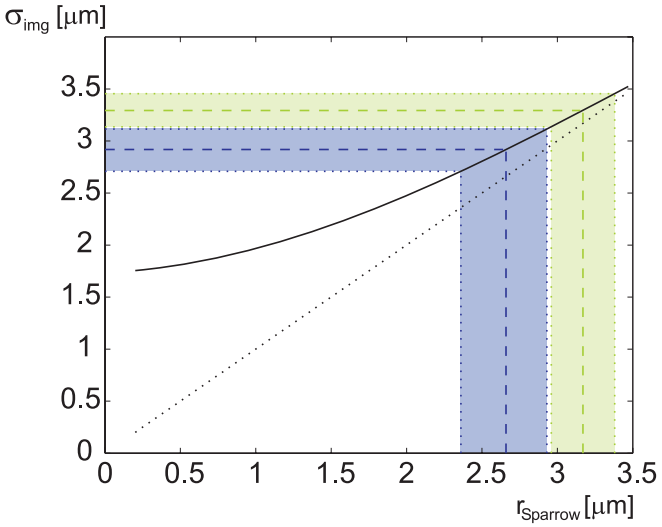

Figure 4.16: The black line shows the Gaussian best-fit of the convolution of a Gaussian with $\sigma_{obj} = 1.7\,\mu$m and the Airy point spread function according to equation (4.42). The Gaussian of $\sigma_{obj} = 1.7\,\mu$m is the numerically estimated value for a BEC in a trap with the parameters given in the text. The blue dashed line indicates the value for $r_{Sparrow}$ where $\sigma_{img} = 2.9\,\mu$m is obtained. The green dashed line shows the corresponding value for $r_{Sparrow}$ for $\sigma_{img} = 3.2\,\mu$m. The blue and green shaded regions are the respective error ranges.

Here, $\sigma_{obj} = 1.7\,\mu$m is the lateral $1/e^2$ width of the BEC and r represents the distance to the radial symmetry axis. $I_{obj}(r)$ is now convolved with

$$PSF(r_{Sparrow}) = \left[\frac{2J_1\left(0.47\frac{2\pi}{r_{Sparrow}}r\right)}{0.47\frac{2\pi}{r_{Sparrow}}r}\right]^2 \tag{4.42}$$

for varying $r_{Sparrow}$, giving

$$I_{img}(r_{Sparrow}) = PSF(r_{Sparrow}) \otimes I_{obj}. \tag{4.43}$$

The width σ_{img} of the Gaussian fit of $I_{img}(r_{Sparrow})$ is plotted in figure 4.16 (black curve). This figure shows that $\sigma_{img} = \sigma_{lat} = 2.9(2)\,\mu$m as measured in the experiment is obtained for $r_{Sparrow} = 2.7(2)\,\mu$m (blue dashed line). The blue shaded area indicates the error range which is based on the estimation of σ_{lat} from the experiments. If we assumed $r_{Sparrow} = 3.2(2)\,\mu$m, the lateral width of the image would be $3.3\,\mu$m as indicated by the horizontal green dashed line. This method does not suffer from out-of-focus blurring since the size of the object in imaging direction is much smaller than in the first method. We will therefore assume a resolution of $2.7\,\mu$m in the following.

Quantitative Influence of Image Broadening

As mentioned before, many different methods of analysing the images depend on fitting the shape of the atomic clouds. We will now discuss quantitatively the effect of the broadening due to the convolution with the PSF. We will assume Gaussian shaped objects

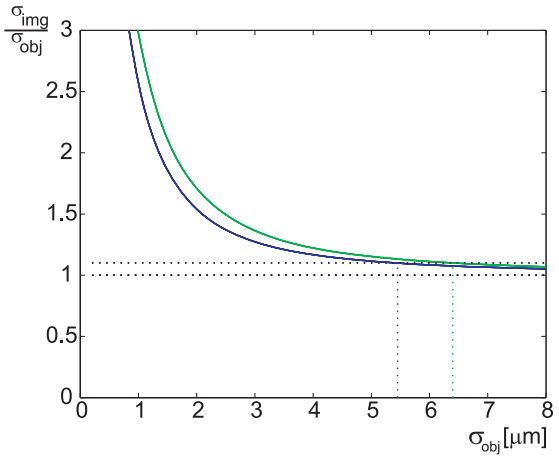

Figure 4.17: Broadening of the image due to the PSF. The solid lines show the relation of the width of the object and the image for a PSF with $r_{Sparrow} = 2.7\,\mu$m (blue) and $r_{Sparrow} = 3.2\,\mu$m (green). The dotted lines indicate a relative error $> 10\%$.

which is in good agreement with the actual shape of the atomic clouds in the trap. The object width σ_{obj} is again defined as the $1/e^2$ radius of the Gaussian representing the atomic cloud. The width of the image σ_{img} is defined as the $1/e^2$ radius of the Gaussian best-fit of the image function

$$I_{img}(r) = PSF(r) \otimes I_{obj}(r) \tag{4.44}$$

where $I_{obj}(r)$ is the object Gaussian and the PSF is the Airy function of our imaging system. Figure 4.17 shows the ratio $\sigma_{img}/\sigma_{obj}$ for different σ_{obj}. The blue line again denotes the case of $r_{Sparrow} = 2.7\,\mu$m, the green line depicts $r_{Sparrow} = 3.2\,\mu$m.
The discrepancy between the size of the actual object and its image vanishes for large object sizes since then the broadening by the PSF becomes negligible. For object sizes below $\sigma_{obj} = 5.5\,\mu$m for $r_{Sparrow} = 2.7\,\mu$m and $\sigma_{obj} = 6.5\,\mu$m for $r_{Sparrow} = 3.2\,\mu$m, however, the broadening becomes significant, i.e. the relative error of σ_{obj} and σ_{img} is larger than 10%, which is depicted by the dotted lines in figure 4.17.
This broadening effect has to be kept in mind when performing experiments with such small atomic clouds. The measured shape of the thin BECs in the Josephson oscillation experiments for example does not represent the actual shape of the BEC but is dominated by the PSF.

Chapter 5

Experimental Results

5.1 Considerations on Trap Parameters

The best parameter range for Josephson tunnelling experiments with ^{87}Rb atoms is the result of a tradeoff between different effects. First of all, both regimes, tunnelling oscillations and self-trapping have to be accessible. In order to obtain tunnelling time scales which are still observable, i.e. tens of milliseconds, the barrier between the two Bose-Einstein condensates has to be low and the two wells close to each other. A low barrier on the other hand calls for a small atom number since otherwise, due to the repulsive on-site interaction, the chemical potential would be too high above the barrier and the atoms would not tunnel any more but go over the barrier. Small atom numbers, however, are hard to detect using absorption imaging, especially concerning the phase measurement (see section 5.4) where the BECs are expanding in time of flight measurements, reducing their density even further. The alternative of making the barrier higher but thinner is limited by our imaging resolution of 2.7 μm. Furthermore the trap parameters should be sufficiently uncritical so that deviations due to experimental uncertainties and instabilities do not have too much influence. A detailed feasibility study based on numerical simulations which determines the best parameter range is outlined in [52].
The following trap parameters for the Josephson tunnelling and self trapping experiments were used: $\omega_x = 2\pi \times 78(1)$ Hz, $\omega_y = 2\pi \times 66(1)$ Hz and $\omega_z = 2\pi \times 90(1)$ Hz for the harmonic confinement. The effective spacing of the double well trap was 4.4(2) μm based on a periodic lattice with a spacing of 5.2(2) μm. The barrier height was $2\pi \times 263(20)$ Hz. The atom number was 1150 ± 150 atoms.

5.2 Initiating the Tunnelling Dynamics

It was already mentioned in section 3.2 that there are in principle two methods to initiate the Josephson tunnelling dynamics, either by creating an initial phase difference or by an initial population imbalance. Both methods will be described here.

5.2.1 Phase Induced Josephson Oscillations

The most direct analogy to the DC Josephson tunnelling case in superconductors would be to initiate the tunnelling dynamics of the BEC Josephson junction by an initial phase

difference. This can in principle be created by the so called 'phase imprinting', which is a method to locally manipulate the phase of the complex wave function $\Psi(\mathbf{r}, t)$ of the Bose-Einstein condensate.
This is being done by shining a pulse of off-resonant light on a part of the condensate for a short time T and therefore creating an additional potential for the atoms. If we assume that this additional potential $V_{PI}(\mathbf{r}, t)$ which will now appear in the Gross-Pitaevskii equation (3.9) is much larger than the other terms appearing in (3.9), we can describe the phase factor of the condensate wave function $\Psi(\mathbf{r}, t)$ after the pulse as [33]:

$$\Psi(\mathbf{r}, T) = exp[-iTV_{PI}(\mathbf{r})/\hbar]\Psi(\mathbf{r}, 0) \tag{5.1}$$

T must be smaller than the timescale of the BEC dynamics. In this case it means that $T \leq 1\,\text{ms}$. If only one of the two double wells is illuminated by the light, we will therefore get a phase difference[1] $\phi = \phi_L - \phi_R$ between both wells.
In order to imprint a clean and constant additional phase on only one of the two coupled BECs, a light pattern is needed which has a steep intensity gradient in the region of the central barrier and is constant otherwise. It can be created by a tightly focussed Gaussian beam, which is quickly (i.e. within T) scanned over one of the weakly linked condensates, resulting in a time averaged optical potential. This process is shown in figure 5.1, which depicts results of a numerical simulation of the phase induced Josephson oscillation method.

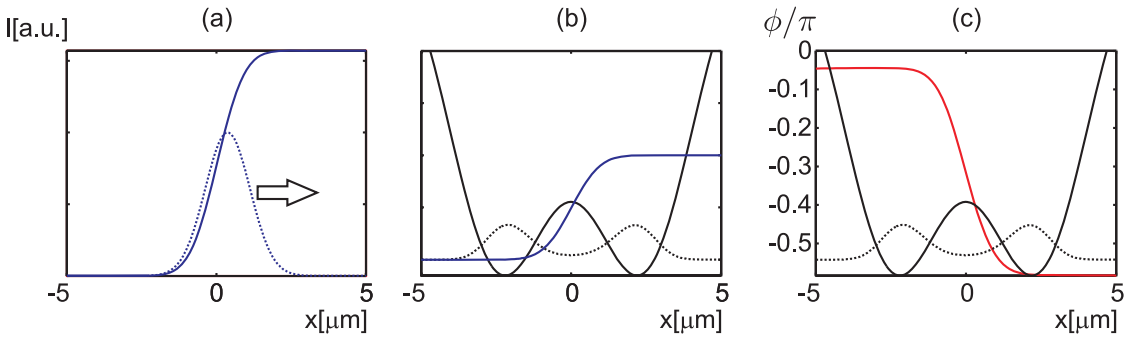

Figure 5.1: (a): The Gaussian intensity profile of the blue detuned laser beam focus is depicted by the blue dotted line. If the beam is moved to the right, the time integrated intensity distribution shown by the blue solid line is obtained. (b): Effective, time integrated phase imprinting potential (blue line) for the BEC (black dotted curve) in the double well potential (black solid line). Note, that the potential of the phase imprinting beam and the double well potential are not drawn to scale (see text). (c): The imprinted phase is shown by the red line.

Figure 5.1(a) shows the Gaussian beam of diameter $d = 3\,\mu$m (dotted blue line) which is moved to the right, creating a time integrated light pattern (solid blue line) with a steep edge but otherwise constant intensity. The potential created by this blue detuned light pattern is depicted in figure 5.1(b) by the blue solid line. The BEC is shown here with the black dotted curve and the constant double well potential with the black solid line. Note, that the potentials are not drawn to scale. The potential created by the focussed

[1]Note that we now define $\phi = \phi_L - \phi_R$ corresponding to the SJJ case and different than in the two mode model of the BJJ.

laser beam is of a factor 35 larger than the height of the central barrier. The beam is scanned over the condensate within $50\,\mu$s and then turned off. The resulting imprinted phase is shown in 5.1(c) by the red line. The intensity and detuning of the blue detuned laser beam are chosen such that the resulting phase difference is $\phi = \frac{\pi}{2}$.
Figure 5.2 shows the time evolution of the so prepared Bose-Einstein Josephson junction.

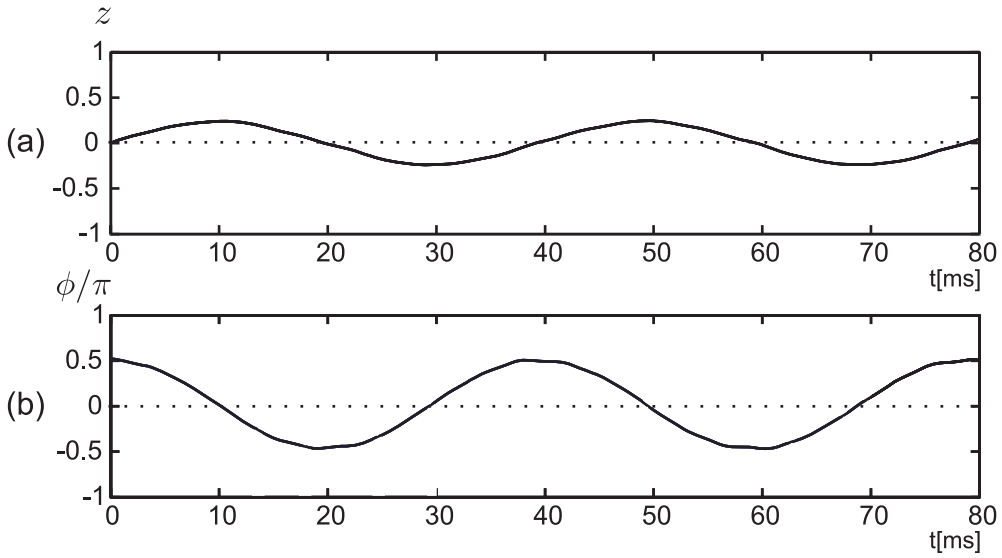

Figure 5.2: (a) Time evolution of the relative population imbalance z for the initial phase difference shown in figure 5.1(c). Clear oscillations of the relative population can be observed. (b) Time evolution of the phase difference ϕ between left and right well. Note that the oscillations of ϕ and z are shifted by $\pi/2$.

Clear oscillations of the relative phase and the population imbalance can be seen that are consistent with the numerical results for the population imbalance induced case discussed in the next section and its experimental confirmation, which will be discussed in section 5.6.
For an actual three-dimensional trap encountered in real experiments not a circular focal spot would be used but an elongated spot, a so called 'light sheet', which has a sharp intensity profile in x-direction but only very little intensity variation lateral to the x-axis, in order to prevent transverse excitations.
The parameters of scanning speed and of the size of the Gaussian beam are uncritical. The scanning process should be completed within $T \leq 1\,$ms and the numerics yield sensible results for $1.8\,\mu\text{m} < d < 3.4\,\mu\text{m}$. Therefore an experimental realisation would be possible.
Note, however, that the regime of self-trapping is not accessible with this method! This can be easily understood by considering the pendulum model described in section 3.2: A rotation of the pendulum, corresponding to the self-trapping case, can only be achieved by giving the pendulum more initial energy than the maximum potential energy of the pendulum. Even for an initially maximally deviated pendulum an additional angular momentum is therefore always necessary. Furthermore, this method requires an extra light beam which has to be moved over the condensate and which was not available at the time.
For these reasons the phase induced Josephson oscillation method has not been used

in the experiment. Using it would, however, be desirable in order to complement the results of our experiments. Stimulated by this fact and promoted by the numerous other possible applications for such an additional, movable light beam, a setup for such a system has been designed and prototypes have been successfully tested in the framework of this thesis. This is being addressed in chapter 6.

5.2.2 Population-Imbalance Induced Josephson Oscillations

In our experiments the method of population-imbalance induced Josephson oscillations is chosen instead. For an initial population imbalance in a symmetric double well, the energies of the two Bose-Einstein condensates in the left and right well, respectively, are different due to the on-site interaction as has been described in section 3.2. Therefore the phase of the two condensates will evolve differently over time, creating an increasing phase difference which in turn initiates the tunnelling dynamics.
The initial population imbalance is obtained by creating an asymmetric double well potential as shown in figure 5.3(a) with a resulting asymmetric atomic population. In the given case, there will be more atoms in the left well than in the right well. The asymmetric potential is achieved by shifting the X-DT beam of the harmonic confinement using the piezo actuated mount of the fibre outcoupler.
In order to start the tunnelling experiments the X-DT is again shifted such that the double well potential becomes symmetric, as shown in figure 5.3(b). This shifting process takes place within 7 ms as could be determined by means of the monitoring quadrant photo diode.

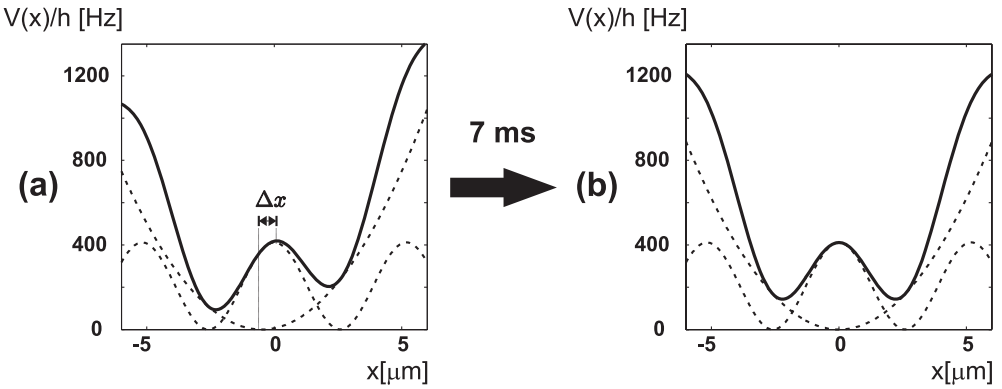

Figure 5.3: (a): Initial asymmetric double well (solid black line) obtained by shifting the harmonic confinement for Δx with respect to the standing wave (both depicted with dashed black lines). (b): In order to start the tunnelling dynamics the potential is again made symmetric. The process takes 7 ms.

The dependence of the population imbalance $z(0)$ on the relative shift Δx between harmonic confinement and lattice potential is shown in figure 5.4 with the solid black line. This data is obtained by numerically calculating the ground state of a BEC in the double well. The grey shaded area depicts the region where Josephson oscillations are expected for our trap parameters. The white areas correspond to the large initial population imbalances leading to self-trapping. The red points show the measured population imbalances for the corresponding relative shift Δx. The error bars represent the statistical errors due to uncertainties of the lattice position and the population imbalance. It can

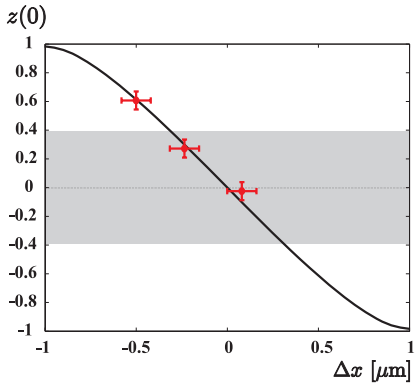

Figure 5.4: The solid line shows the dependence of $z(0)$ on Δx as estimated by numerical calculations. The grey shaded area corresponds to values of $z(0)$ for which Josephson oscillations are expected with our trap parameters. The white area represents the self-trapping regime. The red points depict the measured population imbalances. The error bars represent the errors due to uncertainties in the position fit and the relative population measurement.

be seen that $\Delta x = 350\,\text{nm}$ is already enough to jump from $z(0) = 0$ to $z(0) = 0.4$, where the self-trapping regime starts. This emphasises the need for a stable setup as discussed in section 4.2.2.

5.3 Measuring the Population Imbalance $z(t)$

In order to estimate the population imbalance, a central in x-direction cut through the absorption image of the Bose-Einstein condensate is taken as indicated by the white horizontal line in figure 5.5(a). The corresponding intensity distribution is depicted in 5.5(b) (red curve) and represents the mean of the 13 central pixel rows. It is fitted by a sum of two Gaussians with waists of σ_L and σ_R and amplitudes T_L and T_R for the left and the right Gaussian, respectively. Both Gaussians are plotted with black solid lines.

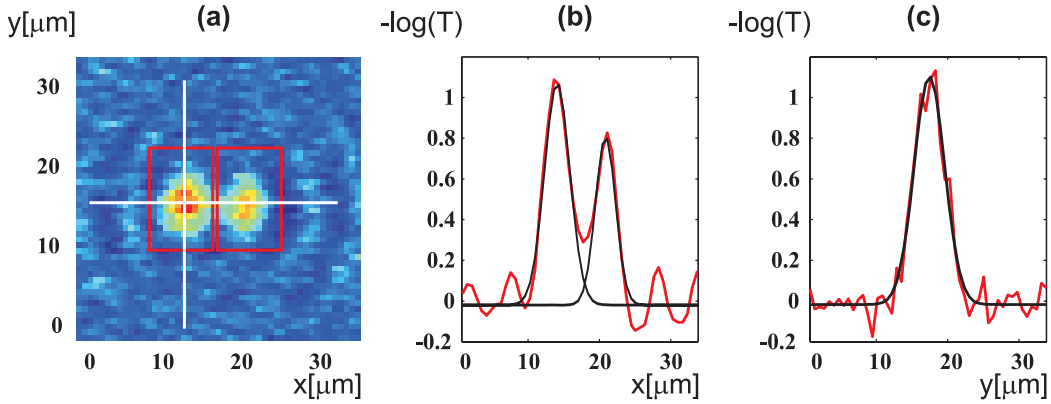

Figure 5.5: (a) shows a typical picture of the BECs in the double well potential after separation (see text). The horizontal white line indicates a central cut in x-direction through the measured intensity distribution, which is plotted in (b) with a red line. The black lines in (b) represent the two Gaussian fit functions. (c) shows a cut in y-direction (red curve) which is indicated by a vertical white line in part (a). The black curve in (c) shows the Gaussian best fit of the width in y-direction.

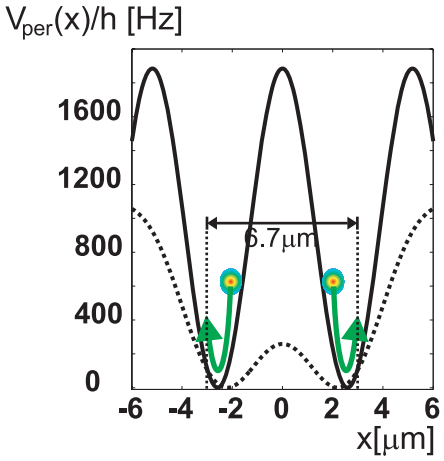

Figure 5.6: The separation of the BECs is increased before taking the absorption image by ramping down the harmonic confinement in x-direction while simultaneously ramping up the periodic potential (black line). Both BECs start oscillating in their respective lattice site. The image is taken at the point of maximum separation, which is $6.7\,\mu$m. The dashed black line depicts the double well potential.

The intensity profile in y-direction is obtained by the same method and indicated by the vertical white line in 5.5(a). It is fitted by a single Gaussian with waist σ_y and amplitude T_L as depicted in figure 5.5(c) with a red curve for the measured intensity distribution and a black line for the Gaussian fit. The intensity distribution is plotted in units of $-\log(T)$. The number of atoms in each well is now calculated as

$$N_L = -\frac{1}{\sigma}\int_{\text{left well}} \log(T(x,y))dA = \frac{1}{\sigma}T_L\frac{\pi}{2}\sigma_L\sigma_y \tag{5.2}$$

$$N_R = -\frac{1}{\sigma}\int_{\text{right well}} \log(T(x,y))dA = \frac{1}{\sigma}T_R\frac{\pi}{2}\sigma_R\sigma_y. \tag{5.3}$$

Here, $\sigma = \frac{\Gamma h\nu}{2I_S}$ corresponding to section 4.3.1 and we assume that σ_y of the condensates in either well is equal. This method overestimates the atom number by a factor of $F = \frac{-log(T(x,y))}{1+log(T(x,y))}$ compared to the high intensity limit described in (4.19), which leads to a total overestimation of the atom number of approximately 20%. This error is afterwards corrected. We then get for z in this specific example:

$$z = \frac{N_L - N_R}{N_L + N_R} = 0.23(3) \tag{5.4}$$

Another method to determine z is to directly sum over the intensity distribution of each well instead of integrating over the fit functions. The area of summation is indicated by the red boxes for the left and right well in figure 5.5(a). Both values are typically very close to each other, in this example $z_{count} = 0.25(4)$.
Due to the significant broadening of our images because of diffraction, the modulation between the two intensity maxima would only be very small if the picture was taken when both condensates are sitting in the double well potential at the well distance of $4.4\,\mu$m.

The fit of the profile in x-direction using a sum of two Gaussians would therefore be vulnerable to fitting errors. Therefore the two wave packets are further separated before taking the image. This is being done by quickly ramping down the harmonic confinement in x-direction while simultaneously ramping up the periodic potential. The two BECs then start to oscillate in their respective wells as shown in figure 5.6. The picture is taken at the point of maximum separation which is about 6.7 μm and which is reached after 1.5 ms.

5.4 Measuring the Phase Difference $\phi(t)$

The phase difference $\phi(t)$ can be measured by means of interference due to the wave character of a Bose-Einstein condensate. If the double well trap is suddenly turned off, both condensates fall down in the gravitational field while expanding because of dispersion. In this 'double slit' experiment, the overlapping wave functions create an interference pattern from which we can extract the relative phase. If we again approximate the BEC by a sum of two Gaussians in x-direction

$$\Psi(x) = A_1 \exp\left[-\frac{(x-x_L)^2}{\sigma_x^2}\right] + A_2 \exp\left[-\frac{(x-x_R)^2}{\sigma_x^2}\right], \tag{5.5}$$

where σ_x represents the width of the two condensates and $x_{L,R}$ the position of the left and the right BEC, respectively. The Fourier transform of (5.5) gives us the interference pattern in the far field:

$$|\Psi(k)|^2 = \exp\left[-2\frac{(k-k_0)^2}{\sigma_k^2}\right]\left[A_L^2 + A_R^2 + 2A_L A_R \cos\left(\frac{2\pi}{d_{TOF}}(k-k_0) - \phi\right)\right]. \tag{5.6}$$

If we again take a central cut in x-direction of a measured interference pattern and fit the resulting intensity profile with (5.6), we can derive ϕ.
A typical interference picture is shown in the left pictures of figure 5.7(a) for a derived $\phi = 0.1(1)\pi$ and of figure 5.7(b) for $\phi = -0.9(1)\pi$. The intensity profiles of the central cuts of both cases are shown on the right side of the figures (red line). The expansion time, i.e. the time of flight was 5 ms in the Josephson oscillation regime and 8 ms in the self-trapping regime.

5.5 Calibrating the Trap Parameters

Trap frequencies of the harmonic confinement and the lattice potential have to be calibrated. The corresponding techniques are explained in detail in [52, 58]. Their description will therefore be restricted to only mentioning the general idea. In the case of the harmonic confinement, the trap frequencies are estimated by giving the condensate an initial 'kick' and directly measuring the frequency of the oscillations which the BEC is then performing in the harmonic trap. The frequencies ν_x, ν_y and ν_z of the oscillations in x, y and z direction correspond to the trapping frequencies of the harmonic confinement:

$$2\pi \times \nu_{x,y,z} = \omega_{x,y,z}$$

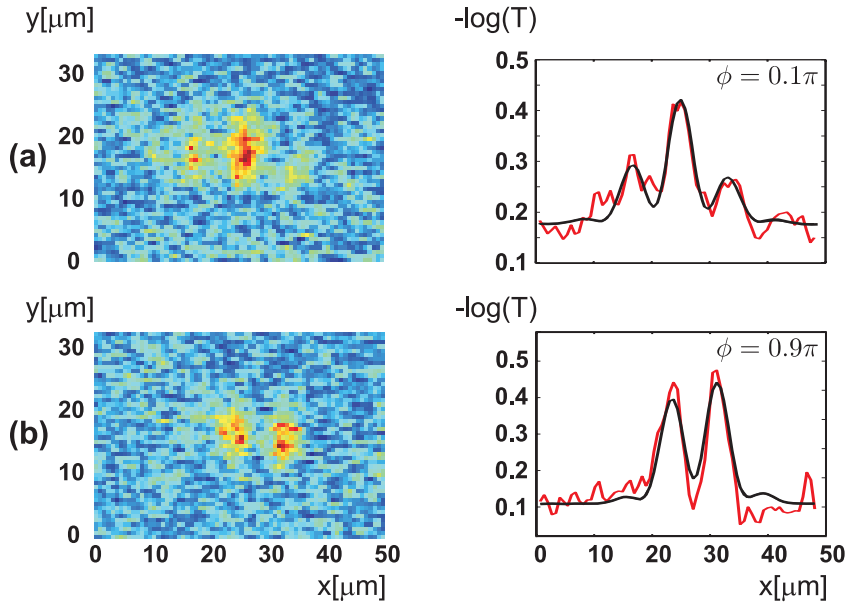

Figure 5.7: Left side: (a) shows a typical interference picture for $\phi = 0.1\pi$. (b) shows a typical interference picture for $\phi = 0.9\pi$. On the right side the corresponding central cuts through the intensity distributions (red line) and the best fits with function (5.6) (black line) are shown.

The lattice potential is calibrated using a similar method as described in section 5.3: A BEC in the double well potential is created and the lattice potential is ramped up while the harmonic confinement is lowered. By measuring the relative distance of the oscillating condensates at different times, the oscillation frequency and thus the depth of the periodic potential can be estimated.

5.6 Results of the Josephson Tunnelling Measurements

In the following, the experimental results of the measurements on the Josephson tunnelling dynamics will be presented. Figure 5.8 shows the first experimental observation of the dynamics of a single Bose-Einstein Josephson junction. Figure 5.8(a) depicts the oscillatory regime. The initial population imbalance is $z(0) = 0.28(6)$ which is below the critical population imbalance $z_c = 0.38$ and corresponds to the case of large amplitude oscillations in the classification in section 3.2.1. The pictures taken at different evolution times of the system clearly show that the atoms, initially in the left well by the majority, tunnel through the barrier to the right side and back again. The oscillation period is $\approx 45\,\mathrm{ms}$.
Figure 5.8(b) depicts the case of self-trapping. At initially $z(0) = 0.62(6)$ the atoms are trapped in the left well. The small amplitude oscillations performed around the nonzero mean value $\langle z(t)\rangle_t$ cannot be resolved. The number of atoms in these experiments was 1150 ± 150. Condensates with different atom numbers were excluded by post-selection. The pictures were taken after separation of the two BECs as described in section 5.3.
A quantitative analysis of the dynamics is shown in figure 5.9(a),(b). We will first focus on the Josephson oscillation regime in figure 5.9(a). The upper graph shows the mea-

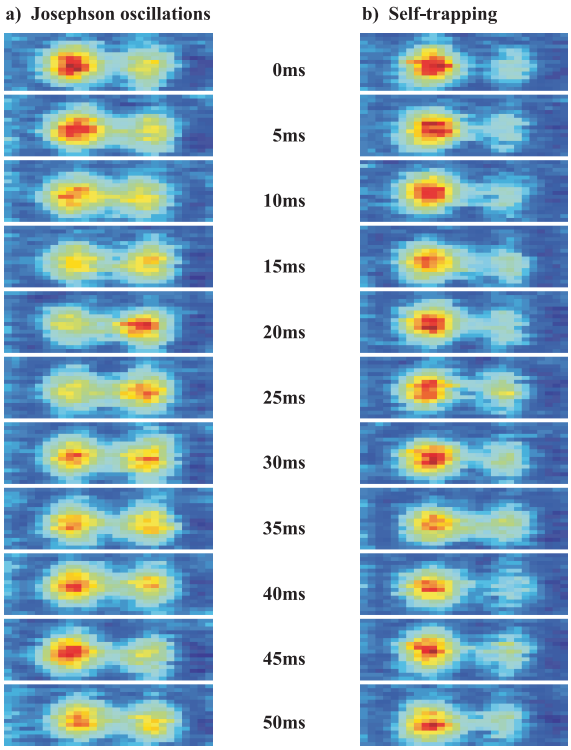

Figure 5.8: First observation of Josephson tunnelling in a single Bose-Einstein Josephson junction. (a) shows the oscillation regime. The atoms are tunnelling from the left to the right side and vice versa. (b) depicts the case of macroscopic quantum self-trapping. The initial population imbalance remains locked on the left side. Each little picture is of size $17.5 \times 9.8\,\mu\mathrm{m}^2$.

sured population imbalance. Each filled circle represents one experimental realisation. The oscillation of a period of 45 ms can be directy seen. The black solid line depicts the results of the numerical simulation using the NPSE for the initial conditions given above. Note that all the numerical calculations of 5.9 do not contain any free parameters. The grey shaded area depicts the area where experimental results are expected if the experimental uncertainties in total and relative atom number N_T and $z(0)$ are taken into account. Both quantities are influencing the oscillation period. Almost all measured points lie within this region showing the excellent agreement of experimental data and theoretical calculation.
The lower picture shows the oscillation of the phase. Each filled circle represents the average of at least five measurements. The error bars represent the statistical error. The solid line again shows the numerical simulation of the development of the relative phase. The insets on the upper side of the graph show representative central cuts through the interference pattern during the phase measurement as described in section 5.4 at the corresponding times.
Figure 5.9(b) demonstrates the self-trapping regime. The measured population imbalance can be seen in the upper graph. Each circle represents a single measurement. The solid line shows the result of the numerical simulation. The predicted small amplitude oscillations cannot be resolved due to the fit errors and the uncertainties of $z(0)$.
The lower graph shows the quasi linear temporal evolution of the relative phase. Each circle denotes the mean of at least five measurements. Again the small amplitude oscil-

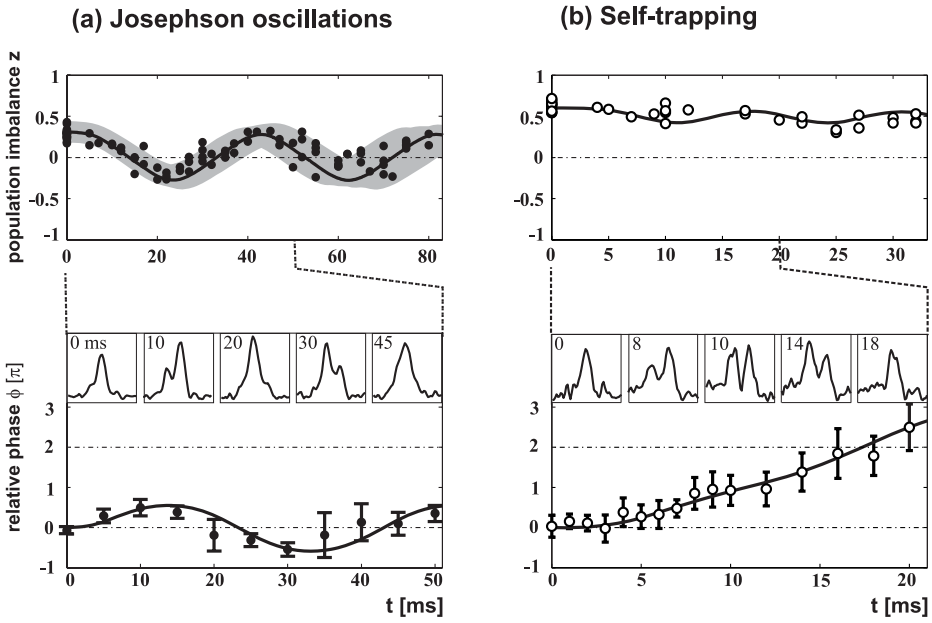

Figure 5.9: Quantitative analysis of the tunnelling dynamics. The graphs of (a) show the oscillatory regime. The upper plot depicts the oscillation of the population imbalance. Each filled circle represents one experimental realisation. The black solid line shows the results of the numerical simulation. The grey shaded area depicts the region where data points are expected if the initial uncertainties of population imbalance and atom number are taken into account, which lead to varying oscillation frequencies. The lower plot of (a) shows the phase development of the oscillatory regime. Each filled circle represents at least five experimental realisations. The error bars denote the standard deviation. The black solid line represents the numerical result. It can be seen that both oscillations are shifted by $\pi/2$. Note, that this plot shows a shorter period of time than the upper graph. (b) depicts the self-trapping regime. In the upper graph, each circle represents one experimental realisation. The black solid line represents the numerical result. The atoms are trapped in the left well. The predicted small amplitude oscillations cannot be resolved. In the lower graph of (b) the quasi linearly increasing phase of the self-trapping case is shown. Each circle represents at least five measurements, the error bars denote the standard deviation. The numerical result is again depicted by the black solid line. Note that all numerical results shown in this figure are obtained without any free parameters. The insets in the lower graphs graph show representative central cuts through the interference pattern at the corresponding times.

lations cannot be resolved. The insets on the upper side of the graph are representative cuts through the intensity distribution of the interference picture.
When looking closely at the graphs it can be observed that the tunnelling dynamics seems to set in with a few milliseconds of delay. This is most obvious in the lower right graph. This delay is due to the fact that the shifting of the X-DT beam which results in the switch from asymmetric to symmetric double well trap as described in section 5.2.2, only takes place with a characteristic time of 7 ms. This fact is being taken into account by the numerical simulations.
These experimental results confirm in an impressive way the theory of Bose-Einstein Josephson tunnelling dynamics, including the two different regimes of macroscopic quantum self-trapping and Josephson oscillations.

Chapter 6

A New Objective: Towards High-Resolution Phase Imprinting and Imaging

6.1 The Need for an Extension of the Setup

The current setup allows for trapping of atoms in a harmonic optical confinement with a superimposed optical lattice. The possible resulting effective trap shapes reach from quasi one-dimensional optical lattices [55, 57] to double well traps. Future planned experiments, such as the creation of dark soliton fans [35, 36] and single lattice site manipulation need an additional narrow light sheet creating a thin singular potential barrier or well. The investigation of phase induced Josephson oscillations (section 5.2.1) even requires a moving light sheet. Thinking further into the future, the need for even more elaborate optical potentials might arise. In order to meet the requirements of future experiments, an extension of the current experimental setup which is capable of creating arbitrary optical potentials for cold atoms has been planned and prototypes have been tested in order to ensure the feasibility.

6.2 Creating Arbitrary Optical Potentials

6.2.1 Holographic Imaging Technique

Generally speaking, two different methods for creating arbitrary optical potentials for cold atoms can be found in current experiments. The first method makes use of holographic images created by a spatial light modulator (SLM) and has originally been applied by Hayasaki [69] and Reicherter [70] as an 'optical tweezer'. An SLM is based on a small liquid crystal array typically with VGA or XGA resolution and of a size on the order of a cm^2. There are various types of SLMs which act either as amplitude or as phase modulators. We will only consider the latter case.
Each pixel of the SLM acts as a variable phase shifting device and can be addressed independently. Therefore, if the SLM is illuminated by a laser beam, the phase of the incident wave can be shifted for each pixel individually and continuously in the range from 0 up to 2π depending on the wavelength. The SLM thus acts as a variable hologram

which, when illuminated by a coherent laser beam can produce arbitrary holographic images. The images represent the fourier transform of the phase pattern on the display. The fourier transform is here performed by the imaging objective [71].
A nice feature of an SLM is the fact that the position of the image plane can be altered without moving the objective. This is possible simply by overlaying a Fresnel-lens ring pattern over the phase pattern creating the holographic image. The image plane will then be shifted by the amount of the focal length corresponding to the Fresnel-lens pattern. This device is a fine and flexible tool for creating arbitrary optical potentials especially for complex intensity distributions and should be kept in mind for future use. It has, however, several drawbacks: Firstly these devices show in practice a varying nonlinear behaviour in the phase shift of each pixel and therefore might have to be calibrated extensively. Secondly, the response time of a liquid crystal display is on the order of at least 10 ms for modern devices and therefore an SLM is too slow for creating time varying optical potentials in the timescale of the experimental dynamics. Since the use of time dependent optical potentials can not be excluded in the future we will instead consider a different method.

6.2.2 Time Averaged Optical Potentials

Although being too fast for the response time of an SLM the atoms are slow enough for applying another technique. The characteristic time scale of the dynamics of a Bose-Einstein condensate is milliseconds. If a focussed, detuned laser beam is steered over the condensate in a given pattern in a time $T \leq 1$ms the atoms will only experience the effective potential integrated over T. If the intensity distribution created by the laser beam during time T is called $I(\mathbf{r}(t);t)$, the resulting potential $V_{seq}(\mathbf{r})$ of the pattern sequence will thus be

$$V_{seq}(\mathbf{r}) = AI_{seq}(\mathbf{r}) = A\frac{1}{T}\int_0^T I(\mathbf{r}(t);t)\,dt. \tag{6.1}$$

Where $A = \frac{\hbar\Gamma^2}{8I_S}\frac{2}{3}\left(\frac{1}{\delta_{D2}} + \frac{1}{2\delta_{D1}}\right)$ following equation (4.5).
For a singular burst of this sequence with appropriate intensity, $V_{seq}(\mathbf{r})$ represents a phase imprinting pattern as described in 5.2.1. Following equation (5.1) the phase of the condensate after the burst is thus

$$\psi(\mathbf{r},T) = \exp[-iTV_{seq}(\mathbf{r})/\hbar]\psi(\mathbf{r},0). \tag{6.2}$$

If this pattern is continuously repeated, V_{seq} just represents an additional constant potential term in the GPE. Slightly varying the sequence in each cycle results in a temporally varying potential.
The spatial resolution of this pattern is only limited by the spot size of the focus. Since typical experiments use small atomic clouds of the size of a few microns or a few tens of microns, these optical potential patterns have to be very small and therefore a well corrected objective with a high numerical aperture is absolutely crucial. The design of the objective, which can also be used as an additional high resolution imaging system, will be explained in section 6.6.

6.3 Experimental Setup of the Phase Imprinting Device

6.3.1 An Overview

The setup of the phase imprinting system is very similar to that of optical tweezers known from biology and biophysics, an example of which can be found in [72]. The working principle will now be discussed by means of a setup which is appropriate for our specific experimental configuration. It can be seen in figure 6.1. The laser beam which is

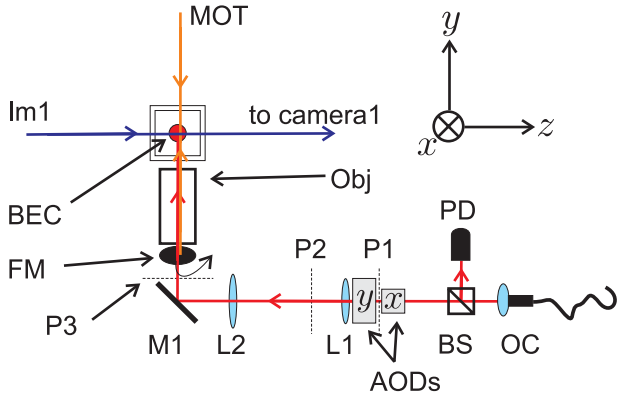

Figure 6.1: Side view of phase imprinting setup. OC: outcoupler (laser source); BS: beam splitter; PD: photodiode for intensity stabilisation; AODs: beam steering device (Acousto Optical Deflectors), direction of deflection as indicated; L1,L2: lenses of beam expander; M1: mirror; FM: flip mirror, needed for MOT beam; Obj: objective; P1: back focal plane (BFP) of L1; P2: focal plane (FP) of L1 and BFP of L2; P3: FP of L2 and BFP of objective; BEC: Bose-Einstein condensate; Im1: imaging beam; MOT: beam for MOT (all orange beams); Note the coordinate system in the upper right.

appropriately detuned to the D2 transition of ^{87}Rb is transferred to the experiment from a Ti:Sa laser by an optical fibre. It enters at the outcoupler (OC) of the fibre. A fraction of the light is then guided onto a photodiode (PD) by means of a beam splitter (BS) in order to measure the intensity of the beam. The intensity can be actively controlled and stabilised by a PI loop and can be adjusted with an acousto optic modulator (AOM) which is placed before the fibre (not shown).
The main beam then passes two (see figure 6.2) acousto optic deflectors (AOD) that are vertically aligned to each other and are used as a beam steering device. The working principle of an AOD is described in section 6.3.4. The right AOD deflects the beam in x-direction and the left one in y-direction. The x-axis is perpendicular to the plane shown in figure 6.1.
After being deflected, the beam passes the two lenses L1 and L2 of a beam expander, enlarging it to a size of 28 mm, for which the objective (Obj) is designed.
The beam is then guided upwards into the objective by mirror M1. Resulting from this, the beam steering in y-direction effectively moves the focal spot in z-direction in the focal plane. Note that in order to have a clear optical path, the flip mirror FM has to be moved out of the way. This mirror is needed for the MOT beam entering the vacuum chamber from below in the beginning of the experimental procedure (see section 4.1.1). The MOT beam, however, is turned off in this stage of the experiment.

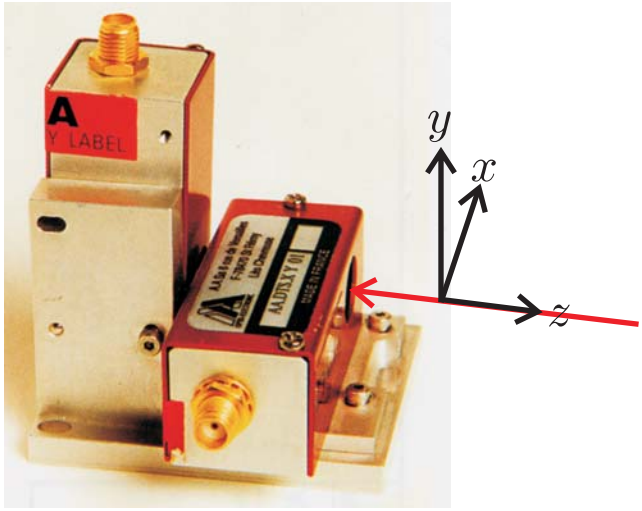

Figure 6.2: Picture of an acousto optic 2-axis deflector of the *AA.DTS.XY* series from *AA Opto-Electronic*. The two AODs are aligned vertically to each other. The beam propagation direction is indicated by the red arrow. Source: *AA Opto-Electronic*

The laser light then enters the objective and is focussed onto the Bose-Einstein condensate (BEC), where the focal spot is moving according to the deflection by the AODs.

6.3.2 The Beam Steering Device and Projection Optics

We will now take a closer look at the beam steering device and projection optics. The setup is depicted in figure 6.3, where the objective (Obj) is displayed as a thin lens for simplicity reasons.
In order to ensure that the focussed beam in the focal plane of the objective (OFP) only changes in position and not in angle, it has to be made certain that the beam only changes in angle but not in position in the back focal plane of the objective, which is P3 in figure 6.3. This is guaranteed if the focal plane of the beam expander coincides with the back focal plane of the objective and if the beam steering device is located in the back focal plane of the beam expander, which is P1 in our case. In order to get a best approximation for this situation, the two AODs of the beam steering device have to be placed as closely together as possible and they are to be placed such that the back focal plane of the beam expander is in the centre between the two AODs.
The distance d of the deflected focus to its central position is given by

$$d = \frac{f_{L1} f_{Obj}}{f_{L2}} \tan(\alpha). \tag{6.3}$$

α here represents the deflection angle. It is therefore inversely dependent on the beam expansion ratio $r_{exp} = f_{L2}/f_{L1}$. Typical maximum deflection angle ranges of AODs are 45 mrad (± 22.5 mrad around a centre deflection angle). For $r_{exp} = 1$ this would give $d_{max} = \pm 473\,\mu$m in x- and z-direction, using $f_{Obj} = 2.1$ cm.
As already mentioned, the beam entering the objective has a diameter[1] of 28 mm. The

[1]We will consider exclusively Gaussian beams throughout this chapter. Here, 'beam waist' w is

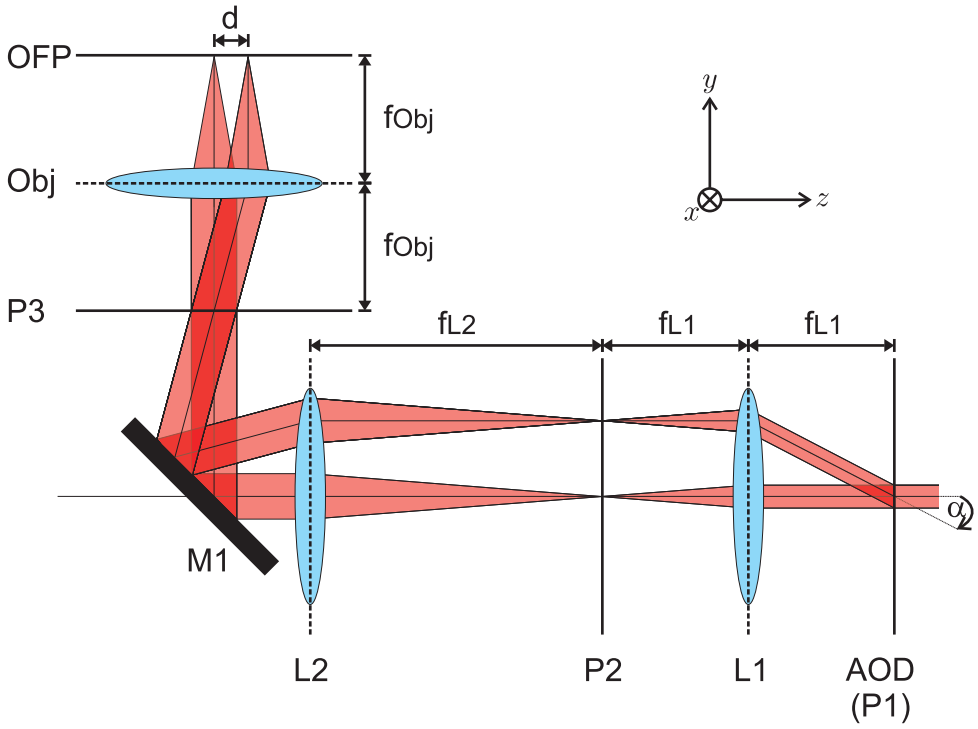

Figure 6.3: Beam path of the deflected and the undeflected beam.

expansion ratio and thus the usable focal field of the objective therefore depends on the size of the incoming beam. This is limited by the size of the AOD aperture. Generally spoken, AODs exist with circular aperture sizes of up to 15 mm but one has to consider that the larger the active aperture, the slower the AOD can alter the beam direction due to the longer running time of the acoustic waves in the AOD (see section 6.3.4). Therefore a certain compromise between maximum speed and maximum deflection angle has to be found. Typical values for a random access time of an AOD are 1.5 μs per μm of beam diameter. A possible solution for our case would be the two axis deflector *AA.DTS.XY 400* from *AA Opto-Electronic* (see figure 6.2) with an aperture of 6.7 mm combined with the fibre collimator *60FC-4-G25-10* from *Schäfter und Kirchhoff* which collimates the laser beam to a diameter of 5.65 mm. A fivefold expansion of the beam yields the desired beam size of 28 mm and a deflection distance of $d = \pm 95\,\mu$m. The random access time of this AOD is specified as 10.3 μs.
Note that a large beam deflection is also desirable in order to be able to react flexibly on position changes of the BEC without needing to mechanically move the objective: The magnetic and optical trap setup has to be re-adjusted every few weeks in order to restore efficient cooling and condensing which can result in a position change of the BEC on the order of a few tens of microns.

defined as the $1/e^2$-radius of a Gaussian, i.e. for a beam profile $\exp\left[-2\frac{x^2}{w^2}\right]$, and 'beam diameter' or 'beam size' as $d := 2w$.

6.3.3 Detailed Objective Mounting

We will now take a closer look at the mounting of the objective close to the vacuum chamber, which is shown in figure 6.4. Due to spatial constraints and the sensitivity of the optical alignment the actual construction has to be undertaken with great care. The phase imprinting beam (red) enters the setup from the right, is deflected upwards by means of a mirror and is led into the objective.
The MOT beam (yellow), which is needed at the beginning of every experimental sequence enters the setup vertically to the image plane (x-direction) and is also deflected upwards into the same beam path. Since a collimated MOT beam is needed at the place of the atoms, the beam passes a focussing lens before entering the objective. Both the lens and the mirror for the MOT beam are mounted on the stage of a flipper mirror (not shown) and are moved out of the way before the phase imprinting beam is turned on.
The objective is movable in all directions. The motion in y-direction is performed by means of a motor controlled translation stage (*Physik Instrumente, M-111.2DG*) with a step resolution of 50 nm. This translation stage is to be mounted on a massive aluminium block (grey, on the left side) in order to guarantee good stability. Please note that precautions have to be undertaken that the objective *physically cannot touch* the vacuum glass cell. This is critical since the distance between objective and glass cell is only 2 mm. The aluminium block in turn is mounted on a two-axis translation stage which can be moved in x- and z-direction. This is necessary for simplifying the alignment of the objective and beam path and to have a coarse adjusting possibility for hitting the atomic cloud with the focal spot (fine adjusting can be performed by beam deflection).
When setting up the whole phase imprinting system, the fibre collimator, the AODs and the beam expander lenses are most practically mounted and fixed on a single, stable rail. Thus, they can be shifted as a whole when aligning the last mirror and the objective which is of great practical advantage for the setup procedure.

6.3.4 Working Principle of Acousto Optic Devices

Acousto optic modulators and acousto optic deflectors have the same working principle. An light beam impinges on a crystal (here $Te0_2$) in which sound waves of a frequency of typically $\nu_a = 100\,\mathrm{MHz}$ are propagating. These acoustic waves are generated by a piezoelectric transducer that is driven by a radio frequency (RF) signal source. The laser beam is Bragg diffracted at the spatially periodic density variations in the crystal corresponding to compressions and rarefactions created by the travelling acoustic wave, which form an effective Bragg diffraction grating. The total beam deflection α of the primarily used first Bragg diffraction order is twice the Bragg angle θ:

$$\alpha = 2 \arcsin\left(\frac{\lambda}{2\lambda_a}\right) \approx \frac{\lambda \nu_a}{c_a} \tag{6.4}$$

Here, λ is the laser wavelength, $\lambda_a = c_a/\nu_a$ the acoustic wavelength, c_a represents the speed of sound in the crystal and ν_a is the RF frequency of the acoustic waves. Typically more than 70% of the incident laser light can be deflected into the first Bragg diffraction order for a well aligned AOM. In order to deflect a beam at an arbitrary angle, the RF frequency can be varied within in a certain range ($\pm 22.5\,\mathrm{MHz}$ in the case of the *AA.DTS.XY 400* at $\lambda = 870\,\mathrm{nm}$) around some device-specific centre frequency. Acousto optic devices have three major applications:

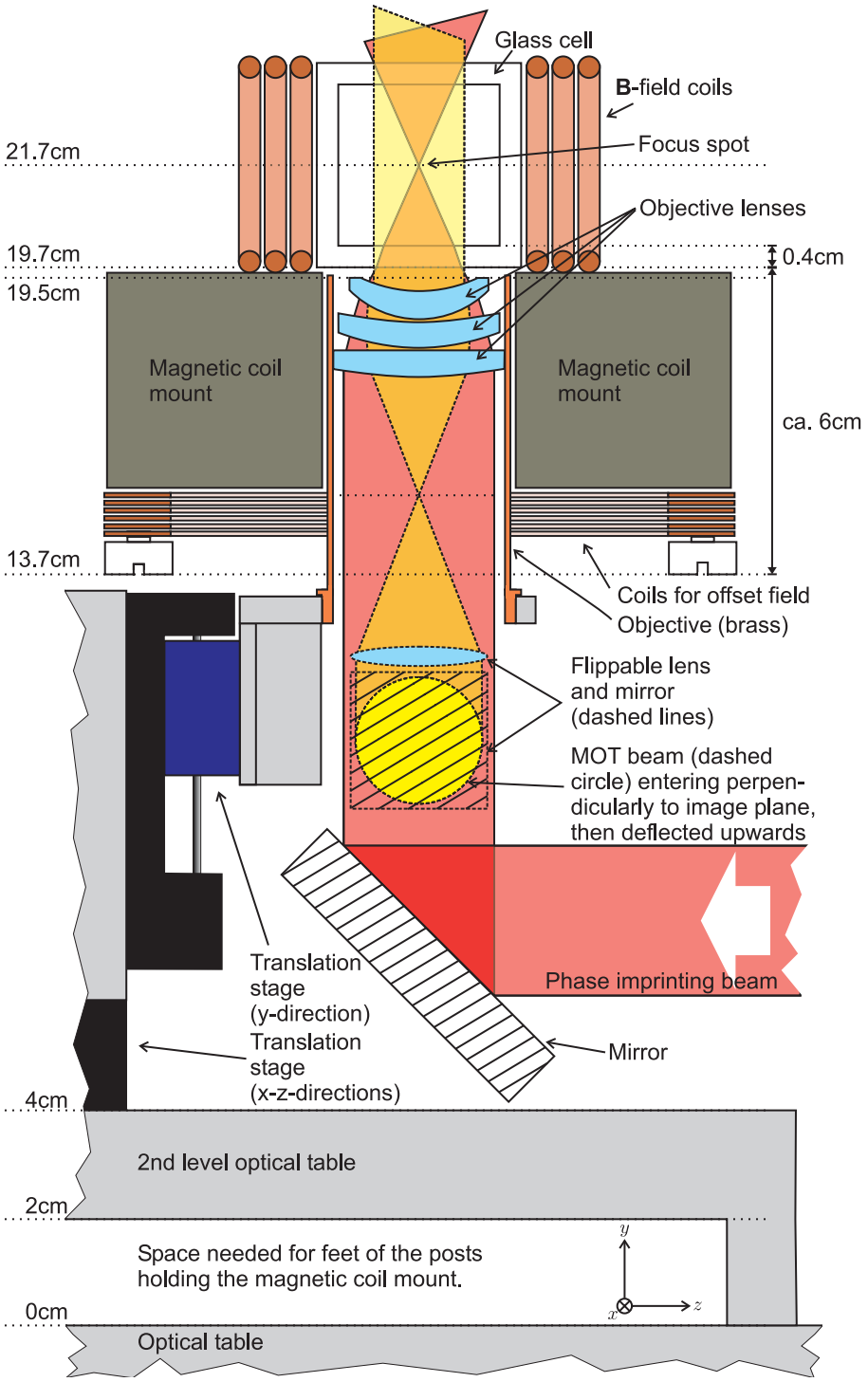

Figure 6.4: Detailed scheme of the mounting of the objective at the vacuum chamber. The proportions of the figure are exact. Scale: 3/4

- Beam deflection.
- Beam intensity modulation, since the intensity of the first Bragg diffraction order is dependent on the amplitude of the acoustic RF signal.

- Frequency shifting: The frequency of the first diffraction order is $\nu_{defl} = \nu + \nu_a$, where ν is the frequency of the incident beam.

The major difference between AOMs and AODs is the fact that AODs are optimised for large beam deflection angles and large beam diameters, whereas AOMs are primarily used for intensity modulation and frequency shifting. According to equation (6.4), the deflection angle depends inversely on the speed of sound, which in TeO_2 depends on the direction of propagation relative to the crystal symmetry axes. Therefore, using different propagation directions of the acoustic waves, c_a can be chosen to be typically 4200m/s for an AOM or 650 m/s for an AOD. For 810 nm, this yields a deflection of ≈ 0.2 mrad/MHz for an AOM and ≈ 1.2 mrad/MHz for an AOD.
In order to create a time averaged light intensity pattern $I_{seq}(\mathbf{r})$ as in equation (6.1), a corresponding time varying RF frequency pattern has to be applied to the two AODs. The most flexible way to create complex patterns would be the use of an arbitrary waveform generator (AWG). Two AWGs are available in the laboratory (*Sony/Tektronix AWG 420* and *HP 8770A*) and could be used for this purpose. However, the sampling frequencies of 200 MHz and 125 MHz, respectively are not high enough to create smooth sinusoidal waves up to 120 MHz as needed for the AODs. This can be circumvented by creating a 60 MHz RF base frequency with a voltage controlled oscillator (VCO) and mixing it with the variable RF signal from the AWG.
Simple patterns (see section 6.4.3) can also be created by only using a VCO and varying the input voltage of the VCO appropriately with a waveform generator and directly use the RF output of the VCO. This method, however, does not allow amplitude modulation of the RF frequency and therefore intensity modulation of the focal spot.

6.4 Feasibility Study

In order to study the feasibility of the setup described in section 6.3 and in order to gain experience with beam steering techniques, a simple test setup was constructed. The goal was firstly to determine if sufficiently small spot sizes can be reached in practice already using a custom 'off-the-shelf' lens as objective instead of a special, customised objective. The same question arises for the lenses of the beam expander. Secondly, to test whether the use of acousto optic devices as beam steering devices is practical.

6.4.1 Estimating the Spot Size

The process of designing a customised objective which takes into account our specific spatial constraints and optical path is a lengthy and costly one. Therefore the commercial lens *AC300-050-B* from *Thorlabs* has been tested in order to measure the experimentally obtainable size of the focal spot. The lens has a focal length of $f = 5$ cm and a usable circular lens area of 2.2 cm of diameter. For a collimated incident beam in the Gaussian TEM_{00}-mode, the minimum spot size according to Gaussian beam optics is given as [73]:

$$d := 2w_f = 2\frac{\lambda f}{\pi w_0} \tag{6.5}$$

Here, $w_0 = 1.05\,\text{cm}$ is the $1/e^2$-waist of the incoming beam, w_f is the waist in the focal plane and $\lambda = 810\,\text{nm}$ is the wavelength of the detuned laser. With the values given, we get $d_f = 2.45\,\mu\text{m}$ which lies in the range for using it as a phase imprinting beam for the phase induced Josephson oscillations.
The spot size cannot directly be measured experimentally by means of a beam profiler or a CCD-camera, since the pixels of these devices are typically larger than the spot size. The method used instead consists of a slit aperture of $2\,\mu\text{m}$ width and 2 mm height, which is mounted on a translation stage and is moved through the focus plane (vertically to the beam) in steps of $0.5\,\mu\text{m}$ by means of a micrometre screw. Fixed behind the slit aperture and moving with it is a photodiode measuring the intensity of the light coming through the slit aperture. The focal plane can be found by moving the slit aperture along the beam direction (z-axis) while also varying its position laterally to the beam: The position z_f of the focal plane is located at the position where the maximum intensity falls onto the photodiode. The intensity of the laser beam is actively stabilised.

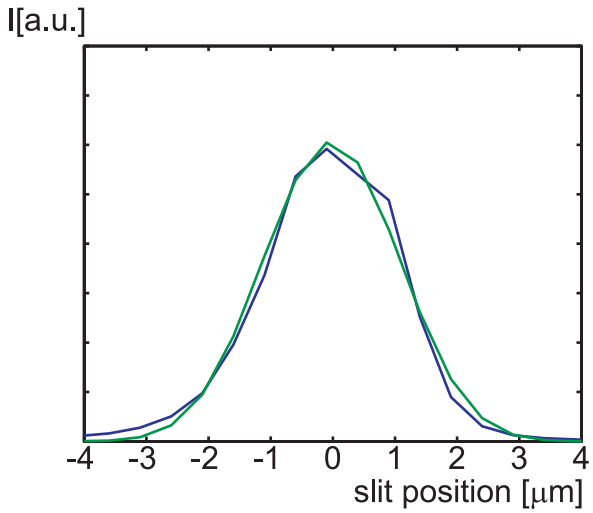

Figure 6.5: Blue line: Measured intensity profile using the slit aperture method (see text). Green line: Best fit for beam size $d_f = 3.6\,\mu\text{m}$

The intensity measured by the photodiode while 'cutting' through the focus with the slit aperture is depicted in figure 6.5 (blue line). The green line in this figure depicts the intensity distribution expected for a Gaussian beam of size $d_f = 3.6\,\mu\text{m}$ if measured by the method described above. This represents the best fit of the blue curve for theoretical beams with varying spot sizes.
Although the experimental value is expected to be larger than the theoretical value due to lens errors, such a big discrepancy was not expected. A reason could be that the incoming beam is not perfectly Gaussian due to the imperfection of the beam expander. The beam expander performs a tenfold expansion of the beam using two standard lenses of focal lengths $f_1 = 1.5\,\text{cm}$ and $f_2 = 15\,\text{cm}$. Although the intensity profile has been controlled thoroughly during the setup as well as the collimation using a phase plate, the result could not be optimised any further with the given optics. Please keep in mind that the glass plate of the vacuum chamber which will be between objective lens and spot will also add aberration which cannot be compensated using a lens 'off-the-shelf'.
In conclusion, in order to get effective spot sizes that are small enough for single lat-

tice site manipulation a customised objective will be needed as well as a thoroughly constructed beam path especially considering the beam expander.

6.4.2 Test Setup For a Moving Light Sheet

In order to investigate the usability of acousto optic devices for our purposes, a simple test setup has been constructed as shown in figure 6.6. This setup was primarily designed to fulfil the needs for phase imprinting in a double well such as described in section 5.2.1 and the investigation of dark soliton fans. Therefore a movable (in x-direction) light sheet has been created. Since an AOD was unavailable at the time, the tests were performed

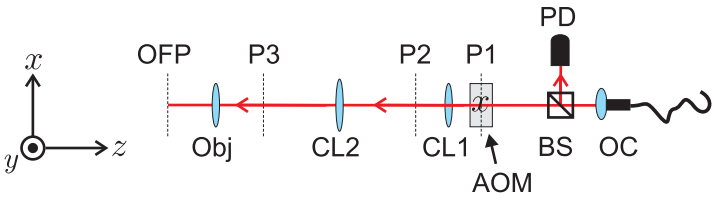

Figure 6.6: Setup to test AOM as beam steering device. OC: fibre collimator; BS: beam splitter; PD: photodiode; AOM: AOM for beam deflection in x-direction; CL1: cylindrical lens, first lens of beam expander; CL2: cylindrical lens, second lens of the beam expander which expands the beam in x-direction; Obj: objective lens; P1: back focal plane of CL1, the AOM is centred in this plane; P2: focal plane of CL1 and back focal plane of CL2; P3: focal plane of CL2 and back focal plane of Obj; OFP: objective focal plane

with an AOM (*Crystal Technologies, 3110-120*) as deflection device.
As shown in the setup in figure 6.6 the laser beam of $\lambda = 810\,\mathrm{nm}$ is provided via an optical fibre. The use of optical fibres is recommendable since they are very good mode filtering devices and, using the appropriate fibre, provide a perfect Gaussian TEM_{00} mode. The fibre collimator (OC) collimates the beam to a diameter of 0.6 mm which just fits into the active aperture of the AOM ($2.5 \times 0.6\,\mathrm{mm}^2$). For larger beams the quality of the mode in the first Bragg diffraction order suffers significantly.
After having passed the AOM which in this test setup does only deflect the beam in x-direction, the beam is expanded by a factor of $r_{exp} = 16.7$ in x-direction by means of two cylindrical lenses CL1 and CL2 with focal lengths $f_1 = 15\,\mathrm{mm}$ and $f_2 = 250\,\mathrm{mm}$, where the focal plane of CL1 is chosen to be in the middle of the AOM crystal. This expansion reduces the deflection by the same factor according to equation (6.3) and therefore to a deflection rate of only $\approx 12\,\mu\mathrm{rad/MHz}$.
Using cylindrical lenses, the beam stays collimated in y-direction and is of the form of an ellipse flattened in y-direction at the position of the spherical objective lens (Obj). According to equation (6.5) the size of the focussed spot is inversely dependent on the size of the incident beam due to diffraction. This way the desired narrow light sheet of now inverted aspect ratio in the focal plane is obtained, i.e. it is elongated in y-direction and narrow in x-direction.
A picture of the beam shape can be seen in figure 6.7. It also shows a second, less intense light sheet to the right. This represents the zeroth order of diffraction. The zeroth order can in principle be filtered out by blocking it in the focal plane P2 of the beam expander, between CL1 and CL2.

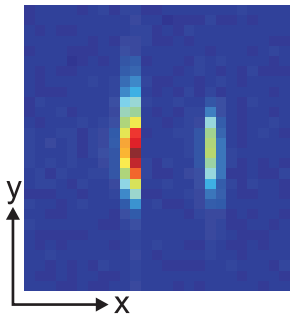

Figure 6.7: Picture of light sheet. One pixel corresponds to 9.9 μm. The less intense light sheet to the right comes from the zeroth diffraction order of the AOM and can in principle be blocked (see text). Note that although the light sheet is thinner than the pixel size, it illuminates two pixel columns and thus appears to be broader than it actually is.

Measuring the Width of the Light Sheet

The slit method described in section 6.4.1 is not preferable for determining the width of the light sheet in this case since a parallel alignment of the light sheet and the slit cannot easily be achieved. Therefore the beam was measured using a CCD-camera (*PCO PixelFly*). The pixels of the camera have a size of $9.9 \times 9.9\,\mu\text{m}^2$ and are therefore much bigger than the expected width of the light sheet in x-direction[2] , which according to equation 6.5 is estimated as $d_{f_x} = 5.2\,\mu$m for the focal length $f = 5\,$cm for the objective and an incident beam size $d_{0_x} = 2w_{0_x} = 16.7 \times 0.6\,\text{mm} = 10\,\text{mm}$. It is therefore impossible to directly record the beam profile in the focus and estimate the beam size by performing a Gaussian fit.
Instead, the beam size $d_x(z)$ in x-direction is measured for several points in the range of approximately $-2.5\,\text{mm} < \Delta z < 2\,\text{mm}$ before and after the focus position z_f. The obtained data for the dependence of the beam width $d_x(z)$ on z is fitted with the theoretical beam size

$$d_x(z) = 2w_{f_x}\sqrt{1 + \left(\frac{z - z_f}{z_r}\right)^2}, \tag{6.6}$$

where $z_r = \frac{\pi w_{f_x}^2}{\lambda}$ is the Rayleigh length. The fitting parameter were z_f and w_{f_x}. The fit can be seen in figure 6.8(a). Figure 6.8(b) shows a magnification of the central region (indicated as small box in figure 6.8(a)). The deviation of the theoretical beam path and the experimental beam path at the focus region are due to the fact that the fitting of the beam size in the focus region overestimates the spot sizes due to the large pixel size. The inset picture of figure 6.8(b) shows a typical image from the focal region. It can be seen that only one pixel row is illuminated. Therefore the fit cannot reach a width $< 9.9\,\mu$m. The actual size of the light sheet as estimated by this method is $d_{f_x} = 5.90(2)\,\mu$m.

[2]The reason why the beam seems to be broader than one pixel column in figure 6.7 is due to the fact that the light sheet is located such that it illuminates two neighbouring pixel columns.

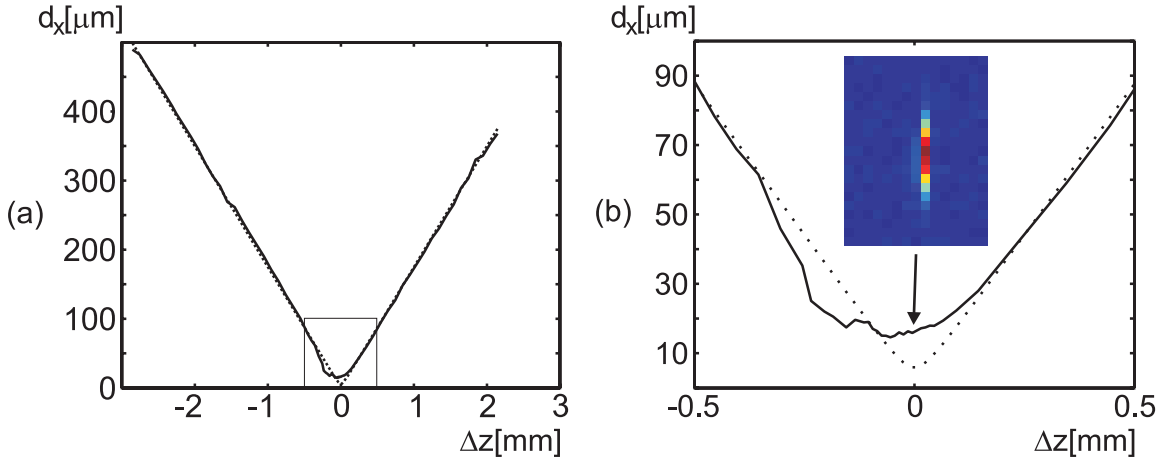

Figure 6.8: (a): The solid line depicts the width d_x of the light sheet plotted against distance Δz from the focal plane, the dashed line shows the best fit according to equation (6.6). (b): Magnification of the central region as indicated by the box in (a). The inset picture shows an image of the light sheet in the central region.

Measuring the Deflection

After estimating the spot size, the beam deflection has been measured quantitatively. Figure 6.9 shows the beam position plotted against the AOM driving frequency (solid line). The linear position fit (dashed line) yields a deflection of 560(20) nm/MHz, which

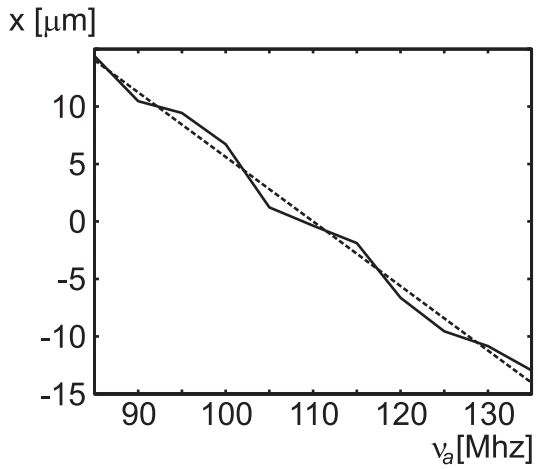

Figure 6.9: Solid line: x-position of light sheet plotted against RF frequency applied to the AOM. Dashed line: Linear best fit. $x = 0$ is defined at as position at the centre frequency $\nu_a = 110\,\mathrm{MHz}$ of the AOM.

corresponds to an angular deflection of $11.2(4)\,\mu$rad considering $f = 5\,\mathrm{cm}$.

6.4.3 Creating Simple Patterns

After these measurements the setup has been modified and the cylindrical lenses were exchanged by spherical lenses. Now the creation of simple patterns was tested, using

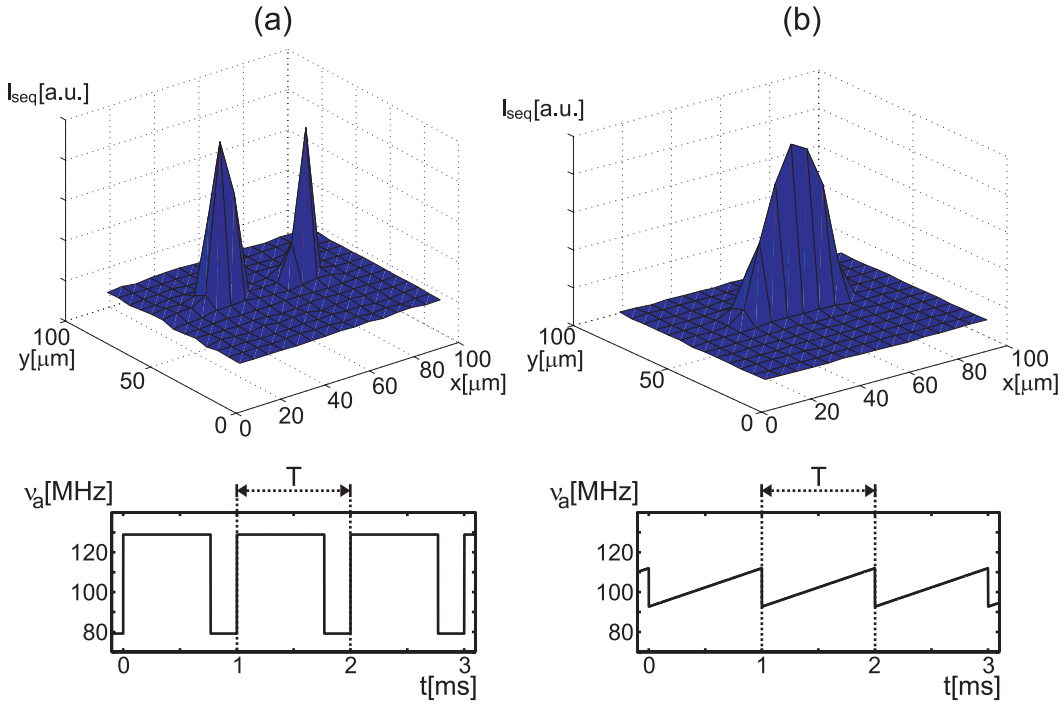

Figure 6.10: Upper figures: Intensity distribution I_{seq} of the moving spot integrated over time $T = 1\,\text{ms}$. (a) Two discrete frequencies have been applied to the AOM consecutively as shown in the lower picture. (b) a frequency ramp has been applied to the AOM resulting in a time averaged light sheet. The frequency ramp is shown in the lower figure.

a VCO as RF source. The upper images in figure 6.10 show the time averaged intensity distribution I_{seq} for two cases. Figure 6.10(a) shows I_{seq} for two different, discrete voltages successively applied to the VCO. This results in two discrete RF frequencies, $\nu_{a_1} = 128.9\,\text{MHz}$ and $\nu_{a_2} = 79.2\,\text{MHz}$ at the output of the VCO which were amplified and fed into the AOM. The RF signal applied to the AOM is shown in the lower graph. The exposure time of the camera was $T = 1\,\text{ms}$ and is indicated by the dashed lines. Two distinct light spots of the same time averaged intensity can be seen in the intensity profile of (a). The reason why ν_{a_1} has been applied longer (0.769 ms) than ν_{a_2} during the sequence length T is the fact that the deflection efficiency of the AOM depends on the RF frequency and is less for 128.9 MHz than for 79.2 MHz. This of course has to be taken into account when creating time averaged potentials.
Figure 6.10(b) shows the case where the RF frequency has been linearly ramped from 92.7 MHz to 112 MHz within T as shown in the lower graph. The resulting time averaged potential shown in the upper picture represents a light sheet. The grid in the pictures displays the pixel size of the camera (*Roper Scientific, CoolSnap ES*) which are of a side length of $6.45\,\mu\text{m}$.
Complex patterns were not feasible with this setup since the deflection range is only approximately five times the spot size.

6.4.4 Important Aspects of Acousto Optic Devices

Concluding this section about beam steering by means of acousto optic devices a short summary of important aspects shall be given that have to be taken into account when

setting up an arbitrary potential generating system.

- The deflection range depends inversely on the beam expansion rate after the AOD. A large beam size on the other hand is crucial for obtaining small spot sizes due to the diffraction limit. Circumventing the problem by already deflecting a large beam with the AOD has the negative side effect that for large AOD aperture sizes the steering speed decreases.

- Beam expansion is obviously a critical subject where great care and good lenses have to be used in order to preserve the Gaussian mode of the beam. Generally spoken, the beam should not be expanded more than necessary.

- The intensity of the deflected beam depends on the RF frequency. This has to be characterised in order to be able to take the effects into account when creating the time averaged potentials.

6.5 High-Resolution Imaging

The objective of the phase imprinting device can alternatively be used as an additional imaging objective in order to be able to not only image the BEC in the x-y-plane but also in the x-z-plane. Apart from the use in the actual experiments this would also facilitate every day's lab routine significantly, since the calibration of the harmonic trap in z-direction, which can hitherto only be done indirectly [52], becomes much easier.
The high numerical aperture of the new objective promises an excellent resolution of this second imaging path. Following equation (4.39) we get an ideal resolution of $r_{Sparrow} < 0.9\,\mu$m, inserting $\lambda = 780\,$nm, $a = 10\,$mm and $z_1 = 23\,$mm for a tenfold magnification (for data on the objective see the following section).
A sample setup for the dual use of the objective is shown in figure 6.11(a) in side view and in figure 6.11(b) in top view. The additional imaging beam (Im2) enters the setup from above. MOT beam MOT1 is guided into the chamber on the same path by means of a beam splitter cube (BS3). After having illuminated the condensate, the imaging light passes the objective which is placed in focal distance $f_{Obj} = 21\,$mm to the BEC and collimates the light, which corresponds to a projection to infinity. The imaging beam is then deflected in z-direction by mirror M1 and guided to camera 2 either by means of a flip mirror (FM2) or alternatively by a beam splitter cube (BS2, not shown).
The former method has the advantage that additional aberration of the phase imprinting beam and the imaging light due to the beam splitter cube can be prevented, which might be necessary in order to be able to completely exploit the new objective. Furthermore, no imaging light is lost at the beam splitter cube which is especially important in the case of fluorescence imaging. It has, however, the great disadvantage that the objective cannot be used for phase imprinting and imaging in the same experimental sequence since the flip mirror cannot be moved out of the phase imprinting beam path quickly enough.
The imaging light is projected onto camera 2 by lens L3. The distance z_{L3} between lens L3 and the back focal plane of the objective (P3) as well as the distance between L3 and camera 2 has to be equal to the focal distance f_{L3} of lens 3. The magnification of the image is then given by $M = f_{L3}/f_{Obj}$. For $f_{Obj} = 21\,$mm and a tenfold magnification

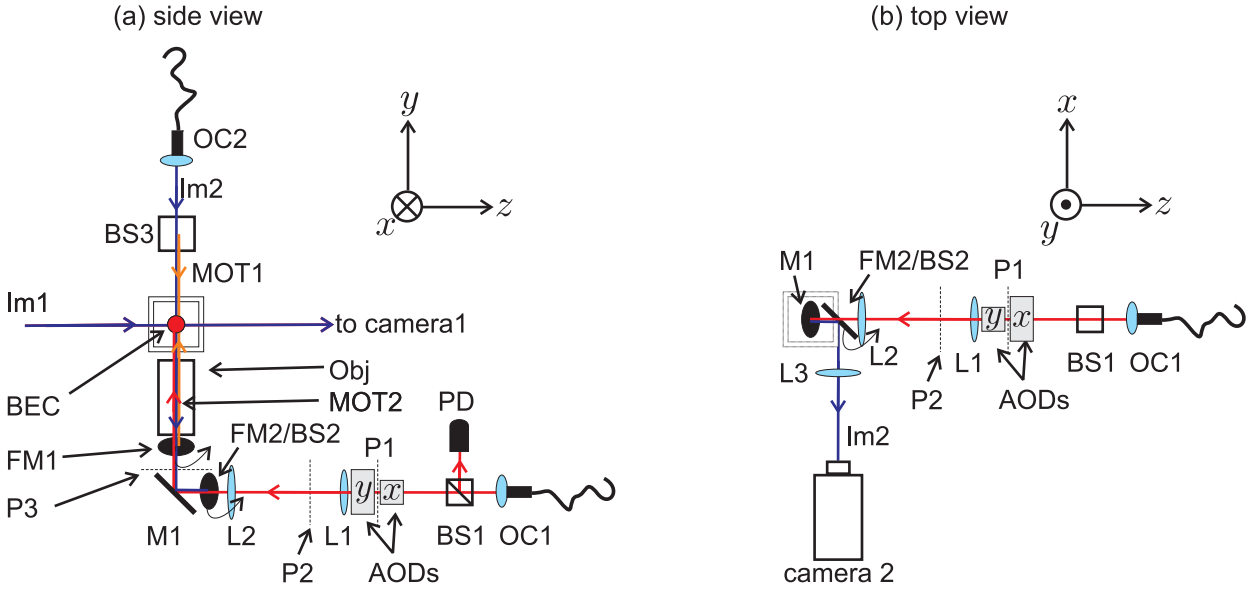

Figure 6.11: (a) Side view of combined imaging and phase imprinting system. OC1: outcoupler (phase imprinting beam source); BS1: beam splitter; PD: photodiode for intensity stabilisation; AODs: beam steering device (Acousto Optical Deflectors), direction of deflection as indicated; L1,L2: lenses of beam expander; M1: mirror; FM1: flip mirror, needed for MOT beam; Obj: objective; P1: back focal plane (BFP) of L1; P2: focal plane (FP) of L1 and BFP of L2; P3: FP of L2 and BFP of objective; BEC: Bose-Einstein condensate; Im1: imaging beam 1; MOT1, MOT2: beams for MOT; OC2: outcoupler (source of Im2); Im2: imaging beam 2; BS3: beam splitter; FM2/BS2: flip mirror or beam splitter cube, guiding the imaging beam in $-x$-direction towards camera 2. (b) Top view of combined imaging and phase imprinting system. The legend is the same as in (a). Note the additional camera. The coordinate systems are shown in the upper right corners of (a) and (b).

this gives $z_{L3} = 21\,\text{cm}$.
Note that lens L3 can be omitted if the objective is moved to a distance $z_1 > f_{Obj}$ between object and objective. The objective then produces a direct projection of the object onto camera 2. The distance z_2 between objective and the camera 2 has to obey the lens equation $\frac{1}{f} = \frac{1}{z_1} + \frac{1}{z_2}$. For a tenfold magnification this gives $z_1 = 23\,\text{mm}$. Although the objective can be easily and reproducibly moved by the motorised stage, this also cannot be done quickly enough for a simultaneous dual use. Therefore this method is only applicable in the flip mirror based version of the setup. In the case of fluorescence imaging, however, it saves another optical element which otherwise leads to additional loss of light.

6.6 The Objective

The objective is the heart of the new setup. Only with a customised objective for our specific experimental configuration, a spot size below $2\,\mu\text{m}$ is possible. Three major points have to be considered which affect the design of the objective and have influence on the numerical aperture and thus the minimum spot size:

- The access to the vacuum glass cell is restricted to a circular aperture of $\approx 35\,\text{mm}$ by the mount for the B field coils (see figure 6.4). The external diameter of

the objective must therefore not exceed 34 mm in order to keep enough fetch for alignment.

- Due to the size of the vacuum glass cell (38 mm side length) the objective must have a minimum focal length $f = 21$ mm including 2 mm fetch between objective and glass cell.

- The thickness of the *VYCOR* glass of the vacuum cell is 4 mm and has to be considered when designing the lenses.

The objective consists of three lenses. The actual numerical calculations for shape and relative position of the lenses has been performed by *Carl Zeiss Laser Systems*. The technical data of each of the lenses is given in figure 6.12. The minimum spot size achievable in the focus is specified as $d = 1.7\,\mu$m.
The exact beam path and spatial alignment is shown in figure 6.13. The objective mount cannot be provided by *Carl Zeiss Laser Systems* and has thus been designed in the framework of this thesis. It will be made of brass and consists of two components.
Component 1 is shown in in the engineering drawing of figure 6.14. It will hold lenses 3 and 2. The lenses are not shown in figure 6.14 but can be seen in figure 6.18. The lenses bear on the edges indicated by the 65° dimensioning, 1 mm from the rim of the lens. The reason for this kind of mounting is the fact that the lenses have a bevel on their outer rim which is too coarsely ground for a perfect coplanar alignment of the lenses, if they were bearing on the bevelled brink. The edge makes sure that the lens lies on its perfectly polished plane and will not be tilted.
The two lenses will be fixed by means of a special cement. The relative position of the two lenses is comparatively uncritical, the error ranges for lateral deviation are specified as 30 μm (H6 DIN standard) and for axial deviation as 0.1 mm without significantly influencing the minimum spot size. This accuracy is mechanically achievable if the whole component part is turned in a single clamping. The lenses thus can be mounted fixedly.
The position of lens 1 is more critical, laterally as well as axially. Therefore it is mounted on a separate component part of the objective, component 2, which can be seen in figure 6.15 and 6.16 in a way that it can be moved laterally and axially with respect to the other lenses.
Component 2 is connected to component 1 with a fine pitch thread which allows an axial fetch of 0.25 mm in order to fine tune the objective optics. An O-ring (green circles in figure 6.17 and 6.18) squeezed between the two components provides a certain pressure on the fine thread such that the fetch of the thread is minimised. Please refer to the technical engineering drawings 6.17, 6.18 for the detailed mechanics.
The necessary lateral fine tuning is performed by means of four set screws, which hold the lens in an adjustable position. In order to make sure that the lens bears coplanarly on its bearing plane, a rubber O-ring is pressed onto lens 3 by means of a clamping ring, which is screwed into component 2. The mounted lens is shown in figure 6.16. The O-ring is indicated as a red circle in figures 6.16 and 6.18.
A second sample of the vacuum glass cell is available in order to be able to take the 4 mm glass plate of the vacuum cell into account. It has, however been found that the thickness of the sides of the glass cell differs between 3.8(1) mm and 4.2(1) mm. In order to get a perfect spot it might therefore be necessary to use the same glass cell for alignment than

for the later experiments.
As methods for estimating the spot size, the slit method described in section 6.4.1 and the method described in section 6.4.2 can be used. An alternative would be to place a small object into the glass cell and optimise the point spread function, using the objective as an imaging objective. As soon as the optimal alignment is reached, the two component parts of the objective should be fixed permanently.

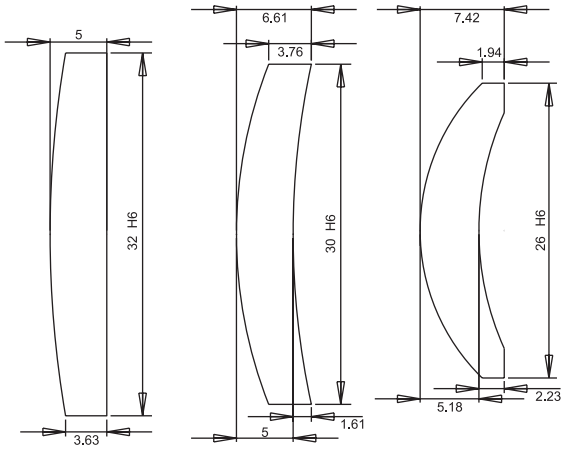

Figure 6.12: Lenses 1, 2, 3 and their technical data. Scale: 3:2

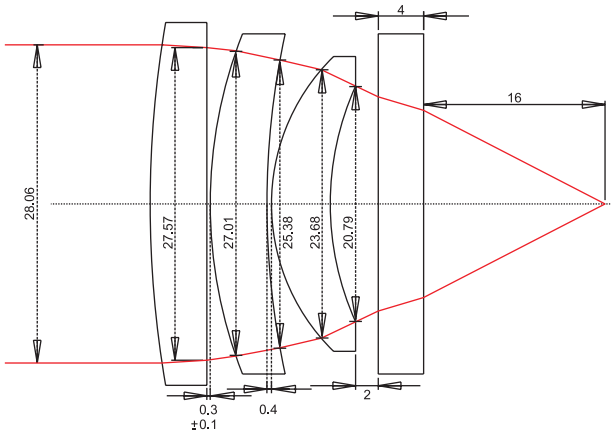

Figure 6.13: Lenses in their objective configuration. The beam path is indicated by the red lines. Scale: 3:2

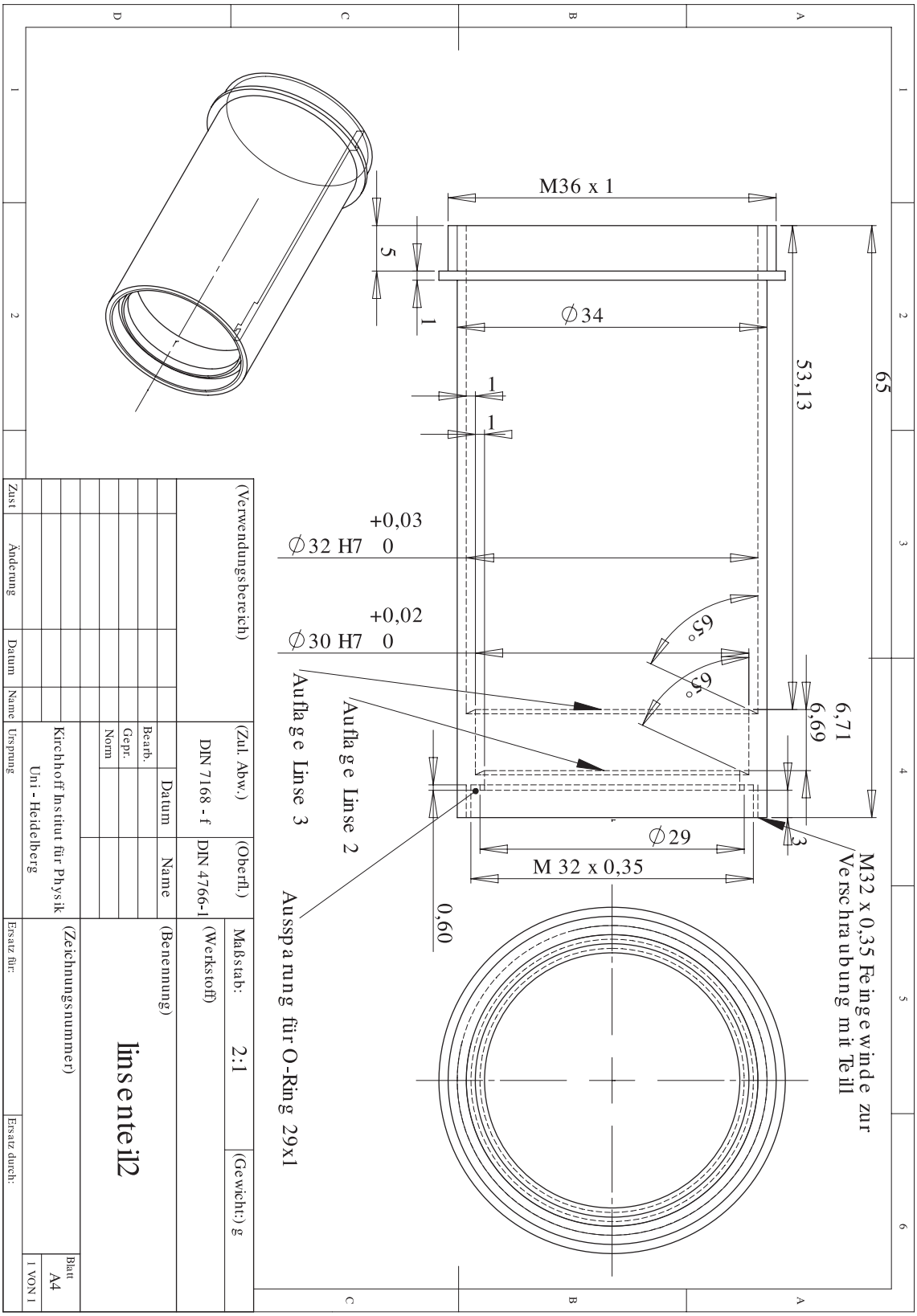

Figure 6.14: Objective component part 1. Scale: 3:2

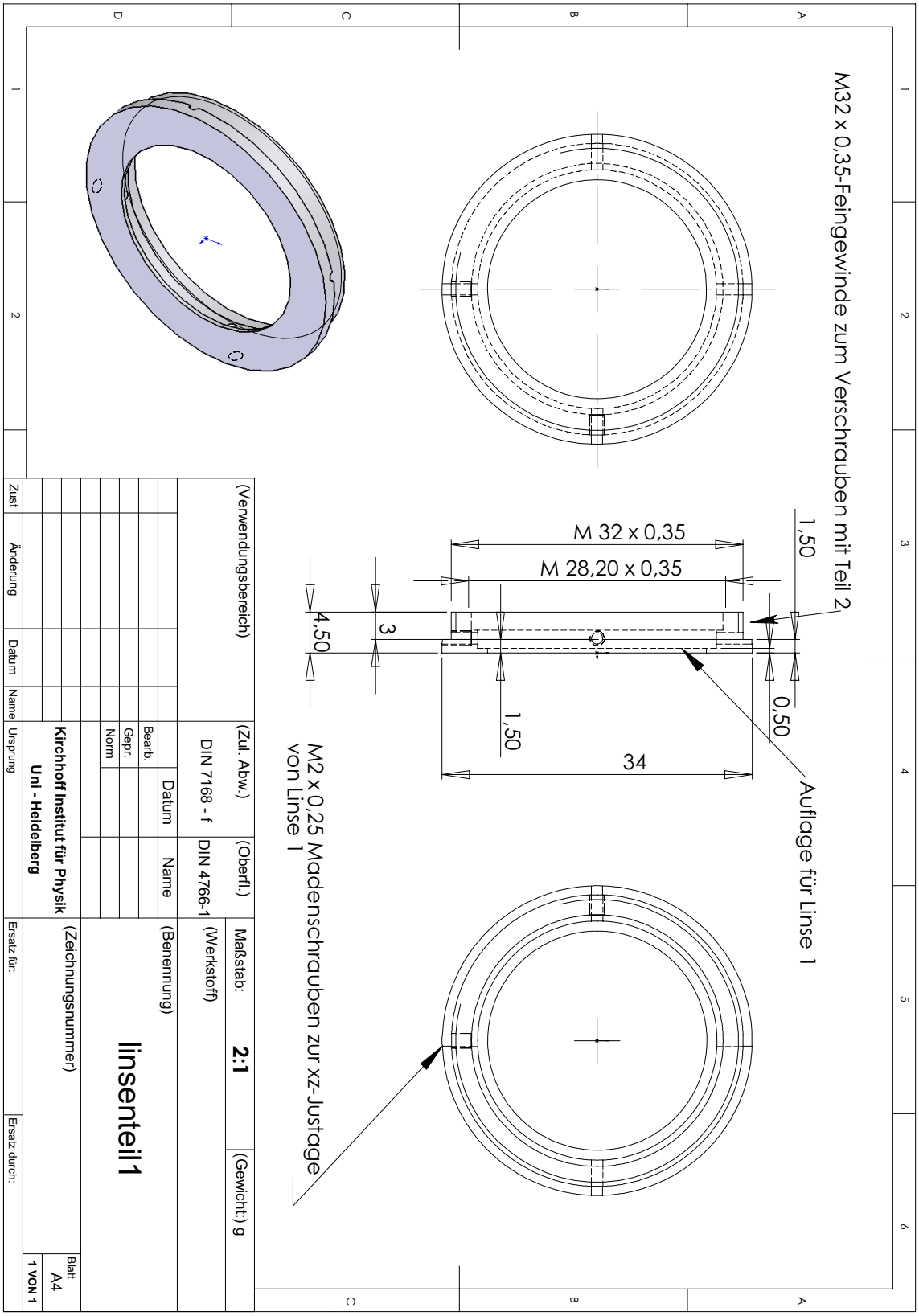

Figure 6.15: Objective component part 2. Scale: 3:2

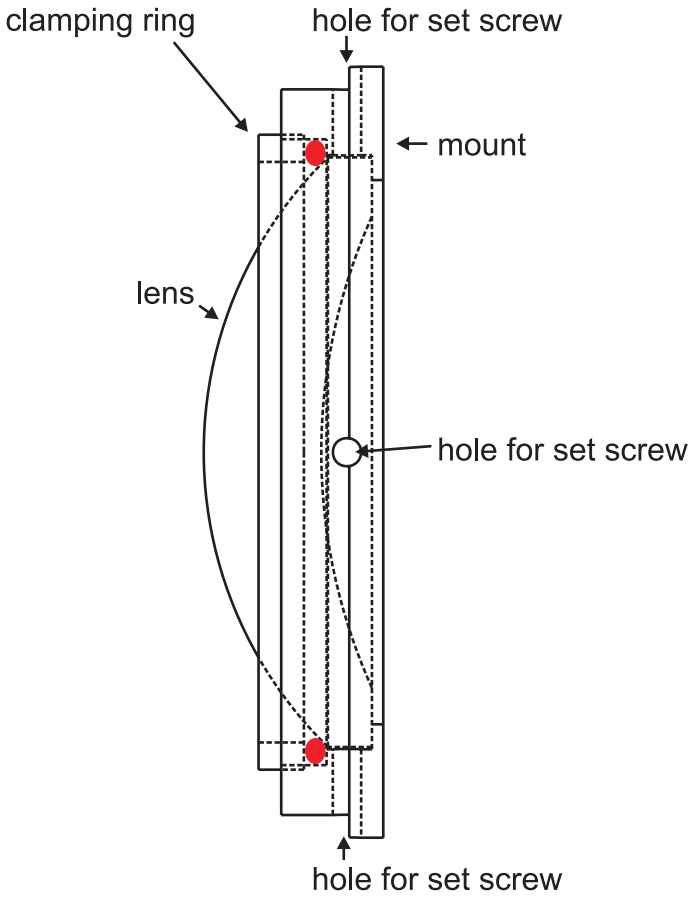

Figure 6.16: Lens 1 mounted in objective component 2. The lens is clamped onto the mount by means of a clamping ring screwed into the mount and a rubber O-ring (red circles). Scale: 3:1

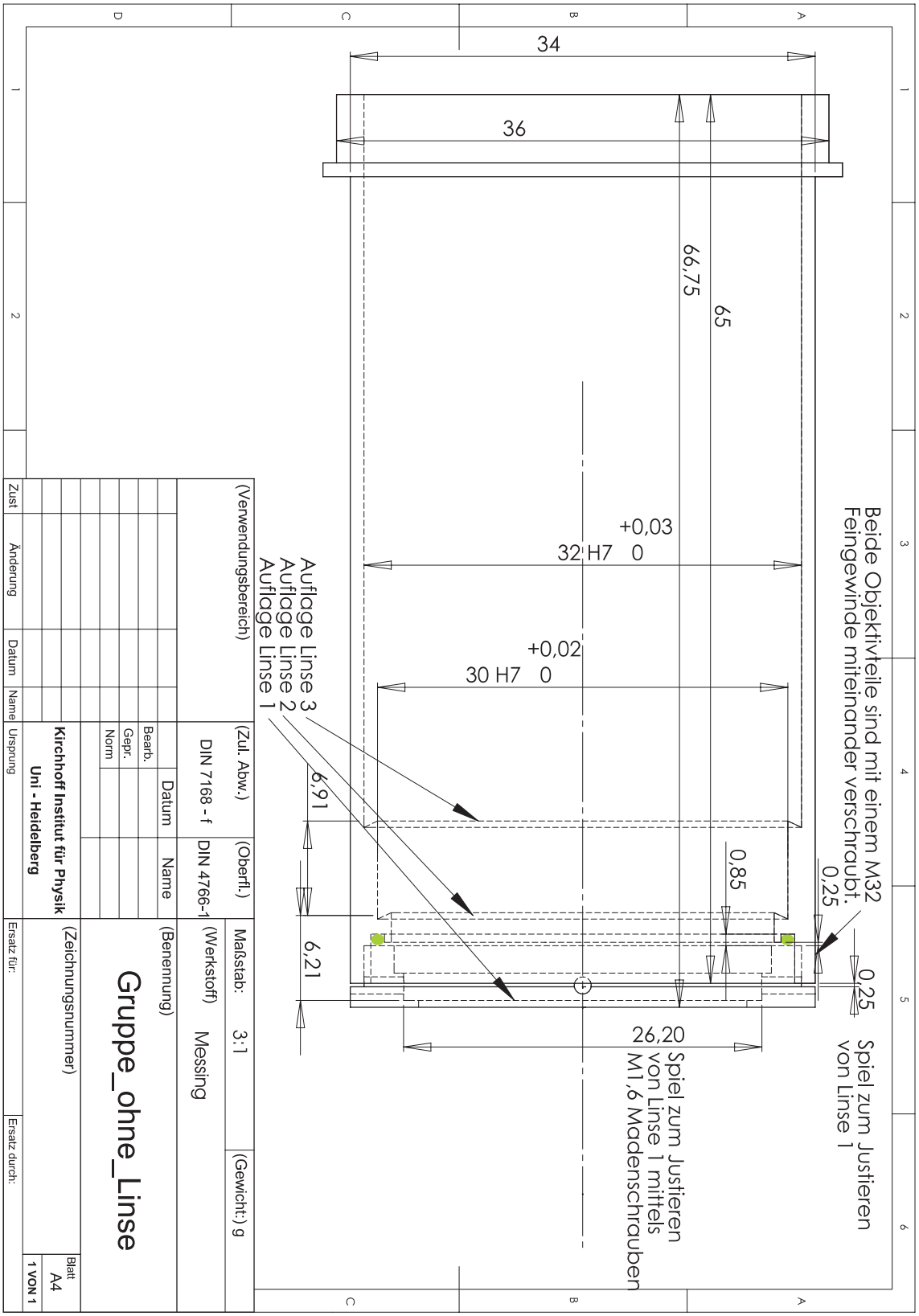

Figure 6.17: Engineering detail drawing of objective. Scale 9:4

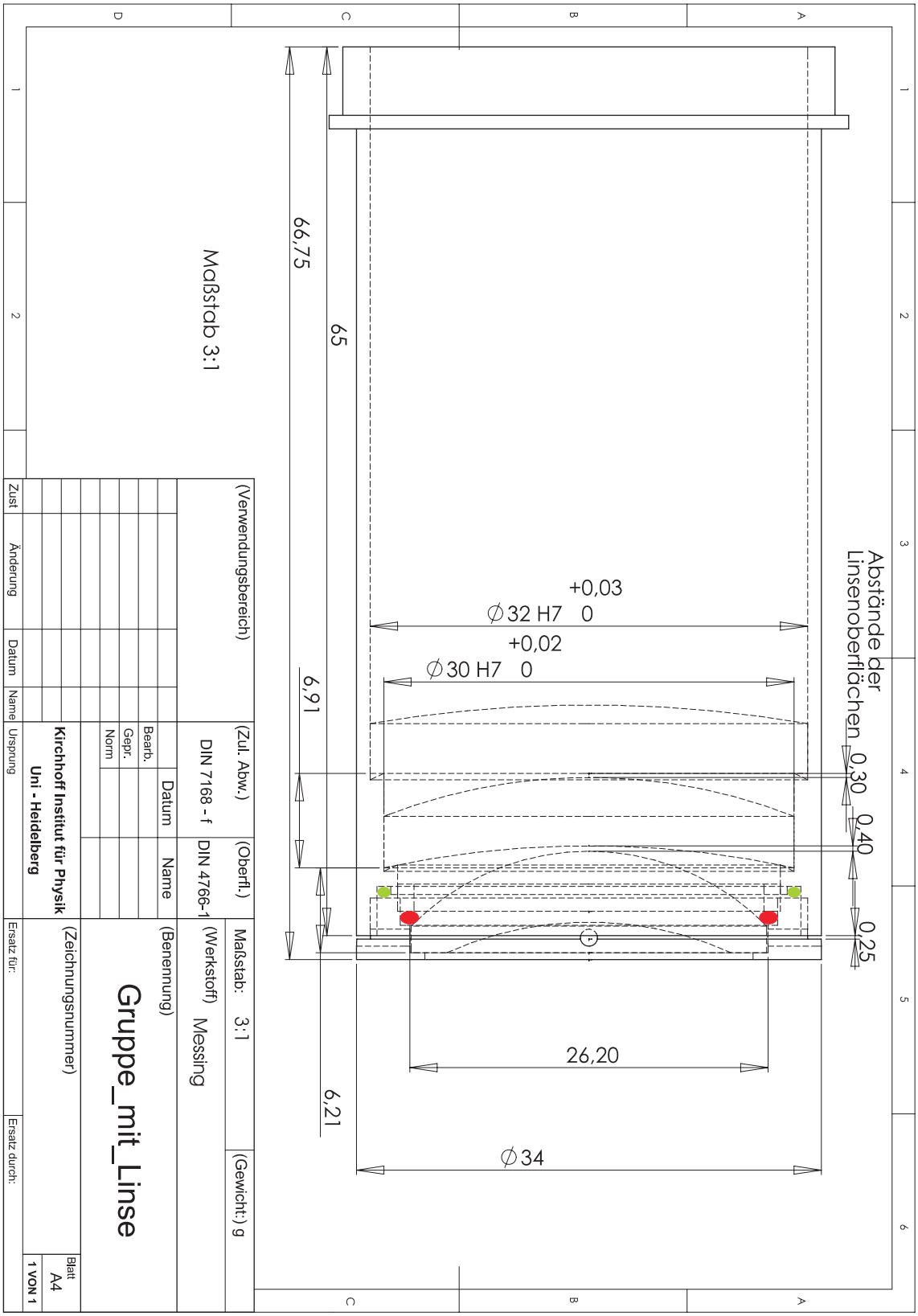

Figure 6.18: Engineering detail drawing of objective and lenses. Scale 9:4

Chapter 7

Conclusion and Outlook

The final year project presented in this thesis is composed of two parts. The first and major part presents the first experimental realisation of a single Bose-Einstein Josephson junction. It is defined as two coupled Bose-Einstein condensates in a double well potential which in our case is created by a superposition of a harmonic optical dipole confinement with an optical standing wave lattice potential.
At the beginning of this project, the state of the experiment was such that Josephson tunnelling measurements had already been attempted but the mechanical stability of the experimental setup was found to be too poor, leading to an intolerable fluctuation in the relative position of the laser beams creating the double well confinement.
Therefore, a more stable and compact arrangement for the relevant parts has been set up. Instead of being mounted on long posts which are susceptible for vibrations, the optical components are now fastened on an additional optical table, which is fixed on the main table using six massive aluminium table-legs. With this new setup the standard deviation of the position of our harmonic confinement for the atoms could be reduced from 800 nm to 100 nm, estimated by fitting the position of the BEC in the confinement.
Furthermore it was attempted to actively stabilise the beam of the crossed dipole trap using a quadrant photo diode as additional beam position reference. The signal of the this detector, however, shows a fluctuation also corresponding to approximately 100 nm which is not correlated to the position fits of the atomic cloud. The quadrant photo diode can therefore not be used for further active stabilisation but was still utilised for general beam diagnostics. This revealed for example that the effective beam position stability is significantly reduced if the beam is coupled into the fibre with the wrong polarisation direction which could thus be corrected.
Hereafter, an active control of the relative phase between the two laser beams creating the optical lattice was implemented. Now the position of the lattice can also be kept stable in the 100 nm range.
With these improvements it was finally possible to measure the Bose-Einstein Josephson tunnelling dynamics of a single junction for the first time. The theoretically predicted regimes of Josephson oscillations and macroscopic quantum self-trapping were confirmed. The former is characterised by an oscillating population imbalance of the BEC in the double well potential. It is commenced by an initial relative population difference between the two wells. The latter regime appears if the initial population imbalance exceeds a critical value. The BEC does not conduct full amplitude tunnelling oscillations any more. The initial population imbalance is locked instead. This counterintuitive effect is

due to the on-site atomic interaction and is not observed in superconducting Josephson junctions. A paper presenting these results has recently been published in Physical Review Letters [74].
After having successfully concluded the measurements of the Josephson tunnelling, a further stabilisation of the optical lattice setup was performed. Although the short term stability of the former realisation was sufficient, it suffered from long term instabilities, which made it necessary to readjust and recalibrate the optical lattice on a time scale of a few days. Therefore the setup has been redesigned and made much more compact, reducing the number of optical elements as well as the length of the beam paths to a minimum. The lattice depth is now stable within 10% for up to two weeks.

The second part of this thesis deals with the development of an extension to the experiment, namely a device to create arbitrary optical potentials which can be used for both high resolution phase imprinting and trapping of the atoms in complex confinements. It was stimulated by the idea to observe not only population imbalance induced Josephson oscillations but also phase induced Josephson oscillations. Furthermore, such a flexible device opens the way for numerous other experiments.
The optical potentials are created by a tightly focussed laser beam which is steered over the condensate on a time scale much faster than the dynamics of the BEC. This results in a time averaged optical dipole potential for the atoms. In the framework of this thesis, a setup for such a beam steering device has been planned in detail and prototypes have been tested using acousto optic modulators for beam deflection.
The resolution of the time averaged optical potential is only restricted by the size of the focussed laser spot. For single well manipulation it is necessary to create a very small spot, which is preferably only limited by diffraction. This requires a well corrected focussing objective. Tests of a commercial lens reveal an insufficient spot size, especially when taking into account that the walls of the vacuum glass cell will create additional aberration which a commercial lens is not corrected for. Therefore a customised objective was designed in cooperation with the company *Carl Zeiss Laser Systems*. This new objective has a specified focus spot size of $d = 1.7\,\mu$m. Apart from being used for phase imprinting, it can also be employed as additional high-resolution imaging objective for either absorption or fluorescence imaging.
The actual state of this venture at the end of this final year project is such that the feasibility has been successfully tested, the detailed blueprints for the setup are finished and all necessary parts except for the AODs of the beam deflector are present. Here, however, AOMs can be used in the meantime. The objective mount is readily designed but not yet constructed since the lenses are not available so far. In the meantime, however, a commercial lens can be implemented as interim solution without much effort of reconstruction afterwards. A mount for such a lens has been constructed and is ready to be installed. A second camera is also available so that the setup can already be used as secondary imaging device.

Outlook

The presented setup for creating arbitrary optical potentials opens a wide range of future experiments. Firstly, using it as a phase imprinting device, phase induced Josephson oscillations can be studied. Due to the flexibility of the system, also ring dark solitons [34]

can be created which require a circular phase imprinting pattern.
Using the device for creating a thin, quickly removable potential barrier in an otherwise harmonic confinement, the collision of two Bose-Einstein condensates can be studied. In this case the appearance of dark soliton fans is theoretically predicted [35, 36].
Single lattice site manipulation is possible for a BEC in a one dimensional lattice. Deepening a single lattice site in an otherwise periodic optical lattice potential is predicted to yield novel localisation effects [75].
Furthermore, a Fabry-Perot interferometer for a Bose-Einstein condensate can be easily constructed, which is expected to show interesting bistability phenomena in its resonances due to the atomic interaction [38]. This represents another classic experiment not yet implemented for Bose-Einstein condensates.

With this outlook into a future full of exciting experiments this thesis shall be concluded.

Bibliography

[1] M. Anderson, J. Ensher, M. Matthews, C. Wieman, and E. Cornell. Observation of Bose-Einstein condensation in a dilute atomic vapor. *Science*, 269:198, 1995.

[2] K. Davis, M.-O. Mewes, M. Andrews, N. van Druten, N. Durfee, D. Kurn, and W. Ketterle. Bose-Einstein condensation in a gas of sodium atoms. *Physical Review Letters*, 75:3969, 1995.

[3] C.C. Bradley, C.A. Sackett, J.J. Tollet, and R.G. Hulet. Evidence of Bose-Einstein condensation in an atomic gas with attractive interactions. *Physical Review Letters*, 75:1687, 1995.

[4] A. Einstein. Quantentheorie des einatomigen idealen Gases: Zweite Abhandlung. *Sitzungsber. Preuss. Akad. Wiss.*, page 18ff., 1925.

[5] S.N. Bose. Plancks Gesetz und Lichtquantenhypothese. *Z.Phys.*, 26(6):178–81, 1924.

[6] M.R. Andrews, C.G. Townsend, H.-J. Miesner, D.S. Durfee, D.M. Kurn, and W. Ketterle. Observation of interference between two Bose-Einstein condensates. *Science*, 275:637, 1997.

[7] K.E. Strecker, G.B. Partridge, A.G. Truscott, and R.G. Hulet. Formation and propagation of matter wave soliton trains. *Nature*, 417:150–153, 2002.

[8] L. Khaykovich, F. Schreck, F. Ferrari, T. Bourdel, J. Cubizolles, L.D. Carr, Y. Castin, and C. Salomon. Formation of a matter wave bright soliton. *Science*, 296:1290, 2002.

[9] B. Eiermann, T. Anker, M. Albiez, M. Taglieber, P. Treutlein, K.-P. Marzlin, and M. K. Oberthaler. Bright Bose-Einstein gap solitons of atoms with repulsive interaction. *Physical Review Letters*, 92:230401, 2004.

[10] S. Burger, K. Bongs, S. Dettmer, W. Ertmer, K. Sengstock, A. Sanpera, G.V. Shlyapnikov, and M. Lewenstein. Dark solitons in Bose-Einstein condensates. *Physical Review Letters*, 83:5198, 1999.

[11] K.W. Madison, F. Chevy, W. Wohlleben, and J. Dalibard. Vortices in a stirred Bose-Einstein condensate. *Journal of modern optics*, 47(14/15):2715–23, 2000.

[12] M. Ben Dahan, E. Peik, J. Reichel, Y. Castin, and C. Salomon. Bloch oscillations of atoms in an optical potential. *Physical Review Letters*, 76(24):4508, 1996.

[13] M. Kozuma, L. Deng, E.W. Hagley, J. Wen, R. Lutwak, K. Helmerson, S.L. Rolston, and W.D. Phillips. Coherent splitting of Bose-Einstein condensed atoms with optically induced Bragg diffraction. *Physical Review Letters*, 82:871, 1999.

[14] C.F. Bharucha, K.W. Madison, P.R. Morrow, S.R. Wilkinson, B. Sundaram, and M.G. Raizen. Observation of atomic tunneling from an accelerating optical potential. *Physical Review A*, 55(2):R857–60, 1997.

[15] B.P. Anderson and M. Kasevich. Macroscopic quantum interference from atomic tunnel arrays. *Science*, 282:1686, 1998.

[16] M. Greiner, O. Mandel, T. Esslinger, T. Hänsch, and I. Bloch. Quantum phase transition from a superfluid to a Mott insulator in a gas of ultracold atoms. *Nature*, 415:39–44, 2002.

[17] B.D. Josephson. Possible new effects in superconductive tunneling. *Physics Letters*, 1:251–253, 1962.

[18] P.L. Anderson and J.W. Rowell. Probable observation of the Josephson superconducting tunnel effect. *Physical Review Letters*, 10:230, 1963.

[19] A. Barone and P. Paterno. *Physics and Applications of the Josephson Effect*. Whiley and Sons, New York, 1982.

[20] S. Backhaus, S. Pereverzev, A. Loshak, J. C. Davis, and R. E. Packard. Direct measurement of the current-phase relation of a superfluid ^{3}He-b weak link. *Science*, 278:1435, 1997.

[21] J. Javanainen. Oscillatory exchange of atoms between traps containing Bose condensates. *Physical Review Letters*, 57:3164, 1986.

[22] A. Smerzi, S. Fantoni, S. Giovanazzi, and S.R. Shenoy. Quantum coherent atomic tunneling between two trapped Bose-Einstein condensates. *Physical Review Letters*, 79:4950–4953, 1997.

[23] S. Raghavan, A. Smerzi, S. Fantoni, and S.R. Shenoy. Coherent oscillations between two weakly coupled Bose-Einstein condensates: Josephson effects, π oscillations, and macroscopic quantum self-trapping. *Physical Review A*, 59:620–633, 1999.

[24] G.J. Milburn, J. Corney, E.M. Wright, and D.F. Walls. Quantum dynamics of an atomic Bose-Einstein condensate in a double well potential. *Physical Review A*, 55:4318–4324, 1997.

[25] I. Zapata, F. Sols, and A.J. Leggett. Josephson effect between trapped Bose-Einstein condensates. *Physical Review A*, 57:R28–31, 1998.

[26] M.W. Jack, M.J. Collett, and D.F. Walls. Coherent quantum tunneling between two Bose-Einstein condensates. *Physical Review A*, 54:R4625–4628, 1996.

[27] I. Marino, S. Raghavan, S. Fantoni, S.R. Shenoy, and A. Smerzi. Bose-condensate tunneling dynamics: Momentum-shortened pendulum with damping. *Physical Review A*, 60:487, 1999.

[28] T.G. Tiecke, M. Kemmann, Ch. Buggle, I. Shvarchuck, W. von Klitzing, and J.T.M Walraven. Bose-Einstein condensation in a magnetic double-well potential. *J. Opt. B*, 5:119–123, 2003.

[29] Y. Shin, M. Saba, T.A. Pasquini, W. Ketterle, D.E. Pritchard, and A.E. Leanhardt. Atom interferometry with Bose-Einstein condensates in a double-well potential. *Physical Review Letters*, 92:050405, 2004.

[30] J. Estève, T. Schumm, J.-B. Trebbia, I. Bouchoule, A. Aspect, and C.I. Westbrook. Realizing a stable magnetic double-well potential on an atom chip. *arXiv:physics/0503112*, 2005.

[31] F.S. Cataliotti, S. Burger, C. Fort, P. Maddaloni, F. Minardi, A. Trombettoni, A. Smerzi, and M. Ingusio. Josephson junction arrays with Bose-Einstein condensates. *Science*, 293:843, 2001.

[32] Th. Anker, M. Albiez, R. Gati, S. Hunsmann, B. Eiermann, A. Trombettoni, and M.K. Oberthaler. Nonlinear self-trapping of matter waves in periodic potentials. *Physical Review Letters*, 94:020403, 2005.

[33] Ł. Dobrek, M. Gajda, M. Lewenstein, K. Sengstock, G. Birkl, and W. Ertmer. Optical generation of vortices in trapped Bose-Einstein condensates. *Physical Review A*, 5:R3381, 1999.

[34] G. Theocharis, D.J. Frantzeskakis, P.G. Kevrekidis, B.A. Malomed, and Y.S. Kivshar. Ring dark solitons and vortex necklaces in Bose-Einstein condensates. *Physical Review Letters*, 90:120403, 2003.

[35] W.P. Reinhardt and C.W. Clark. Soliton dynamics in the collisions of BoseEinstein condensates: an analogue of the Josephson effect. *J. Phys. B. At. Mol. Opt. Phys.*, 30:L785, 1997.

[36] T.F. Scott, R.J. Ballagh, and K. Burnett. Formation of fundamental structures in BoseEinstein condensates. *J. Phys. B. At. Mol. Opt. Phys.*, 31:L329, 1998.

[37] G. Theocharis. Personal communication.

[38] T. Paul, K. Richter, and P. Schlagheck. Nonlinear resonant transport of Bose-Einstein condensates. *Physical Review Letters*, 94:020404, 2005.

[39] M.P. Feynman. *Lectures on physics*, volume 3. Addison-Wesley, New York, 1965.

[40] C.P. Poole, H.A. Farach, and R.J. Creswick. *Superconductivity*. Academic Press, San Diego, 1995.

[41] W. Buckel and R. Kleiner. *Supraleitung*. Wiley-VCH, Weinheim, 2004.

[42] W.C. Stewart. Current-voltage characteristics of Josephson junctions. *Applied Physics Letters*, 12:277, 1968.

[43] D.E. McCumber. Effect of ac impedance on dc voltage-current characteristics of superconductor weak-link. *Journal of Applied Physics*, 39:3113, 1968.

[44] W. Nolting. *Statistische Physik*. Verlag Zimmermann-Neufang, Ulmen, Germany, 1994.

[45] W. Ketterle, D.S. Durfee, and D.M. Stamper-Kurn. Making, probing and understanding Bose-Einstein condensates. In M. Inguscio, S. Stringari, and C. Wieman, editors, *Bose-Einstein Condensation in Atomic Gases*, Amsterdam: IOS Press, 1999. Società Italiana di Fisica.

[46] F. Dalfovo and S. Giorgini. Theory of Bose-Einstein condensation in trapped gases. *Review of Modern Physics*, 71(3):463–512, 1999.

[47] A.J. Leggett. Bose-Einstein condensation in the alkali gases: Some fundamental concepts. *Reviews of Modern Physics*, 73:307, 2001.

[48] E.P. Gross. Structure of a quantized vortex in boson systems. *Nuovo Cimento*, 20:454, 1961.

[49] E.P. Gross. Hydrodynamics of a superfluid condensate. *Jounal of Mathematical Physics*, 4:195, 1963.

[50] L.P. Pitaevskii. Vortex lines in an imperfect Bose gas. *Sov. Phys. JETP*, 13:451, 1961.

[51] D. Ananikian and T. Bergeman. The Gross-Pitaevskii equation for Bose particles in a double well potential: Two mode models and beyond. *arXiv:cond-mat/0503220*, 2005.

[52] M. Albiez. *Observation of nonlinear tunneling of a Bose-Einstein condensate in a single Josephson junction*. PhD thesis, Universität Heidelberg, 2005.

[53] T. Weber, J. Herbig, M. Mark, H.-C. Nägerl, and R. Grimm. Bose-Einstein condensation of cesium. *Science*, 299:232, 2003.

[54] L. Salasnich, A. Parola, and L. Reatto. Effective wave equations for the dynamics of cigar-shaped and disk-shaped Bose condensates. *Physical Review A*, 65(4):043614, 2002.

[55] B. Eiermann. *Kohärente nichtlineare Materienwellendynamik - Helle atomare Solitonen-*. PhD thesis, Universität Konstanz, 2004.

[56] P. Treutlein. Dispersionsmanagement für Materiewellen. Diplomarbeit, Universität Konstanz, Oktober 2002.

[57] M. Taglieber. Helle atomare Gap-Solitonen. Diplomarbeit, Universität Konstanz, Oktober 2003.

[58] S. Hunsmann. Josephson-Effekte in Bose-Einstein Kondensaten. Diplomarbeit, Universität Heidelberg, October 2004.

[59] E.L. Raab, M. Prentiss, A. Cable, S. Chu, and D.E. Pritchard. Trapping of neutral sodium atoms with radiation pressure. *Physical Review Letters*, 59:2631, 1987.

[60] W. Petrich, M. Anderson, J. Ensher, and E. Cornell. Stable, tightly confining magnetic trap for evaporative cooling of neutral atoms. *Physical Review Letters*, 74:3352, 1995.

[61] E. Majorana. Atomi orientati in campo magnetico variabile. *Nuovo Cimento*, 9:43–50, 1932.

[62] M.D. Barrett, J.A. Sauer, and M.S. Chapman. All-optical formation of an atomic Bose-Einstein condensate. *Physical Review Letters*, 87:101404, 2001.

[63] G. Cennini, G. Ritt, C. Geckeler, and M. Weitz. BoseEinstein condensation in a CO_2-laser optical dipole trap. *Applied Physics B*, 77:773779, 2003.

[64] H.J. Metcalf and P. van der Straten. *Laser Cooling and Trapping*. Springer Verlag, 1999.

[65] C. Cohen-Tannoudji, J. Dupont-Roc, and G. Grynberg. *Atom-Photon Interactions*. Wiley-Interscience, New York, 1992.

[66] P. Horowitz and W. Hill. *The Art of Electronics*. Cambridge University Press, Cambridge, second edition, 1989.

[67] J. W. Goodman. *Introduction to Fourier Optics*. McGraw-Hill, Boston, MA, 1998.

[68] E. Hecht. *Optics*. Addison-Wesley, Reading, MA, 1998.

[69] Y Hayasaki, M. Itoh, T. Yatagai, and N. Nishida. Nonmechanical optical manipulation of microparticle using spatial light modulator. *Optical Review*, 6(1):24–27, 1999.

[70] M. Reicherter, J. Liesener, T. Haist, and H.J. Tiziani. Advantages of holographic optical tweezers. *Proc. SPIE*, 5143:76–83, 2003.

[71] E.R. Dufresne, G. C. Spalding, M. T. Dearing, S. A. Sheets, and D.G. Grier. Computer-generated holographic optical tweezer arrays. *Rev. Sci. Inst.*, 72:1810–1816, 2001.

[72] K Svoboda and S.M. Block. Biological applications of optical forces. *Annu. Rev. Biophys. Biomol. Struct.*, 23:247–85, 1994.

[73] D. Meschede. *Optik, Licht und Laser*. B.G. Teubner Stuttgart, Leipzig, 1999.

[74] M. Albiez, R. Gati, J. Fölling, S. Hunsmann, M. Cristiani, and M. K. Oberthaler. Direct observation of tunneling and nonlinear self-trapping in a single bosonic josephson junction. *Physical Review Letters*, 95:010402, 2005.

[75] A. Trombettoni and P. Sodano. Personal communication.

Acknowledgements

I would like to thank all the people who accompanied me during this final year project. Everyone one of them supported me in his or her own way. Special thanks of course go out to my work group:

- First of all I am very grateful to my supervisor Markus Oberthaler for accepting me in his work group and giving me the opportunity to work at this exciting experiment. The working conditions were simply excellent, concerning his support as well as the state of the laboratory. I will always remember his enthusiasm for physics which was very stimulating for me. Neither will I forget those nights around the BBQ grill and in Heidelberg's bars. His feeling for maintaining the adequate ratio of 'full thrust physics' and 'social group activities' was the basis for a wonderful year in his group!

- Nagyon köszönöm to Rudolf Gati! He was never tired of explaining to me everything I wanted to know in all necessary detail and gave me the best support a diploma student could expect from 'his' PhD student. I learned a lot from him and I enjoyed the time with him in and outside of the lab.

- Whenever Michael Albiez enters the room a wave of energy follows in his wake. His straightforward way of attacking problems is really impressing to me and in the predominant number of cases successful. Although I still suspect him of spiriting away stabilising tables in shaky situations I owe him a lot, not only concerning this thesis.

- Stefan Hunsmann was my predecessor and I really enjoyed the time overlap we were having in the group. Thank you!

- Börge Hemmerling is following me as diploma student and as 'Schließer vom Dienst' and although we did not have the chance to spend a lot of time working in the lab together we have still had quite some fun outside the lab. He is definitely not being overestimated and I thank him, too!

- I also want to thank the 'tunnelling people', Ralf Stützle, Elisabeth Kierig, Thomas Hörner and Ramona Ettig, for their support which was more than the mere lending of laboratory equipment!

- Bernd Eiermann was not only a former lab course assistant of mine but also helped me out of problems during my thesis whenever he was in Heidelberg. Thank you!

Finally and most importantly I am deeply grateful to my parents who always and unconditionally supported me in all my decisions.

Erklärung:

Ich versichere, dass ich diese Arbeit selbstständig verfasst und keine anderen als die angegebenen Quellen und Hilfsmittel benutzt habe.

Heidelberg, den _____ _____

Unterschrift